



Universiteit Gent  
Faculteit Wetenschappen  
Vakgroep Fysica en Sterrenkunde

<sup>2</sup> No title yet

<sup>3</sup> No sub-title neither, obviously...

---

<sup>4</sup> Alexis Fagot

5



Thesis to obtain the degree of  
Doctor of Philosophy in Physics  
Academic years 2012-2017





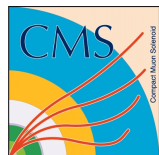


Universiteit Gent  
Faculteit Wetenschappen  
Vakgroep Fysica en Sterrenkunde

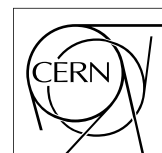
Promotoren: Dr. Michael Tytgat  
Prof. Dr. Dirk Ryckbosch

Universiteit Gent  
Faculteit Wetenschappen  
Vakgroep Fysica en Sterrenkunde  
Proeftuinstraat 86, B-9000 Gent, België  
Tel.: +32 9 264.65.28  
Fax.: +32 9 264.66.97

17



Thesis to obtain the degree of  
Doctor of Philosophy in Physics  
Academic years 2012-2017





## Acknowledgements

<sup>19</sup> Ici on remerciera tous les gens que j'ai pu croiser durant cette aventure et qui m'ont permis de passer  
<sup>20</sup> un bon moment

*Gent, ici la super date de la mort qui tue de la fin d'écriture*  
22 *Alexis Fagot*



# Table of Contents

23

24	<b>Acknowledgements</b>	i
25	<b>Nederlandse samenvatting</b>	vii
26	<b>English summary</b>	ix
27	<b>1 Introduction</b>	1-1
28	1.1 A story of High Energy Physics . . . . .	1-1
29	1.2 Organisation of this study . . . . .	1-1
30	<b>2 Investigating the TeV scale</b>	2-1
31	2.1 The Standard Model of Particle Physics . . . . .	2-1
32	2.2 The Large Hadron Collider & the Compact Muon Solenoid . . . . .	2-1
33	2.2.1 LHC, the most powerful particle accelerator . . . . .	2-1
34	2.2.2 CMS, a multipurpose experiment . . . . .	2-3
35	2.3 Muon Phase-II Upgrade . . . . .	2-3
36	<b>3 Physics of Resistive plate chambers</b>	3-1
37	3.1 Principle . . . . .	3-1
38	3.1.1 Electron drift velocity . . . . .	3-4
39	3.2 Rate capability and time resolution of Resistive Plate Chambers . . . . .	3-4
40	3.2.1 Operation modes . . . . .	3-4
41	3.2.2 Detector designs and performance . . . . .	3-6
42	3.2.2.1 Double-gap RPC . . . . .	3-6
43	3.2.2.2 Multigap RPC (MRPC) . . . . .	3-7
44	3.2.2.3 Charge distribution and performance limitations . . . . .	3-8
45	3.3 Signal formation . . . . .	3-11
46	3.4 Gas transport parameters . . . . .	3-11
47	<b>4 Longevity studies and Consolidation of the present CMS RPC subsystem</b>	4-1
48	4.1 Resistive Plate Chambers at CMS . . . . .	4-1
49	4.1.1 Overview . . . . .	4-1
50	4.1.2 The present RPC system . . . . .	4-2
51	4.1.3 Pulse processing of CMS RPCs . . . . .	4-3
52	4.2 Testing detectors under extreme conditions . . . . .	4-3
53	4.2.1 The Gamma Irradiation Facilities . . . . .	4-6
54	4.2.1.1 GIF . . . . .	4-6
55	4.2.1.2 GIF++ . . . . .	4-8
56	4.3 Preliminary tests at GIF . . . . .	4-10
57	4.3.1 Resistive Plate Chamber test setup . . . . .	4-10
58	4.3.2 Data Acquisition . . . . .	4-12

---

59	4.3.3	Geometrical acceptance of the setup layout to cosmic muons . . . . .	4-12
60	4.3.3.1	Description of the simulation layout . . . . .	4-13
61	4.3.3.2	Simulation procedure . . . . .	4-15
62	4.3.3.3	Results . . . . .	4-16
63	4.3.4	Photon flux at GIF . . . . .	4-16
64	4.3.4.1	Expectations from simulations . . . . .	4-16
65	4.3.4.2	Dose measurements . . . . .	4-21
66	4.3.5	Results and discussions . . . . .	4-22
67	4.4	Longevity tests at GIF++ . . . . .	4-23
68	4.4.1	Description of the Data Acquisition . . . . .	4-26
69	4.4.2	RPC current, environmental and operation parameter monitoring . . . . .	4-27
70	4.4.3	Measurement procedure . . . . .	4-28
71	4.4.4	Longevity studies results . . . . .	4-28
72	<b>5</b>	<b>Investigation on high rate RPCs</b>	<b>5-1</b>
73	5.1	Rate limitations and ageing of RPCs . . . . .	5-1
74	5.1.1	Low resistivity electrodes . . . . .	5-1
75	5.1.2	Low noise front-end electronics . . . . .	5-1
76	5.2	Construction of prototypes . . . . .	5-1
77	5.3	Results and discussions . . . . .	5-1
78	<b>6</b>	<b>Conclusions and outlooks</b>	<b>6-1</b>
79	6.1	Conclusions . . . . .	6-1
80	6.2	Outlooks . . . . .	6-1
81	<b>A</b>	<b>A data acquisition software for CAEN VME TDCs</b>	<b>A-1</b>
82	A.1	GIF++ DAQ file tree . . . . .	A-1
83	A.2	Usage of the DAQ . . . . .	A-2
84	A.3	Description of the readout setup . . . . .	A-3
85	A.4	Data read-out . . . . .	A-3
86	A.4.1	V1190A TDCs . . . . .	A-4
87	A.4.2	DataReader . . . . .	A-6
88	A.4.3	Data quality flag . . . . .	A-10
89	A.5	Communications . . . . .	A-12
90	A.5.1	V1718 USB Bridge . . . . .	A-13
91	A.5.2	Configuration file . . . . .	A-13
92	A.5.3	WebDCS/DAQ intercommunication . . . . .	A-17
93	A.5.4	Example of inter-process communication cycle . . . . .	A-18
94	A.6	Software export . . . . .	A-18
95	<b>B</b>	<b>Details on the offline analysis package</b>	<b>B-1</b>
96	B.1	GIF++ Offline Analysis file tree . . . . .	B-1
97	B.2	Usage of the Offline Analysis . . . . .	B-2
98	B.2.1	Output of the offline tool . . . . .	B-3
99	B.2.1.1	ROOT file . . . . .	B-3
100	B.2.1.2	CSV files . . . . .	B-5
101	B.3	Analysis inputs and information handling . . . . .	B-6
102	B.3.1	Dimensions file and IniFile parser . . . . .	B-6
103	B.3.2	TDC to RPC link file and Mapping . . . . .	B-7
104	B.4	Description of GIF++ setup within the Offline Analysis tool . . . . .	B-9

---

105	B.4.1	RPC objects . . . . .	B-9
106	B.4.2	Trolley objects . . . . .	B-10
107	B.4.3	Infrastructure object . . . . .	B-11
108	B.5	Handeling of data . . . . .	B-12
109	B.5.1	RPC hits . . . . .	B-13
110	B.5.2	Clusters of hits . . . . .	B-14
111	B.6	DAQ data Analysis . . . . .	B-15
112	B.6.1	Determination of the run type . . . . .	B-16
113	B.6.2	Beam time window calculation for efficiency runs . . . . .	B-17
114	B.6.3	Data loop and histogram filling . . . . .	B-18
115	B.6.4	Results calculation . . . . .	B-19
116	B.6.4.1	Rate normalisation . . . . .	B-19
117	B.6.4.2	Rate and activity . . . . .	B-21
118	B.6.4.3	Strip masking tool . . . . .	B-23
119	B.6.4.4	Output CSV files filling . . . . .	B-25
120	B.7	Current data Analysis . . . . .	B-29



<sup>121</sup>

<sup>122</sup>

## Nederlandse samenvatting –Summary in Dutch–

<sup>123</sup> Le resume en Neerlandais (j'aurais peut-être pu apprendre la langue juste pour ça...).



## English summary

<sup>125</sup> Le meme résume mais en Anglais (on commencera par la hein!).



# List of Figures

126

127	2.1	CERN accelerator complex. . . . .	2-2
128	2.2	Absorbed dose in the CMS cavern after an integrated luminosity of 3000 fb. R is the transverse distance from the beamline and Z is the distance along the beamline from the Interaction Point at Z=0. . . . .	2-3
129	2.3	A quadrant of the muon system, showing DTs (yellow), RPCs (light blue), and CSCs (green). The locations of new forward muon detectors for Phase-II are contained within the dashed box and indicated in red for GEM stations (ME0, GE1/1, and GE2/1) and dark blue for improved RPC (iRPC) stations (RE3/1 and RE4/1). . . . .	2-4
130	2.4	RMS of the multiple scattering displacement as a function of muon $p_T$ for the proposed forward muon stations. All of the electromagnetic processes such as bremsstrahlung and magnetic field effect are included in the simulation. . . . .	2-5
131	3.1	Different phases of the avalanche development in the RPC gas volume subjected to a constant electric field $E_0$ . a) An avalanche is initiated by the primary ionisation caused by the passage of a charged particle through the gas volume. b) Due to its growing size, the avalanche starts to locally influence the electric field. c) The electrons, lighter than the cations reach the anode first. d) The ions reach the cathode. While the charges have not recombined, the electric field in the small region around the avalanche stays affected and locally blind the detector. . . . .	3-2
132	3.2	Effeciency (circles and stars with 30 mV and 100 mV thresholds respectively) and streamer probability (opened circles) as function of the operating voltatge of a 2 mm single gap HPL RPC flushed with a gas mixture containing (a) 5%, (b) 2%, (c) 1% and (d) no $SF_6$ [32]. . . . .	3-3
133	3.3	Movement of the charge carriers in an RPC. Figure 3.3a: Voltage across an RPC whose electrode have a relative permittivity of 5 at the moment the tension s applied. Figure 3.3b: After the charge carriers moved, the electrodes are charged and there is no voltage drop over the electrodes anymore. The full potential is applied on the gas gap only. Figure 3.3c: The streamer discharge initiated by a charged particle transports electrons and cations towards the anode and cathode respectively. . . . .	3-5
134	3.4	Typical oscilloscope pulses in streamer mode (Figure 3.4a) and avalanche mode(Figure 3.4b). In the case of streamer mode, the very small avalanche signal is visible. . . . .	3-5
135	3.5	Rate capability comparison for the streamer and avalanche mode of operation. An order of magnitude in rate capability for a maximal efficiency drop of 10% is gained by using the avalanche mode over the streamer mode. . . . .	3-6
136	3.6	Possible double-gap RPC layouts: a) "standard" 1D double-gap RPC, as used in CMS experiment, where the anodes are facing each other and a 1D read-out plane is sandwiched in between them, b) double read-out double-gap RPC as used in ATLAS experiment, where the cathodes are facing each other and 2 read-out planes are used on the outer surfaces. This last layout can offer the possibility to use a 2D reconstruction by using orthogonal read-out planes. . . . .	3-7
137			

166	3.7	Comparison of performance of CMS double and single gap RPCs using cosmic muons [43]. Figure 3.7a: Comparison of efficiency sigmoids. Figure 3.7b: Voltage distribution at 95% of maximum efficiency. Figure 3.7c: $\Delta_{10\%}^{90\%}$ distribution. . . . .	3-7
167			
168			
169	3.8	Presentation of ALICE MRPC using 250 $\mu\text{m}$ gas gaps, 620 $\mu\text{m}$ outer glass electrodes and 550 $\mu\text{m}$ inner floating electrodes. More details on the labels are given in [44]. . . . .	3-8
170			
171	3.9	Particle identification applied to electrons in the STAR experiment. The identification is performed combining ToF and $dE/dx$ measurements [49]. . . . .	3-9
172			
173	3.10	Comparison of the detector performance of ALICE ToF MRPC [50] at fixed applied voltage (in blue) and at fixed effective voltage (in red). The effective voltage is kept fixed by increasing the applied voltage accordingly to the current drawn by the detector.	3-9
174			
175			
176	3.11	Ratio between total induced and drifting charge have been simulated for single gap, double-gap and multigap layouts [51]. The total induced charge for a double-gap RPC is a factor 2 higher than for a multigap. . . . .	3-10
177			
178			
179	3.12	Charge spectra have been simulated for single gap, double-gap and multigap layouts [51]. It appears that when single gap shows a decreasing spectrum, double and multigap layouts exhibit a spectrum whose peak is detached from the origin. The detachment gets stronger as the number of gaps increases. . . . .	3-10
180			
181			
182			
183	3.13	The maximal theoretical efficiency is simulated for single gap, double-gap and multigap layouts [51] at a constant gap thickness of 2 mm and using an effective Townsend coefficient of 9 $\text{mm}^{-1}$ . . . . .	3-11
184			
185			
186	4.1	Signals from the RPC strips are shaped by the FEE described on Figure 4.1a. Output LVDS signals are then read-out by a TDC module connected to a computer or converted into NIM and sent to scalers. Figure 4.1b describes how these converted signals are put in coincidence with the trigger. . . . .	4-3
187			
188			
189			
190	4.2	Description of the principle of a CFD. A comparison of threshold triggering (left) and constant fraction triggering (right) is shown in Figure 4.2a. Constant fraction triggering is obtained thanks to zero-crossing technique as explained in Figure 4.2b. The signal arriving at the input of the CFD is split into three components. A first one is delayed and connected to the inverting input of a first comparator. A second component is connected to the noninverting input of this first comparator. A third component is connected to the noninverting input of another comparator along with a threshold value connected to the inverting input. Finally, the output of both comparators is fed through an AND gate. . . . .	4-4
191			
192			
193			
194			
195			
196			
197			
198			
199	4.3	(4.3a) Extrapolation from 2016 data of single hit rate per unit area in the barrel region. (4.3b) Extrapolation from 2016 data of single hit rate per unit area in the endcap region. . . . .	4-5
200			
201			
202	4.4	Background Fluka simulation compared to 2016 Data at $L = 10^{34}\text{cm}^{-2}.\text{s}^{-1}$ in the fourth endcap disk region. A mismatch in between simulation and data can be observed. [To be understood.] . . . . .	4-6
203			
204			
205	4.5	Layout of the test beam zone called X5c GIF at CERN. Photons from the radioactive source produce a sustained high rate of random hits over the whole area. The zone is surrounded by 8 m high and 80 cm thick concrete walls. Access is possible through three entry points. Two access doors for personnel and one large gate for material. A crane allows installation of heavy equipment in the area. . . . .	4-7
206			
207			
208			
209			
210	4.6	$^{137}\text{Cs}$ decays by $\beta^-$ emission to the ground state of $^{137}\text{Ba}$ (BR = 5.64%) and via the 662 keV isomeric level of $^{137}\text{Ba}$ (BR = 94.36%) whose half-life is 2.55 min. . . . .	4-8
211			

212	4.7	Floor plan of the GIF++ facility. When the facility downstream of the GIF++ takes electron beam, a beam pipe is installed along the beam line (z-axis). The irradiator can be displaced laterally (its center moves from $x = 0.65$ m to 2.15 m), to increase the distance to the beam pipe. . . . .	4-8
213	4.8	Simulated unattenuated current of photons in the xz plane (Figure 4.8a) and yz plane (Figure 4.8b) through the source at $x = 0.65$ m and $y = 0$ m. With angular correction filters, the current of 662 keV photons is made uniform in xy planes. . . . .	4-9
214	4.9	Description of the RPC setup. Dimensions are given in mm. A tent containing RPCs is placed at 1720 mm from the source container. The source is situated in the center of the container. RE-4-2-BARC-161 chamber is 160 mm inside the tent. This way, the distance between the source and the chambers plan is 2060 mm. Figure 4.9a provides a side view of the setup in the xz plane while Figure 4.9b shows a top view in the yz plane. . . . .	4-10
215	4.10	RE-4-2-BARC-161 chamber is inside the tent as described in Figure 4.9. In the top right, the two scintillators used as trigger can be seen. This trigger system has an inclination of 10° relative to horizontal and is placed above half-partition B2 of the RPCs. PMT electronics are shielded thanks to lead blocks placed in order to protect them without stopping photons from going through the scintillators and the chamber. . . . .	4-11
216	4.11	Hit distributions over all 3 partitions of RE-4-2-BARC-161 chamber is showed on these plots. Top, middle and bottom figures respectively correspond to partitions A, B, and C. These plots show that some events still occur in other half-partitions than B2, which corresponds to strips 49 to 64, in front of which the trigger is placed, contributing to the inefficiency of detection of cosmic muons. In the case of partitions A and C, the very low amount of data can be interpreted as noise. On the other hand, it is clear that a little portion of muons reach the half-partition B1, corresponding to strips 33 to 48. . . . .	4-12
217	4.12	Results are derived from data taken on half-partition B2 only. On the 18 <sup>th</sup> of June 2014, data has been taken on chamber RE-2-BARC-161 at building 904 (Prevessin Site) with cosmic muons providing us a reference efficiency plateau of $(97.54 \pm 0.15)\%$ represented by a black curve. A similar measurement has been done at GIF on the 21 <sup>st</sup> of July with the same chamber giving a plateau of $(78.52 \pm 0.94)\%$ represented by a red curve. . . . .	4-13
218	4.13	Representation of the layout used for the simulations of the test setup. The RPC is represented as a yellow trapezoid while the two scintillators as blue cuboids looking at the sky. A green plane corresponds to the muon generation plane within the simulation. Figure 4.9a shows a global view of the simulated setup. Figure 4.9b shows a zommed view that allows to see the 2 scintillators as well as the full RPC plane. . . . .	4-14
219	4.14	$\gamma$ flux $F(D)$ is plot using values from table 4.1. As expected, the plot shows similar attenuation behaviours with increasing distance for each absorption factors. . . . .	4-17
220	4.15	Figure 4.15a shows the linear approximation fit done via formulae 4.7 on data from table 4.2. Figure 4.15b shows a comparison of this model with the simulated flux using a and b given in figure 4.15a in formulae 4.4 and the reference value $D_0 = 50\text{cm}$ and the associated flux for each absorption factor $F_0^{ABS}$ from table 4.1 . . . . .	4-19
221	4.16	Dose measurements has been done in a plane corresponding to the tents front side. This plan is 1900 mm away from the source. As explained in the first chapter, a lens-shaped lead filter provides a uniform photon flux in the vertical plan orthogonal to the beam direction. If the second line of measured fluxes is not taken into account because of lower values due to experimental equipments in the way between the source and the tent, the uniformity of the flux is well showed by the results. . . . .	4-21
222			
223			
224			
225			
226			
227			
228			
229			
230			
231			
232			
233			
234			
235			
236			
237			
238			
239			
240			
241			
242			
243			
244			
245			
246			
247			
248			
249			
250			
251			
252			
253			
254			
255			
256			
257			
258			
259			
260			

261	4.17	4-22
262	4.18 Evolution of the maximum efficiency for RE2 (4.18a) and RE4 (4.18b) chambers 263 with increasing extrapolated $\gamma$ rate per unit area at working point. Both irradiated 264 (blue) and non irradiated (red) chambers are shown. . . . .	4-24
265	4.19 Evolution of the working point for RE2 (4.19a) and RE4 (4.19b) with increasing 266 extrapolated $\gamma$ rate per unit area at working point. Both irradiated (blue) and non 267 irradiated (red) chambers are shown. . . . .	4-24
268	4.20 Evolution of the maximum efficiency at HL-LHC conditions, i.e. a background hit 269 rate per unit area of 300 Hz/cm <sup>2</sup> , with increasing integrated charge for RE2 (4.20a) 270 and RE4 (4.20b) detectors. Both irradiated (blue) and non irradiated (red) chambers 271 are shown. The integrated charge for non irradiated detectors is recorded during test 272 beam periods and stays small with respect to the charge accumulated in irradiated 273 chambers. . . . .	4-25
274	4.21 Comparison of the efficiency sigmoid before (triangles) and after (circles) irradiation 275 for RE2 (4.21a) and RE4 (4.21b) detectors. Both irradiated (blue) and non irradiated 276 (red) chambers are shown. . . . .	4-25
277	4.22 Evolution of the Bakelite resistivity for RE2 (4.22a) and RE4 (4.22b) detectors. Both 278 irradiated (blue) and non irradiated (red) chambers are shown. . . . .	4-26
279	4.23 Evolution of the noise rate per unit area for the irradiated chamber RE2-2-BARC-9 280 only. . . . .	4-26
281	A.1 (A.1a) View of the front panel of a V1190A TDC module [57]. (A.1b) View of the 282 front panel of a V1718 Bridge module [58]. (A.1c) View of the front panel of a 6U 283 6021 VME crate [59]. . . . .	A-3
284	A.2 Module V1190A <i>Trigger Matching Mode</i> timing diagram [57]. . . . .	A-4
285	A.3 Structure of the ROOT output file generated by the DAQ. The 5 branches ( <code>EventNumber</code> , 286 <code>number_of_hits</code> , <code>Quality_flag</code> , <code>TDC_channel</code> and <code>TDC_TimeStamp</code> ) are visible on 287 the left panel of the ROOT browser. On the right panel is visible the histogram cor- 288 responding to the variable <code>nHits</code> . In this specific example, there were approximately 289 50k events recorded to measure the gamma irradiation rate on the detectors. Each 290 event is stored as a single entry in the <code>TTree</code> . . . . .	A-10
291	A.4 The effect of the quality flag is explained by presenting the content of <code>TBranch</code> 292 <code>number_of_hits</code> of a data file without <code>Quality_flag</code> in Figure A.4a and the con- 293 tent of the same <code>TBranch</code> for data corresponding to a <code>Quality_flag</code> where all TDCs 294 were labelled as <code>GOOD</code> in Figure A.4b taken with similar conditions. It can be noted 295 that the number of entries in Figure A.4b is slightly lower then in Figure A.4a due 296 to the excluded events. . . . .	A-12
297	A.5 Using the same data as previously showed in Figure A.4, the effect of the quality 298 flag is explained by presenting the reconstructed hit multiplicity of a data file with- 299 out <code>Quality_flag</code> in Figure A.5a and the reconstructed content of the same RPC 300 partition for data corresponding to a <code>Quality_flag</code> where all TDCs were labelled as 301 <code>GOOD</code> in Figure A.5b taken with similar conditions. The artificial high content of bin 302 0 is completely suppressed. . . . .	A-12
303	A.6 WebDCS DAQ scan page. On this page, shifters need to choose the type of scan 304 (Rate, Efficiency or Noise Reference scan), the gamma source configuration at the 305 moment of data taking, the beam configuration, and the trigger mode. These in- 306 formation will be stored in the DAQ ROOT output. Are also given the minimal 307 measurement time and waiting time after ramping up of the detectors is over before 308 starting the data acquisition. Then, the list of HV points to scan and the number of 309 triggers for each run of the scan are given in the table underneath. . . . .	A-14

---

310	B.1	Example of expected hit time distributions in the cases of efficiency (Figure B.1a) and noise/gamma rate per unit area (Figure B.1b) measurements as extracted from the raw ROOT files. The unit along the x-axis corresponds to ns. The fact that "the" muon peak is not well defined in Figure B.1a is due to the contribution of all the RPCs being tested at the same time that don't necessarily have the same signal arrival time. Each individual peak can have an offset with the ones of other detectors. The inconsistancy in the first 100 ns of both time distributions is an artefact of the TDCs and are systematically rejected during the analysis. . . . .	B-16
311			
312			
313			
314			
315			
316			
317			
318	B.2	The effect of the quality flag is explained by presenting the reconstructed hit multi- plicity of a data file without <code>Quality_flag</code> . The artificial high content of bin 0 is the effect of corrupted data. . . . .	B-19
319			
320			
321	B.3	Display of the masking tool page on the webDCS. The window on the left allows the shifter to edit <code>ChannelsMapping.csv</code> . To mask a channel, it only is needed to set the 3rd field corresponding to the strip to mask to 0. It is not necessary for older mapping file formats to add a 1 for each strip that is not masked as the code is versatile and the default behaviour is to consider missing mask fields as active strips. The effect of the mask is directly visible for noisy channels as the corresponding bin turns red. The global effect of masking strips will be an update of the rate value showed on the histogram that will take into consideration the rejected channels. . . . .	B-24
322			
323			
324			
325			
326			
327			
328			



## List of Tables

329

330	3.1 Properties of the most used electrode materials for RPCs. . . . .	3-4
331	4.1 Total photon flux ( $E\gamma \leq 662$ keV) with statistical error predicted considering a	
332	$^{137}\text{Cs}$ activity of 740 GBq at different values of the distance $D$ to the source along	
333	the x-axis of irradiation field [54]. . . . .	4-16
334	4.2 Correction factor $c$ is computed thanks to formulae 4.5 taking as reference $D_0 =$	
335	50 cm and the associated flux $F_0^{ABS}$ for each absorption factor available in table 4.1.	4-18
336	4.3 The data at $D_0$ in 1997 is taken from [54]. In a second step, using Equations 4.8	
337	and 4.9, the flux at $D$ can be estimated in 1997. Then, taking into account the	
338	attenuation of the source activity, the flux at $D$ can be estimated at the time of the	
339	tests in GIF in 2014. Finally, assuming a sensitivity of the RPC to $\gamma$ $s = 2 \cdot 10^{-3}$ ,	
340	an estimation of the hit rate per unit area is obtained. . . . .	4-20
341	A.1 Inter-process communication cycles in between the webDCS and the DAQ through	
342	file string signals. . . . .	A-19



# List of Acronyms

## List of Acronyms

### A

349 **AFL**

Almost Full Level

### B

354 **BARC**

Bhabha Atomic Research Centre

355 **BLT**

Block Transfer

356 **BR**

Branching Ratio

### C

361 **CAEN**

Costruzioni Apparecchiature Elettroniche Nucleari S.p.A.

362 **CERN**

European Organization for Nuclear Research

363 **CFD**

Constant Fraction Discriminator

364 **CMS**

Compact Muon Solenoid

365 **CSC**

Cathode Strip Chamber

### D

370 **DAQ**

Data Acquisition

371 **DCS**

Detector Control Software

372 **DQM**

Data Quality Monitoring

373 **DT**

Drift Tube

### F

378	FEE	Front-End Electronics
379	FEB	Front-End Board
380		
381	<b>G</b>	
383		
384	GE-/-	Find a good description
385	GE1/1	Find a good description
386	GE2/1	Find a good description
387	GEANT	GEometry ANd Tracking - a series of software toolkit platforms developed by CERN
388		
389	GEM	Gas Electron Multiplier
390	GIF	Gamma Irradiation Facility
391	GIF++	new Gamma Irradiation Facility
392		
393	<b>H</b>	
394		
395		
396	HL-LHC	High Luminosity LHC
397	HPL	High-pressure laminate
398	HV	High Voltage
399		
400		
401	<b>I</b>	
402		
403	iRPC	improved RPC
404	IRQ	Interrupt Request
405	ISR	Intersecting Storage Rings
406		
407		
408	<b>L</b>	
409		
410	LEP	Large Electron-Positron
411	LHC	Large Hadron Collider
412	LS1	First Long Shutdown
413	LS3	Third Long Shutdown
414	LV	Low Voltage
415	LVDS	Low-Voltage Differential Signaling
416		
417		
418	<b>M</b>	
419		
420	MC	Monte Carlo

421	MCNP	Monte Carlo N-Particle
422	ME-/-	Find good description
423	ME0	Find good description
424	MRPC	Multigap RPC
425		
426	<b>N</b>	
428		
429	NIM	Nuclear Instrumentation Module logic signals
430		
431	<b>P</b>	
432		
433		
434	PS	Proton Synchrotron
435	PMT	PhotoMultiplier Tube
436		
437	<b>R</b>	
438		
439		
440	RE-/-	Find a good description
441	RE2/2	Find a good description
442	RE3/1	Find a good description
443	RE3/2	Find a good description
444	RE4/1	Find a good description
445	RE4/2	Find a good description
446	RE4/3	Find a good description
447	RMS	Root Mean Square
448	ROOT	a framework for data processing born at CERN
449	RPC	Resistive Plate Chamber
450		
451	<b>S</b>	
452		
453		
454	SC	Synchrocyclotron
455	SPS	Super Proton Synchrotron
456		
457	<b>T</b>	
458		
459		
460	TDC	Time-to-Digital Converter
461	ToF	Time-of-flight
462		
463	<b>W</b>	
464		
465		

<sup>466</sup> webDCS      Web Detector Control System

# 1

## Introduction

467

468

<sup>469</sup> **1.1 A story of High Energy Physics**

<sup>470</sup> **1.2 Organisation of this study**



# 2

471

472

## Investigating the TeV scale

### 473 2.1 The Standard Model of Particle Physics

### 474 2.2 The Large Hadron Collider & the Compact Muon Solenoid

475 Throughout its history, CERN has played a leading role in high energy particle physics. Large re-  
476 gional facilities such as CERN were thought after the second world war in an attempt to increase  
477 international scientific collaboration and allows scientists to share the forever increasing costs of  
478 experiment facilities required due to the need for increasing the energy in the center of mass to  
479 deeper probe matter. The construction of the first accelerators at the end of the 50s, the Synchro-  
480 cyclotron (SC) and the Proton Synchrotron (PS), was directly followed by the first observation of  
481 antinuclei in 1965 [1]. Strong from the experience of the Intersecting Storage Rings (ISR), the very  
482 first proton-proton collider that showed hints that protons are not elementary particles, the Super  
483 Proton Synchrotron (SPS) was built in the 70s to investigate the structure of protons, the preference  
484 for matter over antimatter, the state of matter in the early universe or exotic particles, and lead to  
485 the discovery in 1983 of the W and Z bosons [2–5]. These newly discovered particles and the elec-  
486 troweak interaction would then be studied in details by the Large Electron-Positron (LEP) collider  
487 that will help to prove in 1989 that there only are three generations of elementary particles [6]. The  
488 LEP would then be dismantled in 2000 to allow for the LHC to be constructed in the existing tunnel.

#### 489 2.2.1 LHC, the most powerful particle accelerator

490 The LHC has always been considered as an option to the future of CERN. At the moment of the  
491 construction of the LEP, the tunnel was built in order to accomodate what would be a Large Hadron  
492 Collider with a dipole field of 10 T and a beam energy in between 8 and 9 TeV [7] directly followed  
493 in 1985 with the creation of a 'Working Group on the Scientific and Technological Future of CERN'  
494 to investigate such a collider [8]. The decision was finally taken almost 10 years later, in 1994, to  
495 construct the LHC in the LEP tunnel [9] and the approval of the 4 main experiments that would take

place at the 4 interaction points would come in 1997 [10] and 1998 [11]:

- ALICE [12] has been designed in the purpose of studying quark-gluon plasma that is believed to have been a state of matter that existed in the very first moment of the universe.
- ATLAS [13] and CMS [14] are general purpose experiments that have been designed with the goal of continuing the exploration of the Standard Model and investigate new physics.
- LHCb [15] has been designed to investigate the preference of matter over antimatter in the universe through the CP violation.

These large scale experiments, as well as the full CERN accelerator complex, are displayed on Figure 2.1.

### CERN's Accelerator Complex

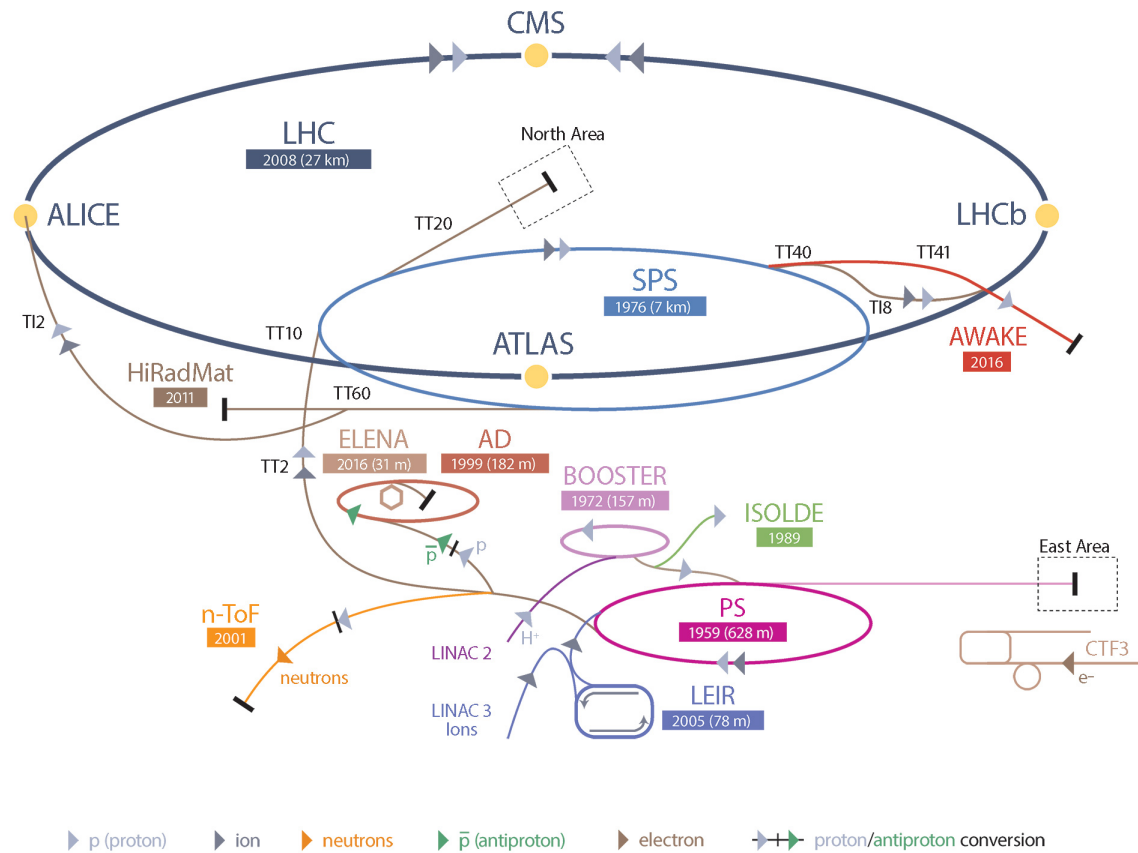


Figure 2.1: CERN accelerator complex.

The LHC is a 27 km long hadron collider and is the most powerful accelerator used for particle physics since 2008 [16]. Run 1 of LHC was enough to discover the Higgs boson [17] and

507 pentaquarks [18]. The LHC was originally designed to collide protons at a center-of-mass energy  
 508 of 14 TeV and luminosity of  $10^{34} \text{ cm}^{-2}\text{s}^{-1}$ , as well as  $Pb$  ions at a center-of-mass energy  
 509 of 2.8 TeV/A with a peak luminosity of  $10^{27} \text{ cm}^{-2}\text{s}^{-1}$ . Nevertheless, after the Third Long Shut-  
 510 down (LS3) (2024-2026), the accelerator will be in the so called High Luminosity LHC (HL-LHC)  
 511 configuration [19], increasing its instantaneous luminosity to  $10^{35} \text{ cm}^{-2}\text{s}^{-1}$  for  $pp$  collisions and to  
 512  $4.5 \times 10^{27} \text{ cm}^{-2}\text{s}^{-1}$ .

### 513 2.2.2 CMS, a multipurpose experiment

## 514 2.3 Muon Phase-II Upgrade

515 After the more than two years lasting First Long Shutdown (LS1), the Large Hadron Collider (LHC)  
 516 delivered its very first Run-II proton-proton collisions early 2015. LS1 gave the opportunity to the  
 517 LHC and to its experiments to undergo upgrades. The accelerator is now providing collisions  
 518 at center-of-mass energy of 13 TeV and bunch crossing rate of 40 MHz, with a peak luminosity  
 519 exceeding its design value. During the first and upcoming second LHC Long Shutdown, the Compact  
 520 Muon Solenoid (CMS) detector is also undergoing a number of upgrades to maintain a high system  
 521 performance [20].

522 From the LHC Phase-2 or High Luminosity LHC (HL-LHC) period onwards, i.e. past the Third  
 523 Long Shutdown (LS3), the performance degradation due to integrated radiation as well as the average  
 524 number of inelastic collisions per bunch crossing, or pileup, will rise substantially and become a  
 525 major challenge for the LHC experiments, like CMS that are forced to address an upgrade program  
 526 for Phase-II [21]. Simulations of the expected distribution of absorbed dose in the CMS detector  
 527 under HL-LHC conditions, show in figure 4.16 that detectors placed close to the beamline will have  
 528 to withstand high irradiation, the radiation dose being of the order of a few tens of Gy.

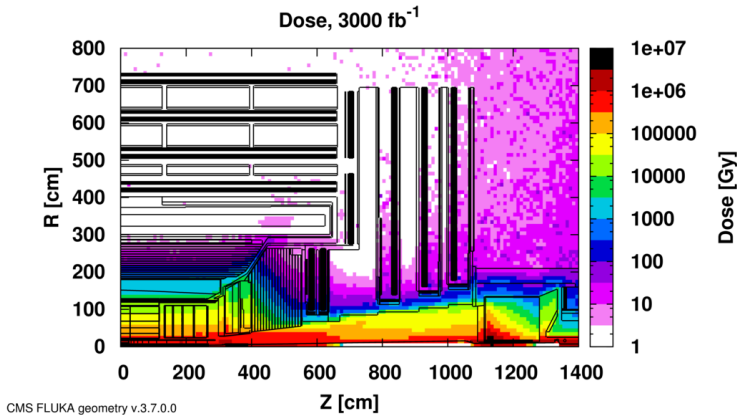
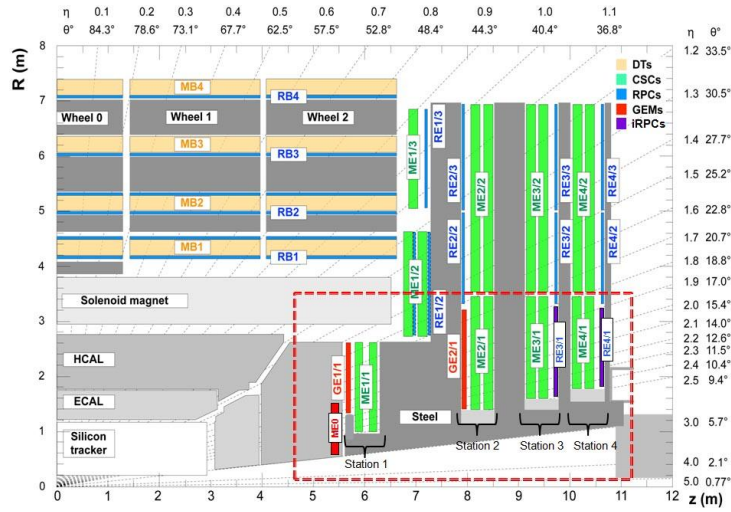


Figure 2.2: Absorbed dose in the CMS cavern after an integrated luminosity of  $3000 \text{ fb}^{-1}$ .  $R$  is the transverse distance from the beamline and  $Z$  is the distance along the beamline from the Interaction Point at  $Z=0$ .

529 The measurement of small production cross-section and/or decay branching ratio processes, such  
 530 as the Higgs boson coupling to charge leptons or the  $B_s \rightarrow \mu^+\mu^-$  decay, is of major interest and  
 531 specific upgrades in the forward regions of the detector will be required to maximize the physics  
 532 acceptance on the largest possible solid angle. To ensure proper trigger performance within the

present coverage, the muon system will be completed with new chambers. In figure 2.3 one can see that the existing Cathode Strip Chambers (CSCs) will be completed by Gas Electron Multipliers (GEMs) and Resistive Plate Chambers (RPCs) in the pseudo-rapidity region  $1.6 < |\eta| < 2.4$  to complete its redundancy as originally scheduled in the CMS Technical Proposal [22].



*Figure 2.3: A quadrant of the muon system, showing DTs (yellow), RPCs (light blue), and CSCs (green). The locations of new forward muon detectors for Phase-II are contained within the dashed box and indicated in red for GEM stations (ME0, GE1/1, and GE2/1) and dark blue for improved RPC (iRPC) stations (RE3/1 and RE4/1).*

RPCs are used by the CMS first level trigger for their good timing performances. Indeed, a very good bunch crossing identification can be obtained with the present CMS RPC system, given their fast response of the order of 1 ns. In order to contribute to the precision of muon momentum measurements, muon chambers should have a spatial resolution less or comparable to the contribution of multiple scattering [20]. Most of the plausible physics is covered only considering muons with  $p_T < 100$  GeV thus, in order to match CMS requirements, a spatial resolution of  $\mathcal{O}(\text{few mm})$  the proposed new RPC stations, as shown by the simulation in figure 2.4. According to preliminary designs, RE3/1 and RE4/1 readout pitch will be comprised between 3 and 6 mm and 5  $\eta$ -partitions could be considered.

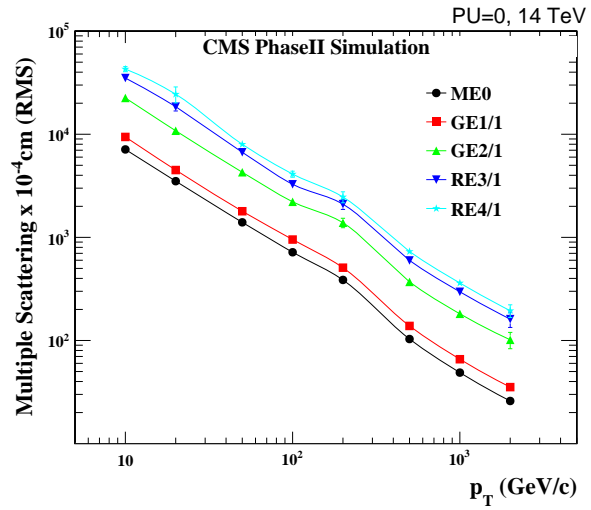


*Figure 2.4: RMS of the multiple scattering displacement as a function of muon p<sub>T</sub> for the proposed forward muon stations. All of the electromagnetic processes such as bremsstrahlung and magnetic field effect are included in the simulation.*



# 3

546

547

## Physics of Resistive plate chambers

548 A Resistive Plate Chamber (RPC) is a gaseous detector using the same physical processes described  
549 in Chapter 3. It has been developed in 1981 by Santonico and Cardarelli [23], under the name of  
550 *Resistive Plate Counter*, as an alternative to the local-discharge spark counters proposed in 1978  
551 by Pestov and Fedotovich [24, 25]. Working with spark chambers implied using high-pressure gas  
552 and high mechanical precision which the RPC simplified by formerly using a gas mixture of argon  
553 and butane flowed at atmospheric pressure and a constant and uniform electric field propagated  
554 in between two parallel electrode plates. Moreover, a significant increase in rate capability was  
555 introduced by the use of electrode plate material with high bulk resistivity, preventing the discharge  
556 from growing throughout the whole gas gap. Indeed, the effect of using resistive electrodes is that  
557 the constant electric field is locally canceled out by the development of the discharge, limiting its  
558 growth.

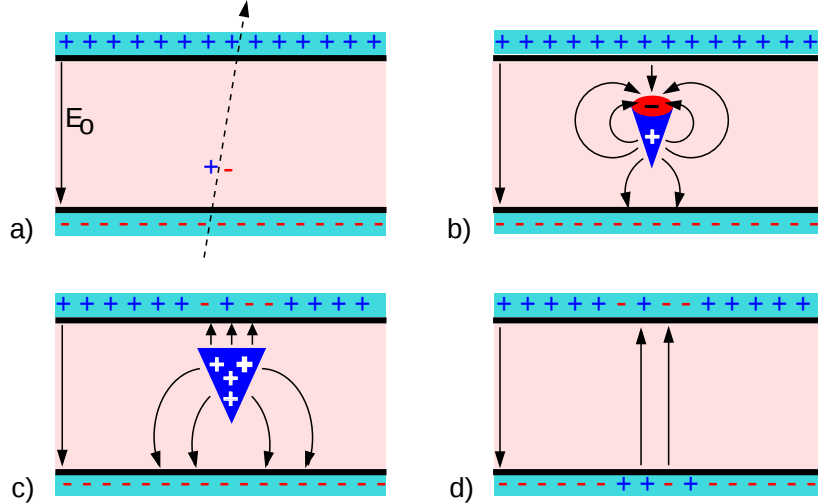
559 Through its development history, different operating modes [26–28] and new detector designs [29–  
560 31] have been discovered, leading to further improvement of the rate capability of such a detector.  
561 Moreover, the addition of  $SF_6$  into the gas mix improved the stability of operation of the RPC [32,  
562 33].

563 The low developing costs and easily achievable large detection areas offered by RPCs, as well as  
564 the wide range of possible designs, made them a natural choice to as muon chambers and/or trigger  
565 detectors in multipurpose experiments such as CMS [20] or ATLAS [34], time-of-flight detectors in  
566 ALICE [35], calorimeter with CALICE [36] or even detectors for volcanic muography with ToMu-  
567 Vol [37].

### 568 3.1 Principle

569 RPCs are ionisation detectors composed of two parallel resistive plate electrodes in between which  
570 a constant electric field is set. The space in between the electrodes, referred as *gap*, is filled with a  
571 dense gas that is used to generate primary ionization into the gas volume. The free charge carriers  
572 (electrons and cations) created by the ionization of the gas molecules are then accelerated towards

573 the electrodes by the electric field, as shown in Figure 3.1 [38].



574 *Figure 3.1: Different phases of the avalanche development in the RPC gas volume subjected to a constant  
575 electric field  $E_0$ . a) An avalanche is initiated by the primary ionisation caused by the passage of a charged  
576 particle through the gas volume. b) Due to its growing size, the avalanche starts to locally influence the electric  
577 field. c) The electrons, lighter than the cations reach the anode first. d) The ions reach the cathode. While  
578 the charges have not recombined, the electric field in the small region around the avalanche stays affected and  
579 locally blind the detector.*

580 RPCs being passive detectors, a current on pick-up copper read-out placed outside of the gas  
581 volume is induced by the charge accumulation during the growth of the avalanche. As a result,  
582 the time resolution of the detector is substantially increased as the output signal is generated while  
583 the electrons are still in movement. The advantage of a constant electric field, over multi-wire  
584 proportional chambers, is that the electrons are being fully accelerated from the moment charge  
585 carriers are freed and feel the full strength of the electric field that doesn't depend on the distance to  
586 the readout and that the output signal doesn't need for the electrons to be physically collected.

587 The typical gas mixture RPCs are operated with is generally composed of 3 gas compounds.

- 588 • Tetrafluoroethane ( $C_2F_4H_2$ ), also referred to as *Freon*, is the principal compound of the RPC  
589 gas mixtures, with a typical fraction above 90%. It is used for it's high effective Townsend  
590 coefficient and the great average fast charge that allows to operate the detector with a high  
591 threshold with respect to argon, for example, that has similar effective Townsend coefficient  
592 but suffers from a lower fast charge. To operate with similar conditions, argon would require a  
593 higher electric field leading to a higher fraction of streamers, thus limiting the rate capability  
594 of the detector [39].
- 595 • Isobutane (i- $C_4H_{10}$ ), only present in a few percent in the gas mixtures, is used for its UV  
596 quenching properties [40] helping to prevent streamers due to UV photon emission during the  
597 avalanche growth.
- 598 • Sulfur hexafluoride, ( $SF_6$ ), referred to simply as *SF6*, is used in very little quantities for its  
599 high electronegativity. Excess of electrons are being absorbed by the compound and streamers

594       are suppressed [33]. Nevertheless, a fraction of  $SF_6$  higher than 1% will not bring any extra  
 595       benefice in terms of streamer cancelation power but will lead to higher operating voltage [32],  
 596       as can be understood through Figure 3.2.

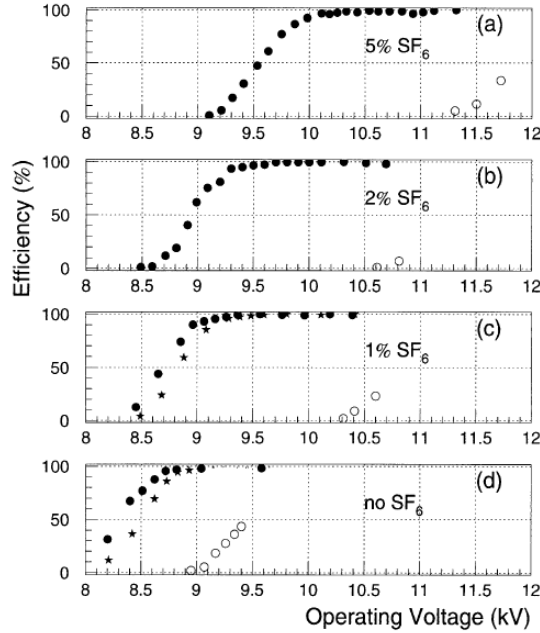


*Figure 3.2: Effeciency (circles and stars with 30 mV and 100 mV thresholds respectively) and streamer probability (opened circles) as function of the operating voltatge of a 2 mm single gap HPL RPC flushed with a gas mixture containing (a) 5%, (b) 2%, (c) 1% and (d) no  $SF_6$  [32].*

597       After an avalanche developed in the gas, a time long compared to the development of a discharge  
 598       is needed to recombine the charge carriers in the electrode material due to their resistivity. This  
 599       property has the advantage of affecting the local electric field and avoiding sparks in the detector  
 600       but, on the other hand, the rate capability is intrinsically limited by the time constant  $\tau_{RPC}$  of the  
 601       detector. Using a quasi-static approximation of Maxwell's equations for weakly conducting media,  
 602       it can be shown that the time constant  $\tau_{RPC}$  necessary to the charge recombination at the interface  
 603       in between the electrode and the gas volume is given by the Formula 3.1 [41].

$$\tau_{RPC} = \frac{\epsilon_{electrode} + \epsilon_{gas}}{\sigma_{electrode} + \sigma_{gas}} \quad (3.1)$$

604       A gas can be assimilated to vacuum, leading to  $\epsilon_{gas} = \epsilon_0$  and  $\sigma_{gas} = 0$ , and the electrodes  
 605       permittivity and conductivity can be written as  $\epsilon_{electrode} = \epsilon_r \epsilon_0$  and  $\sigma_{electrode} = 1/\rho_{electrode}$ ,  
 606       showing the strong dependence of the time constant to the electrodes resistivity in Formula 3.2.

$$\tau_{RPC} = (\epsilon_r + 1)\epsilon_0 \times \rho_{electrode} \quad (3.2)$$

607       Very few materials with a low enough resistivity exist in nature. The resistivity targeted to build  
 608       RPCs ranges from  $10^9$  to  $10^{12} \Omega \cdot \text{cm}$ . The most common RPC electrode materials are displayed in  
 609       Table 3.1. When the doped glass and ceramics can offer short time constants of the order of 1 ms,

610 the developing cost of such materials is quite high due to the very low demand. Thus, High-pressure  
 611 laminate (HPL) is often the choice for high rate experiments using very large RPC detection areas.  
 612 Other experiments working at cosmic muon fluxes can safely operate with ordinary float glass.

Material	$\rho_{electrode}$ ( $\Omega \cdot \text{cm}$ )	$\epsilon_r$	$\tau_{RPC}$ (ms)
Float glass	$10^{12}$	$\sim 7$	$\sim 700$
High-pressure laminate	$10^{10}$ to $10^{12}$	$\sim 6$	$\sim 6$ to 600
Doped glass (LR S)	$10^9$ to $10^{11}$	$\sim 10$	$\sim 1$ to 100
Doped ceramics (SiN/SiC)	$10^9$	$\sim 8.5$	$\sim 1$
Doped ceramics (Ferrite)	$10^8$ to $10^{12}$	$\sim 20$	$\sim 0.2$ to 2000

Table 3.1: Properties of the most used electrode materials for RPCs.

### 613 3.1.1 Electron drift velocity

614 Talk about the electron drift velocity and mention the time resolution of RPCs.

## 615 3.2 Rate capability and time resolution of Resistive Plate Chambers

617 As already previously discussed, the electrode material plays a key role in the max intrinsic rate  
 618 capability of RPCs. R&D is being done to develop at always cheaper costs material with lower  
 619 resistivity. Nevertheless, the amount of charge released, i.e. the size of the discharge, if reduced  
 620 leads to a smaller blind area in the detector, increasing the rate capability of the detector.

### 621 3.2.1 Operation modes

622 RPCs where developed early 1980s. At that time it was using an operating mode now referred to  
 623 as *streamer mode*. Streamers are large discharges that develop in between the 2 electrodes enough  
 624 to locally discharge the electrodes. If the electric field inside of the gas volume is strong enough,  
 625 with electrons being fast compared to ions, a large and dense cloud of positive ions will develop  
 626 nearby the anode and extend toward the cathode while the electrons are being collected, eventually  
 627 leading to a streamer discharge due to the increase of field seen at the cathode. the field is then strong  
 628 enough so that electrons are pulled out of the cathode. Electrodes, though they are a unique volume  
 629 of resistive material, can be assimilated to capacitors. At the moment an electric field is applied in  
 630 between their outer surfaces, the charge carriers inside of the volume will start moving leading to  
 631 a situation where there is no voltage across the electrodes and a higher density of negative charges,  
 632 i.e. electrons, on the inner surface of the cathode. Finally, when a streamer discharge occurs, these  
 633 electrons are partially released in the gas volume contributing to increase the discharge strength until  
 634 the formation of a conductive plasma, the streamer. This can be understood through Figure 3.3 [26].  
 635 Streamer signals are very convenient in terms of read-out as no amplification is required with output  
 636 pulses amplitudes of the order of a few tens to few hundreds of mV as can be seen on Figure 3.4.

637 When the electric field is reduced though, the electronic gain is small until the electrons get close  
 638 enough to the anode and the positive ion cloud is much smaller. The electric field cannot rise to the  
 639 point a field emission of electrons on the cathode is possible. The resulting signal is weak, of the

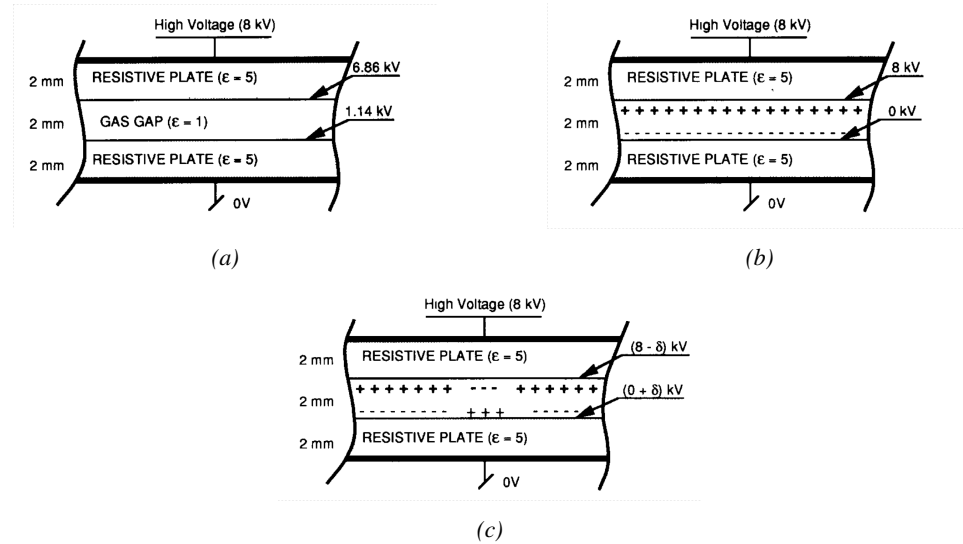


Figure 3.3: Movement of the charge carriers in an RPC. Figure 3.3a: Voltage across an RPC whose electrode have a relative permittivity of 5 at the moment the tension is applied. Figure 3.3b: After the charge carriers moved, the electrodes are charged and there is no voltage drop over the electrodes anymore. The full potential is applied on the gas gap only. Figure 3.3c: The streamer discharge initiated by a charged particle transports electrons and cations towards the anode and cathode respectively.

order of a few mv as shown on Figure 3.4, and requires amplification. This is the *avalanche mode* of RPC operation.

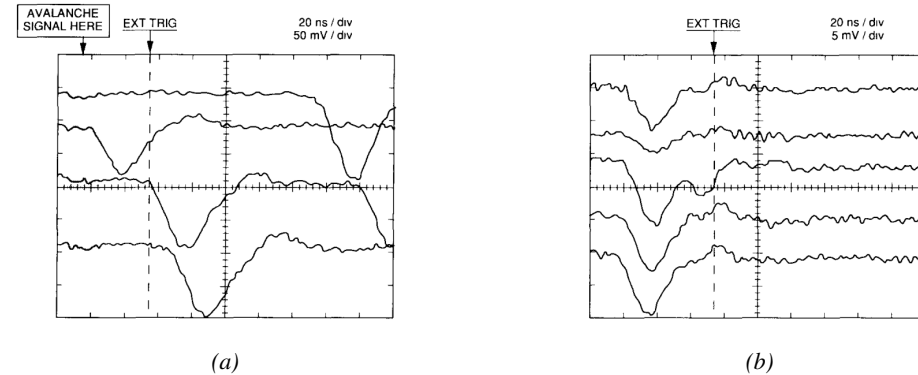


Figure 3.4: Typical oscilloscope pulses in streamer mode (Figure 3.4a) and avalanche mode (Figure 3.4b). In the case of streamer mode, the very small avalanche signal is visible.

This mode offers a higher rate capability by providing smaller discharges that don't affect the electrodes charge and are more locally contained in the gas volume as was demonstrated by Crotty with Figure 3.5 [26]. The detector only stays locally blind the time the charge carriers are recombined and there is no need for electrode recharge which is a long process affecting a large portion of the detector. Another advantage of avalanche signals over streamer is the great time consistency. Figure 3.4 shows very clearly that avalanche signals have a very small time jitter. This is a natural choice for high rate experiments.

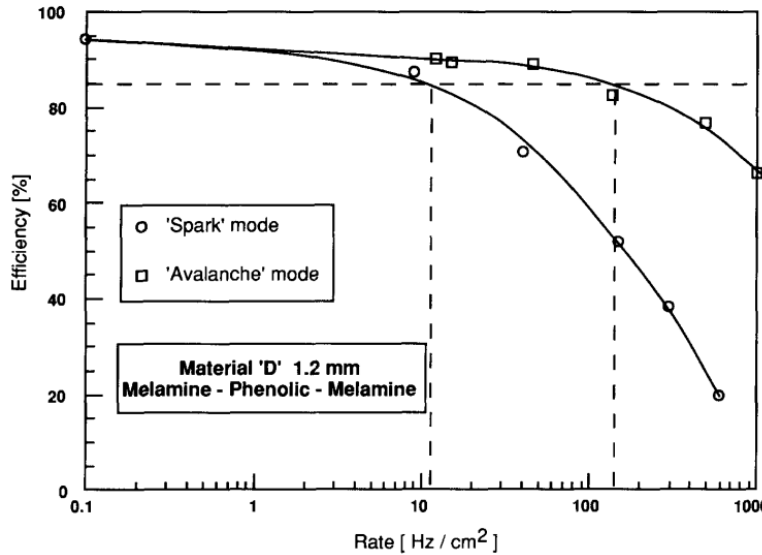


Figure 3.5: Rate capability comparison for the streamer and avalanche mode of operation. An order of magnitude in rate capability for a maximal efficiency drop of 10% is gained by using the avalanche mode over the streamer mode.

### 649 3.2.2 Detector designs and performance

650 Different RPC design have been used and each of them present its own advantages. Historically,  
 651 the first type of RPC to have been developed is what is referred now to *no narrow gap* RPC [23, 42].  
 652 After the avalanche mode has been discovered [26], it has been proven that increasing the width  
 653 of the gas gap lead to higher rate capability, due to lower charge deposition per avalanche, and  
 654 lower power dissipation [42]. Nevertheless, by increasing the gas gap width, the time resolution of  
 655 the detector decreases. This is a natural result if the increase of active gas volume in the detector is  
 656 taken into account. Indeed, for a given threshold, only the small fraction of gas closest to the cathode  
 657 will provide enough gain to have a detectable signal. In the case of a wider gas volume, the active  
 658 region is then larger and a larger time jitter is introduced with the variation of starting position of the  
 659 avalanche, as discussed in [29]. To solve improve both the time resolution and the rate capability,  
 660 different methods were used trying to get advantages of both narrow and wide gap RPCs.

#### 661 3.2.2.1 Double-gap RPC

662 Double-gap RPCs are made out of 2 narrow RPC detectors. The 2 RPC gaps are stacked on top of  
 663 each other as shown in Figure 3.6. This detector layout, popularized by the two multipurpose experi-  
 664 ments CMS [20] and ATLAS [34] at LHC, can be used as an OR system in which each individual  
 665 chamber participates in the output signal. The gain of such a detector is greatly reduced with respect  
 666 to single-gap RPCs with an efficiency plateau reached at lower voltage, as visible on Figure 3.7.

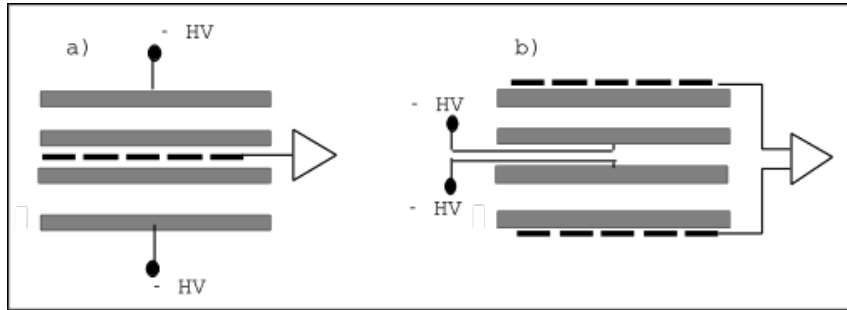


Figure 3.6: Possible double-gap RPC layouts: a) "standard" 1D double-gap RPC, as used in CMS experiment, where the anodes are facing each other and a 1D read-out plane is sandwiched in between them, b) double read-out double-gap RPC as used in ATLAS experiment, where the cathodes are facing each other and 2 read-out planes are used on the outer surfaces. This last layout can offer the possibility to use a 2D reconstruction by using orthogonal read-out planes.

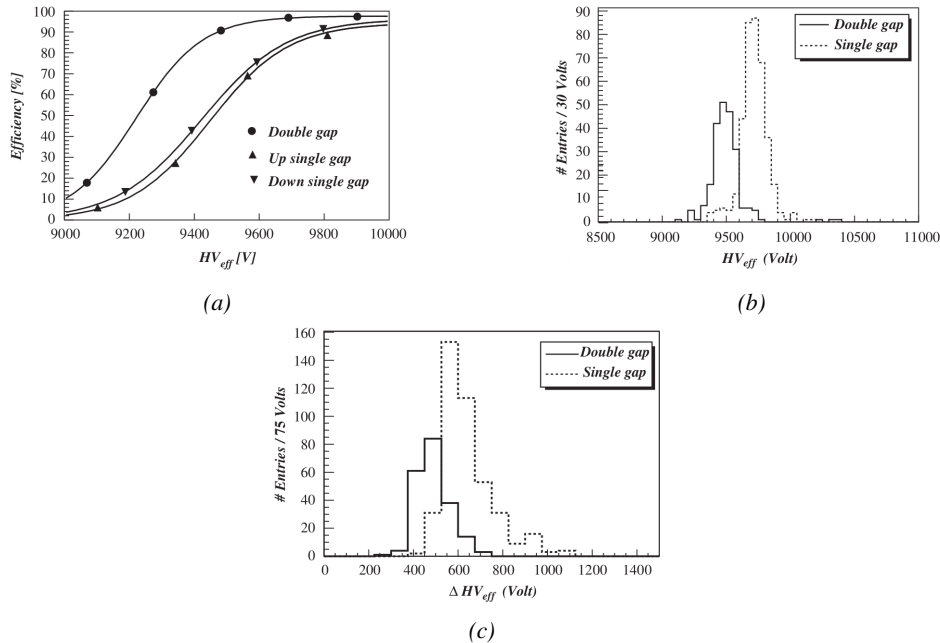
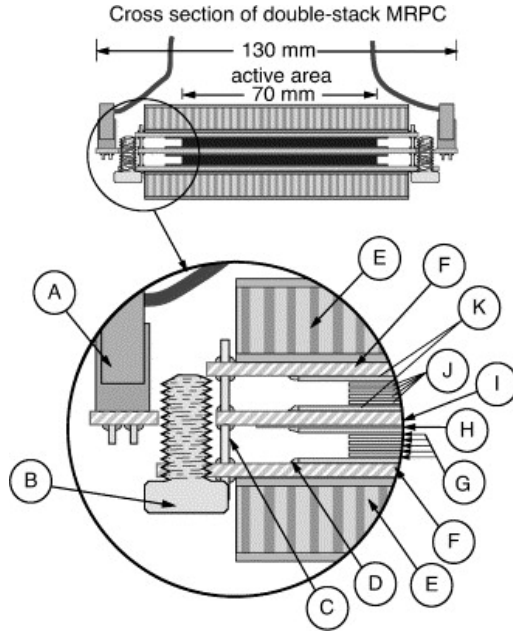


Figure 3.7: Comparison of performance of CMS double and single gap RPCs using cosmic muons [43]. Figure 3.7a: Comparison of efficiency sigmoids. Figure 3.7b: Voltage distribution at 95% of maximum efficiency. Figure 3.7c:  $\Delta_{10\%}^{90\%}$  distribution.

### 667 3.2.2.2 Multigap RPC (MRPC)

668 MRPCs are layouts in which floating sub electrode plates are placed into a wide gap RPC to divide  
 669 the gas volume and create a sum of narrow gaps [29, 30]. The time resolution of such a detector can  
 670 reach of few tens of ps, with gas gaps of the order of a few hundred  $\mu\text{m}$  as shown in Figure 3.8  
 671 representing ALICE Time-of-flight (ToF) MRPCs.

672 Sometimes used as a double multigap RPC, taking advantage of the OR of double gap RPCs,  
 673 the MRPC is mainly used as ToF detector [44–48] due to its excellent timing properties that allow



*Figure 3.8: Presentation of ALICE MRPC using 250  $\mu\text{m}$  gas gaps, 620  $\mu\text{m}$  outer glass electrodes and 550  $\mu\text{m}$  inner floating electrodes. More details on the labels are given in [44].*

674 to perform particle identification as explained by Williams in [49]. The principle of particle iden-  
 675 tification using ToF is simply the measurement of the velocity of a particle. Indeed, particles are  
 676 defined by their mass (for the parameter of interest here, their electric charge being measured using  
 677 the bending angle of the particles traveling through a magnetic field) and this mass can be calculated  
 678 by measuring the velocity  $\beta$  and momentum of the particle:

$$\beta = \frac{p}{\sqrt{p^2 + m^2}} \quad (3.3)$$

679 Intuitively, it is trivial to understand that 2 different particles having the same momentum will  
 680 have a different velocity due to the mass difference and thus a different flight time  $T_1$  and  $T_2$  through  
 681 the detector and this is used to separate and identify particles. The better the time resolution of the  
 682 ToF system used, the stronger will the separation be:

$$T = \frac{L}{v} = \frac{L}{c \cdot \beta}, \quad \Delta T = T_1 - T_2 = \frac{L}{c} \left( \sqrt{1 + m_1^2/p^2} - \sqrt{1 + m_2^2/p^2} \right) \cong (m_1^2 - m_2^2) \frac{L}{2cp^2} \quad (3.4)$$

683 An example of particle identification is given for the case of STAR experiment in Figure 3.9.

684 Another benefit of using such small gas gaps is the strong reduction of the average avalanche  
 685 volume and thus of the blind spot on MRPCs leading to an improved rate capability. Multigaps can  
 686 sustain backgrounds of several kHz/cm<sup>2</sup> as demonstrated in Figure 3.10.

### 687 3.2.2.3 Charge distribution and performance limitations

688 The direct consequence of the different RPC layouts is a variation of intrinsic time resolution of the  
 689 RPC as the gap size decreases. An advantage is given to multigaps whose design use sub-millimeter

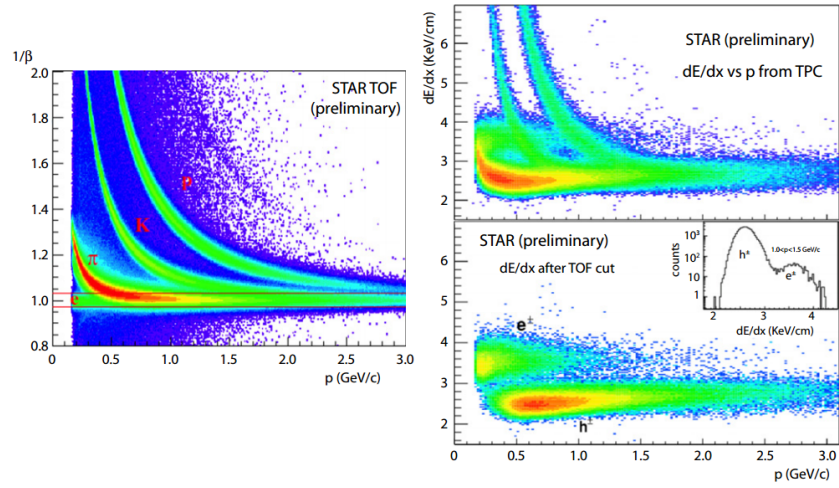


Figure 3.9: Particle identification applied to electrons in the STAR experiment. The identification is performed combining ToF and  $dE/dx$  measurements [49].

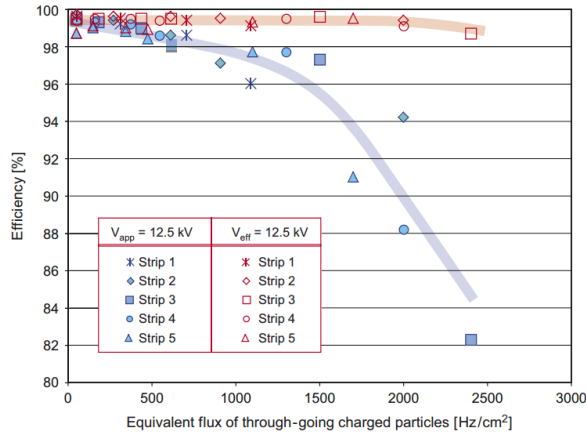


Figure 3.10: Comparison of the detector performance of ALICE ToF MRPC [50] at fixed applied voltage (in blue) and at fixed effective voltage (in red). The effective voltage is kept fixed by increasing the applied voltage accordingly to the current drawn by the detector.

690 gas volumes providing very consistent signals.

691 On the charge spectrum point of view, each layout has its own advantages. When the double-gap  
 692 has the highest induced over drifting charge ratio, as seen in Figure 3.11, the multigap has a charge  
 693 spectrum strongly detached from the origin, as visible in Figure 3.12. A high induced over drifting  
 694 charge ratio means that the double gap can be safely operated at high threshold or that at similar  
 695 threshold it can be operated with a twice smaller drifting charge, meaning a higher rate capability.  
 696 On the other hand, the strong detachment of the charge spectrum from the origin in the MRPC case  
 697 allows to reach a higher efficiency with increasing threshold as most of the induced charge is not low  
 698 due to the convolution of several single gap spectra. The range of stable efficiency increases with  
 699 the number of gap, as presented in Figure 3.13.

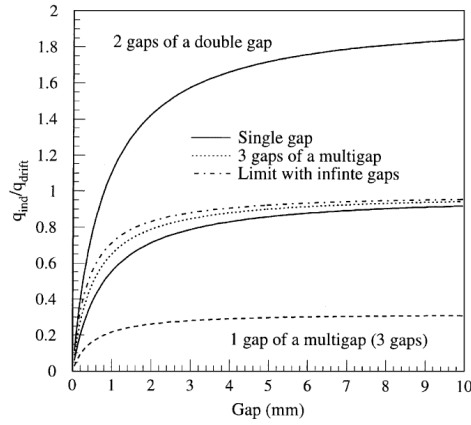


Figure 3.11: Ratio between total induced and drifting charge have been simulated for single gap, double-gap and multigap layouts [51]. The total induced charge for a double-gap RPC is a factor 2 higher than for a multigap.

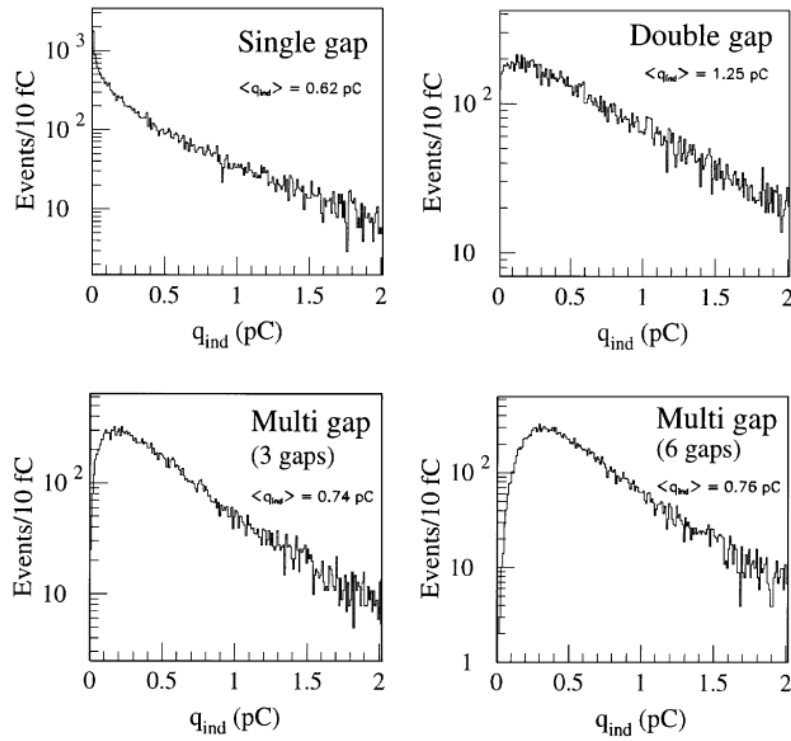
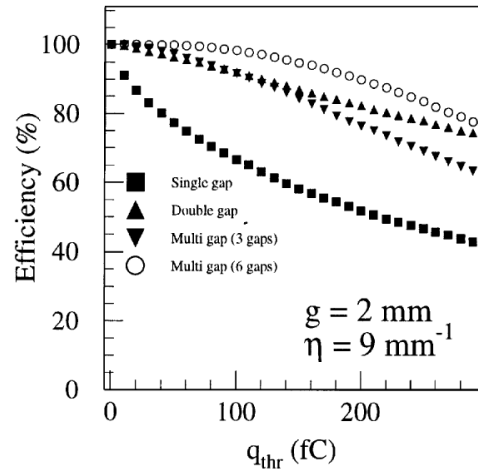


Figure 3.12: Charge spectra have been simulated for single gap, double-gap and multigap layouts [51]. It appears that when single gap shows a decreasing spectrum, double and multigap layouts exhibit a spectrum whose peak is detached from the origin. The detachment gets stronger as the number of gaps increases.



*Figure 3.13: The maximal theoretical efficiency is simulated for single gap, double-gap and multigap layouts [51] at a constant gap thickness of 2 mm and using an effective Townsend coefficient of  $9 \text{ mm}^{-1}$ .*

### 700    3.3 Signal formation

### 701    3.4 Gas transport parameters



# 4

702

703

704

## Longevity studies and Consolidation of the present CMS RPC subsystem

705

### 4.1 Resistive Plate Chambers at CMS

706

#### 4.1.1 Overview

707

The Resistive Plate Chambers (RPC) system, located in both barrel and endcap regions, provides a fast, independent muon trigger with a looser  $p_T$  threshold over a large portion of the pseudorapidity range ( $|\eta| < 1.6$ ) [\[add reconstruction\]](#).

710

711

During High-Luminosity LHC (HL-LHC) operations the expected conditions in terms of background and pile-up will make the identification and correct  $P_T$  assignment a challenge for the Muon system. The goal of RPC upgrade is to provide additional hits to the Muon system with precise timing. All these informations will be elaborated by the trigger system in a global way enhancing the performance of the trigger in terms of efficiency and rate control. The RPC Upgrade is based on two projects: an improved Link Board System and the extension of the RPC coverage up to  $|\eta| = 2.4$ . [\[FIXME 2.4 or 2.5?\]](#)

712

713

714

715

716

717

The Link Board system, that will be described in section xxx, is responsible to process, synchronize and zero-suppress the signals coming from the RPC front end boards. The Link Board components have been produced between 2006 and 2007 and will be subjected to aging and failure in the long term. The upgraded Link Board system will overcome the aging problems described in section xxx and will allow for a more precise timing information to the RPC hits from 25 to 1 ns [ref section xxx].

718

719

720

721

722

723

The extension of the RPC system up to  $|\eta| = 2.1$  was already planned in the CMS TDR [ref cmstdr] and staged because of budget limitations and expected background rates higher than the rate capability of the present CMS RPCs in that region. An extensive R&D program has been done in order to develop an improved RPC that fulfills the CMS requirements. Two new RPC layers in the innermost ring of stations 3 and 4 will be added with benefits to the neutron-induced background

729 reduction and efficiency improvement for both trigger and offline reconstruction.

### 730 4.1.2 The present RPC system

731 The RPC system is organized in 4 stations called RB1 to RB4 in the barrel region, and RE1 to RE4  
 732 in the endcap region. The innermost barrel stations, RB1 and RB2, are instrumented with 2 layers  
 733 of RPCs facing the innermost (RB1in and RB2in) and outermost (RB1out and RB2out) sides of the  
 734 DT chambers. Every chamber is then divided from the read-out point of view into 2 or 3  $\eta$  partitions  
 735 called “rolls”. The RPC system consist of 480 barrel chambers and 576 endcap chambers. Details  
 736 on the geometry are discussed in the paper [ref to geo paper].

737 The CMS RPC chamber is a double-gap, operated in avalanche mode to ensure reliable operation  
 738 at high rates. Each RPC gap consists of two 2-mm-thick resistive High-Pressure Laminate (HPL)  
 739 plates separated by a 2-mm-thick gas gap. The outer surface of the HPL plates is coated with a thin  
 740 conductive graphite layer, and a voltage is applied. The RPCs are operated with a 3-component,  
 741 non-flammable gas mixture consisting of 95.2% freon ( $C_2H_2F_4$ , known as R134a), 4.5% isobutane  
 742 ( $i-C_4H_{10}$ ), and 0.3% sulphur hexafluoride ( $SF_6$ ) with a relative humidity of 40% - 50%. Readout  
 743 strips are aligned in  $\eta$  between the 2 gas gaps. [\[Add a sentence on FEBs.\]](#)

744 The discriminated signals coming from the Front End boards feed via twisted cables (10 to 20 m  
 745 long) the Link Board System located in UXC on the balconies around the detector. The Link System  
 746 consist of the 1376 Link Boards (LBs) and the 216 Control Boards (CBs), placed in 108 Link Boxes.  
 747 The Link Box is a custom crate (6U high) with 20 slots (for two CBs and eighteen LBs). The Link  
 748 Box contains custom backplane to which the cables from the chambers are connected, as well as the  
 749 cables providing the LBs and CBs power supply and the cables for the RPC FEBs control with use  
 750 of the I2C protocol (trough the CB). The backplane itself contains only connectors (and no any other  
 751 electronic devices).

752 The Link Board has 96 input channels (one channel corresponds to one RPC strip). The input  
 753 signals are the  $\sim 100$  ns binary pulses which are synchronous to the RPC hits, but not to the LHC  
 754 clock (which drives the entire CMS electronics). Thus the first step of the FEB signals processing  
 755 is synchronization, i.e. assignment of the signals to the BXes (25 ns periods). Then the data are  
 756 compressed with a simple zero-suppressing algorithm (the input channels are grouped into 8 bit  
 757 partitions, only the partitions with at least one nonzero bit are selected for each BX). Next, the non-  
 758 empty partitions are time-multiplexed i.e. if there are more than one such partition in a given BX,  
 759 they are sent one-by-one in consecutive BXes. The data from 3 neighbouring LBs are concentrated  
 760 by the middle LB which contains the optical transmitter for sending them to the USC over a fiber at  
 761 1.6 Gbps.

762 The Control Boards provide the communication of the control software with the LBs via the  
 763 FEC/CCU system. The CBs are connected into token rings, each ring consists of 12 CBs of one  
 764 detector tower and a FEC mezzanine board placed on the CCS board located in the VME crate in  
 765 the USC. In total, there are 18 rings in the entire Link System. The CBs also perform automatic  
 766 reloading of the LB's firmware which is needed in order to avoid accumulation of the radiation  
 767 induced SEUs in the LBs firmware.

768 Both LBs and CB are based on the Xilinx Spartan III FPGAs, the CB additionally contains  
 769 radiation-tolerant (FLASH based) FPGA Actel ProAsicPlus.

770 The High Voltage power system is located in USC, not exposed to radiation and easily accessible  
 771 for any reparation. A single HV channel powers 2 RPC chambers both in the barrel and endcap  
 772 regions. The Low Voltage boards are located in UXC on the balconies and provide the voltage to the

773 front end electronics.

### 774 4.1.3 Pulse processing of CMS RPCs

775 Signals induced by cosmic particle in the RPC strips are shaped by standard CMS RPC Front-End  
 776 Electronics (FEE) following the scheme of Figure 4.1. On a first stage, analogic signals are amplified  
 777 and then sent to the Constant Fraction Discriminator (CFD) described in Figure 4.2. At the end of  
 778 the chain, 100 ns long pulses are sent in the LVDS output. These output signal are sent on one side to  
 779 a V1190A Time-to-Digital Converter (TDC) module from CAEN and on the other to an OR module  
 780 to count the number of detected signals. Trigger and hit coïncidences are monitored using scalers.  
 781 The TDC is used to store the data into ROOT files. These files are thus analysed to understand the  
 782 detectors performance.

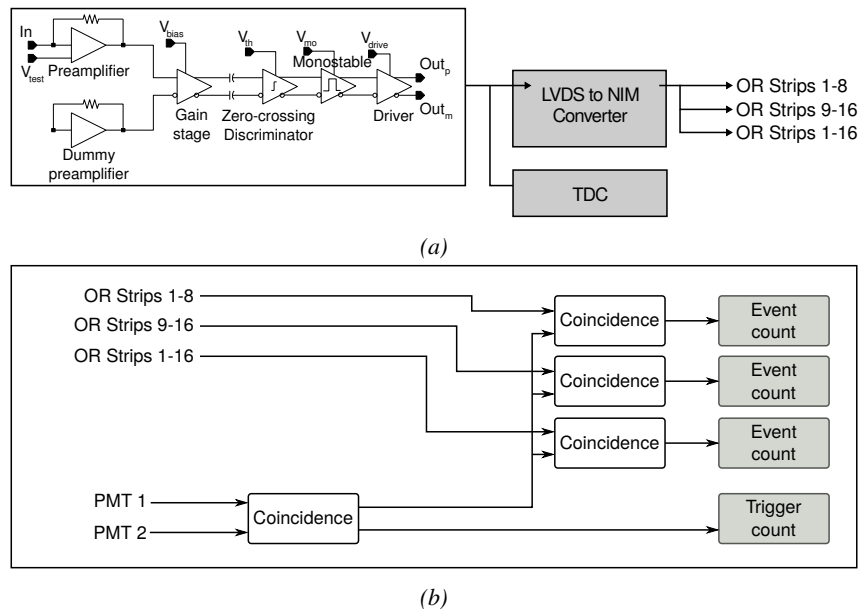
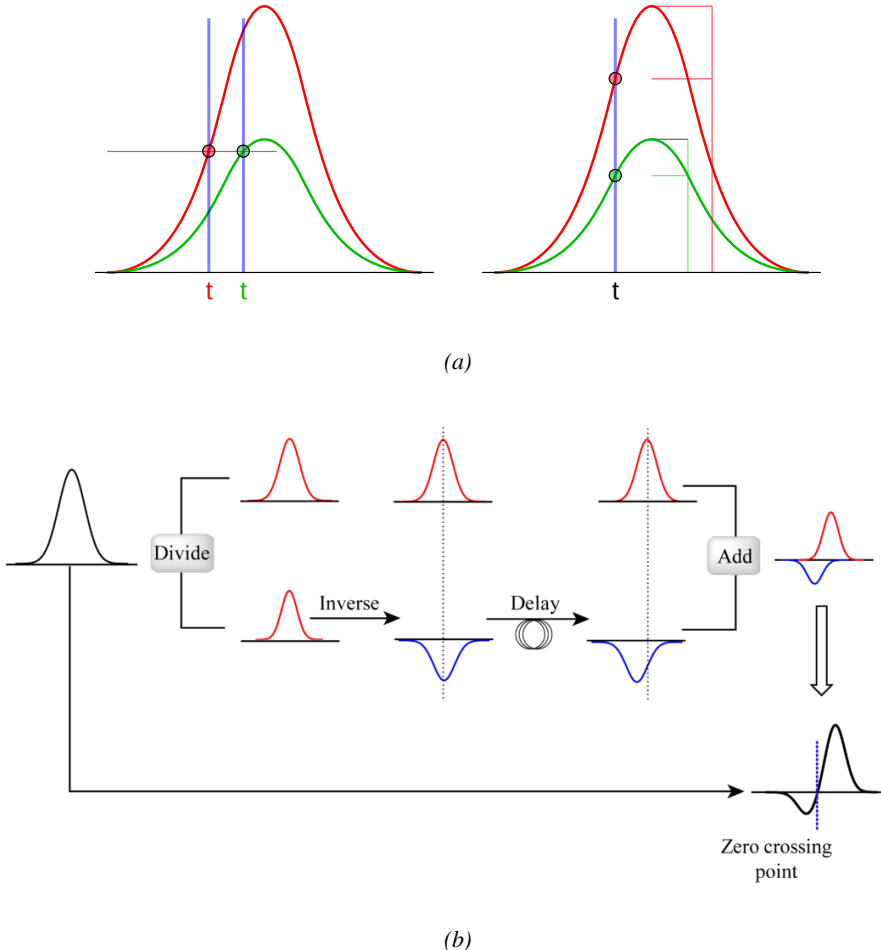


Figure 4.1: Signals from the RPC strips are shaped by the FEE described on Figure 4.1a. Output LVDS signals are then read-out by a TDC module connected to a computer or converted into NIM and sent to scalers. Figure 4.1b describes how these converted signals are put in coincidence with the trigger.

## 783 4.2 Testing detectors under extreme conditions

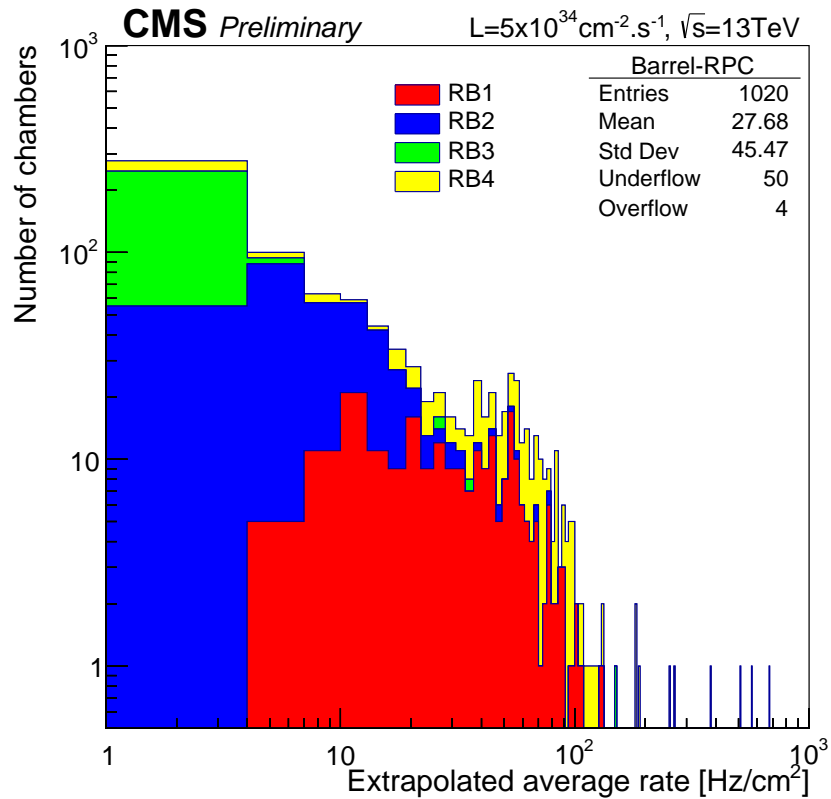
784 The upgrade from LHC to HL-LHC will increase the peak luminosity from  $10^{34} \text{ cm}^{-2} \text{ s}^{-1}$  to reach  
 785  $5 \times 10^{34} \text{ cm}^{-2} \text{ s}^{-1}$ , increasing in the same way the total expected background to which the RPC  
 786 system will be subjected to. Composed of low energy gammas and neutrons from  $p$ - $p$  collisions, low  
 787 momentum primary and secondary muons, puch-through hadrons from calorimeters, and particles  
 788 produced in the interaction of the beams with collimators, the background will mostly affect the  
 789 regions of CMS that are the closest to the beam line, i.e. the RPC detectors located in the endcaps.  
 790 [To update.]

791

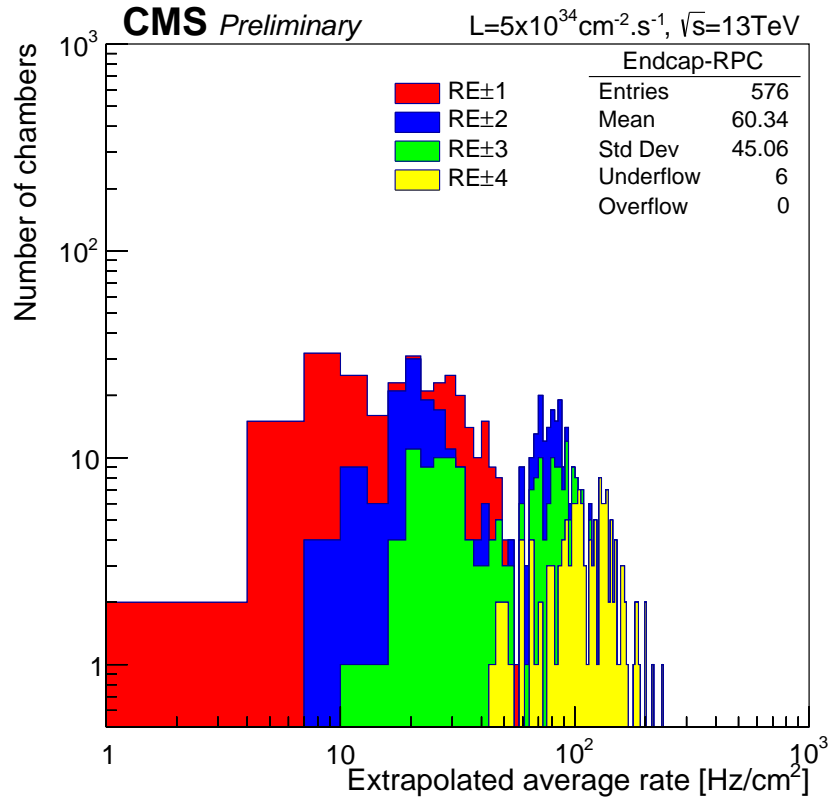


*Figure 4.2: Description of the principle of a CFD. A comparison of threshold triggering (left) and constant fraction triggering (right) is shown in Figure 4.2a. Constant fraction triggering is obtained thanks to zero-crossing technique as explained in Figure 4.2b. The signal arriving at the input of the CFD is split into three components. A first one is delayed and connected to the inverting input of a first comparator. A second component is connected to the noninverting input of this first comparator. A third component is connected to the noninverting input of another comparator along with a threshold value connected to the inverting input. Finally, the output of both comparators is fed through an AND gate.*

792     The 2016 data allowed to study the values of the background rate in all RPC system. In Figure  
 793     the distribution of the chamber background hit rate per unit area is shown at a luminosity  
 794     of  $5 \times 10^{34} \text{ cm}^{-2} \cdot \text{s}^{-1}$  linearly extrapolating from data collected in 2016 [ref mentioning the linear  
 795     dependency of rate vs lumi]. The maximum rate per unit area at HL-LHC conditions is expected to  
 796     be of the order of  $600 \text{ Hz/cm}^2$  (including a safety factor 3). Nevertheless, Fluka simulations have  
 797     conducted in order to understand the background at HL-LHC conditions. The comparison to the  
 798     data has shown, in Figure 4.4, a discrepancy of a factor 2 even though the order of magnitude is  
 799     consistent. [Understand mismatch.]



(a)



(b)

Figure 4.3: (4.3a) Extrapolation from 2016 data of single hit rate per unit area in the barrel region. (4.3b) Extrapolation from 2016 data of single hit rate per unit area in the endcap region.

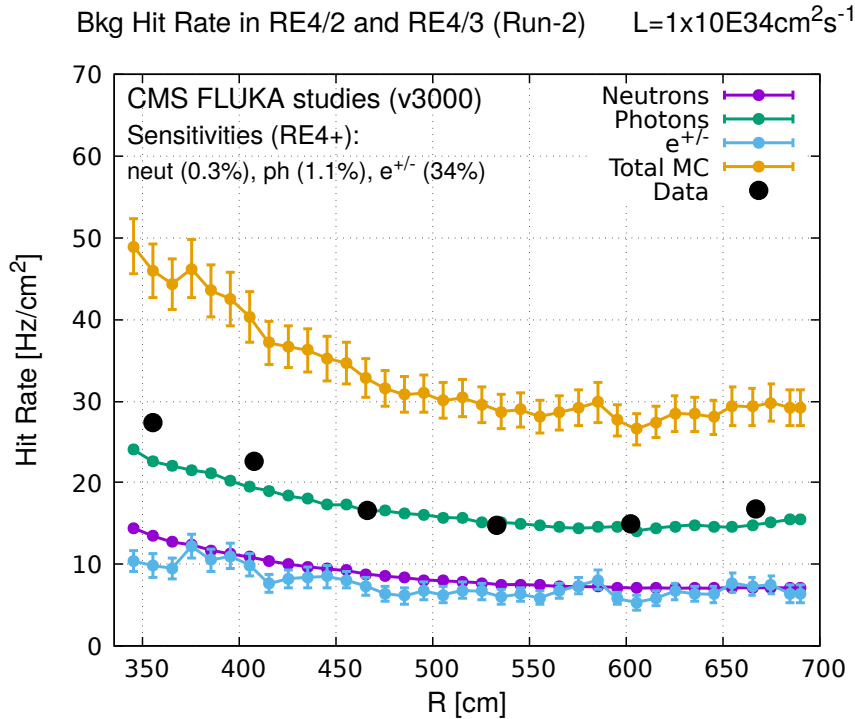


Figure 4.4: Background Fluka simulation compared to 2016 Data at  $L = 10^{34} \text{ cm}^{-2} \cdot \text{s}^{-1}$  in the fourth endcap disk region. A mismatch in between simulation and data can be observed. [\[To be understood.\]](#)

In the past, extensive long-term tests were carried out at several gamma and neutron facilities certifying the detector performance. Both full size and small prototype RPCs have been irradiated with photons up to an integrated charge of  $\sim 0.05 \text{ C}/\text{cm}^2$  and  $\sim 0.4 \text{ C}/\text{cm}^2$ , respectively [52, 53]. During Run-I, the RPC system provided stable operation and excellent performance and did not show any aging effects for integrated charge of the order of  $0.01 \text{ C}/\text{cm}^2$ . Projections on currents from 2016 Data, has allowed to determine that the total integrated charge, by the end of HL-LHC, would be of the order of  $1 \text{ C}/\text{cm}^2$  (including a safety factor 3). [\[Corresponding figure needed.\]](#)

808

## 809 4.2.1 The Gamma Irradiation Facilities

### 810 4.2.1.1 GIF

811 Located in the SPS West Area at the downstream end of the X5 test beam, the Gamma Irradiation  
 812 Facility (GIF) was a test area in which particle detectors were exposed to a particle beam in presence  
 813 of an adjustable gamma background [54]. Its goal was to reproduce background conditions these  
 814 detectors would suffer in their operating environment at LHC. GIF layout is shown in Figure 4.5.  
 815 Gamma photons are produced by a strong  $^{137}\text{Cs}$  source installed in the upstream part of the zone  
 816 inside a lead container. The source container includes a collimator, designed to irradiate a  $6 \times 6 \text{ m}^2$   
 817 area at 5 m maximum to the source. A thin lens-shaped lead filter helps providing with a uniform  
 818 outgoing flux in a vertical plane, orthogonal to the beam direction. The principal collimator hole  
 819 provides a pyramidal aperture of  $74^\circ \times 74^\circ$  solid angle and provides a photon flux in a pyramidal vol-

ume along the beam axis. The photon rate is controled by further lead filters allowing the maximum rate to be limited and to vary within a range of four orders of magnitude. Particle detectors under test are then placed within the pyramidal volume in front of the source, perpendicularly to the beam line in order to profit from the homogeneous photon flux. Adjusting the background flux of photons can then be done by using the filters and choosing the position of the detectors with respect to the source.

825

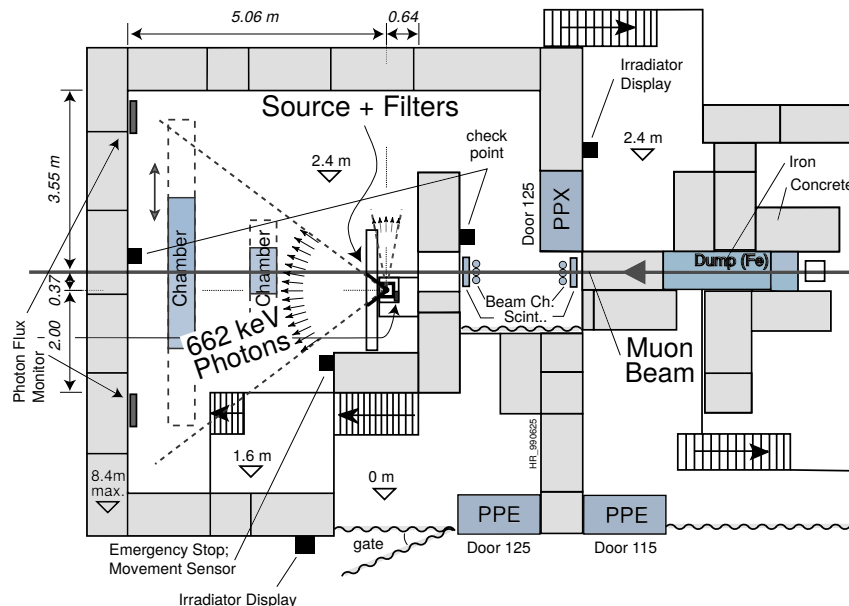


*Figure 4.5: Layout of the test beam zone called X5c GIF at CERN. Photons from the radioactive source produce a sustained high rate of random hits over the whole area. The zone is surrounded by 8 m high and 80 cm thick concrete walls. Access is possible through three entry points. Two access doors for personnel and one large gate for material. A crane allows installation of heavy equipment in the area.*

As described on Figure 4.6, the  $^{137}\text{Cs}$  source emits a 662 keV photon in 85% of the decays. An activity of 740 GBq was measured on the 5<sup>th</sup> March 1997. To estimate the strength of the flux in 2014, it is necessary to consider the nuclear decay through time associated to the Cesium source whose half-life is well known ( $t_{1/2} = (30.05 \pm 0.08)$  y). The GIF tests were done in between the 20<sup>th</sup> and the 31<sup>st</sup> of August 2014, i.e. at a time  $t = (17.47 \pm 0.02)$  y resulting in an attenuation of the activity from 740 GBq in 1997 to 494 GBq in 2014.

832

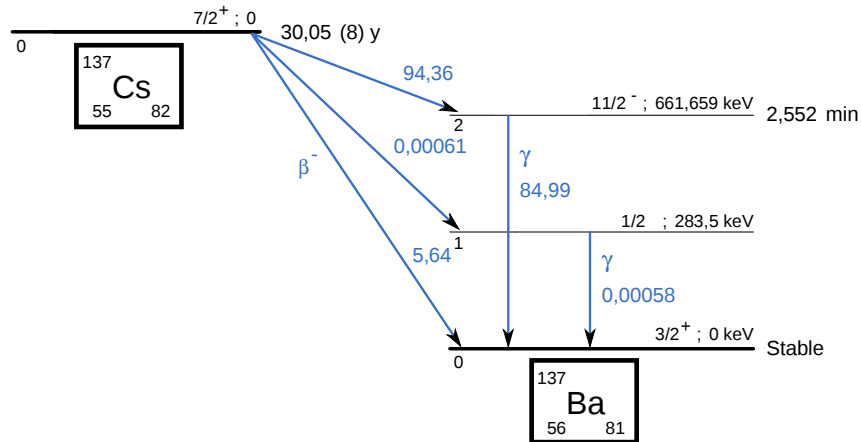


Figure 4.6:  $^{137}\text{Cs}$  decays by  $\beta^-$  emission to the ground state of  $^{137}\text{Ba}$  ( $\text{BR} = 5.64\%$ ) and via the 662 keV isomeric level of  $^{137}\text{Ba}$  ( $\text{BR} = 94.36\%$ ) whose half-life is 2.55 min.

### 4.2.1.2 GIF++

The new Gamma Irradiation Facility (GIF++), located in the SPS North Area at the downstream end of the H4 test beam, has replaced its predecessor during LS1 and has been operational since spring 2015 [55]. Like GIF, GIF++ features a  $^{137}\text{Cs}$  source of 662 keV gamma photons, their fluence being controlled with a set of filters of various attenuation factors. The source provides two separated large irradiation areas for testing several full-size muon detectors with continuous homogeneous irradiation, as presented in Figure 4.7.

840

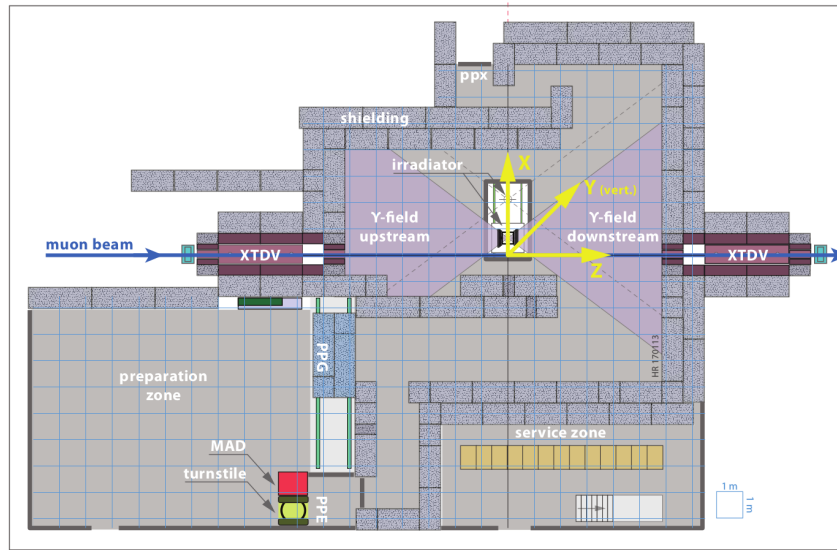


Figure 4.7: Floor plan of the GIF++ facility. When the facility downstream of the GIF++ takes electron beam, a beam pipe is installed along the beam line ( $z$ -axis). The irradiator can be displaced laterally (its center moves from  $x = 0.65 \text{ m}$  to  $2.15 \text{ m}$ ), to increase the distance to the beam pipe.

841 The source activity was measured to be about 13.5 TBq in March 2016. The photon flux being  
 842 far greater than HL-LHC expectations, GIF++ provides an excellent facility for accelerated aging  
 843 tests of muon detectors.

844

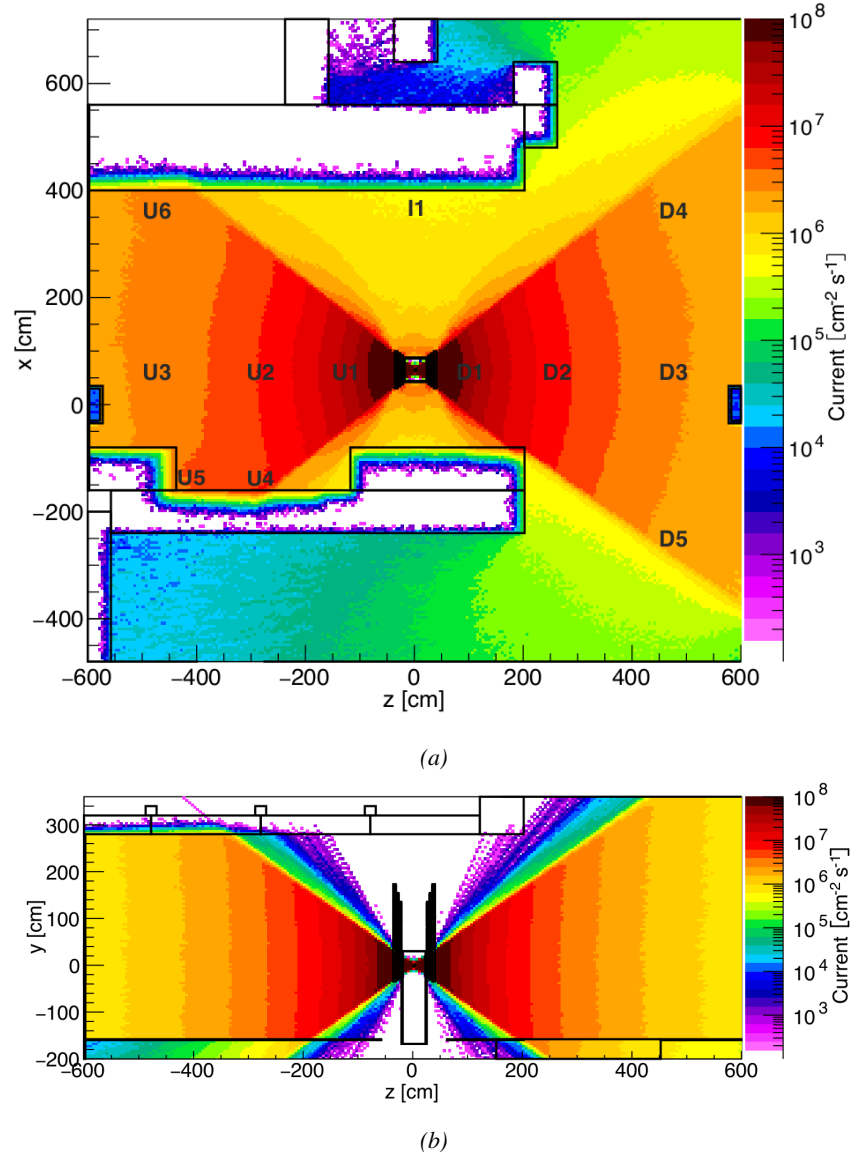


Figure 4.8: Simulated unattenuated current of photons in the xz plane (Figure 4.8a) and yz plane (Figure 4.8b) through the source at  $x = 0.65$  m and  $y = 0$  m. With angular correction filters, the current of 662 keV photons is made uniform in xy planes.

845 The source is situated in the muon beam line with the muon beam being available a few times a  
 846 year. The H4 beam, composed of muons with a momentum of about 150 GeV/c, passes through the  
 847 GIF++ zone and is used to study the performance of the detectors. Its flux is of 104 particles/ $\text{cm}^2$

848 focused in an area similar to  $10 \times 10 \text{ cm}^2$ . Therefore, with properly adjusted filters, one can imitate  
 849 the HL-LHC background and study the performance of muon detectors with their trigger/readout  
 850 electronics in HL-LHC environment.

851

## 852 4.3 Preliminary tests at GIF

### 853 4.3.1 Resistive Plate Chamber test setup

854 During summer 2014, preliminary tests have been conducted in the GIF area on a newly produced  
 855 RE4/2 chamber labelled RE-4-2-BARC-161. This chamber has been placed into a trolley covered  
 856 with a tent. The position of the RPC inside the tent and of the tent related to the source is described  
 857 in Figure 4.9. To test this CMS RPC, three different absorber settings were used. First of all,  
 858 measurements were done with fully opened source. Then, to complete this preliminary study, the  
 859 gamma flux has been attenuated from a factor 2 and a factor 5. The expected gamma flux at the level  
 860 of our detector will be discussed in subsection ??.

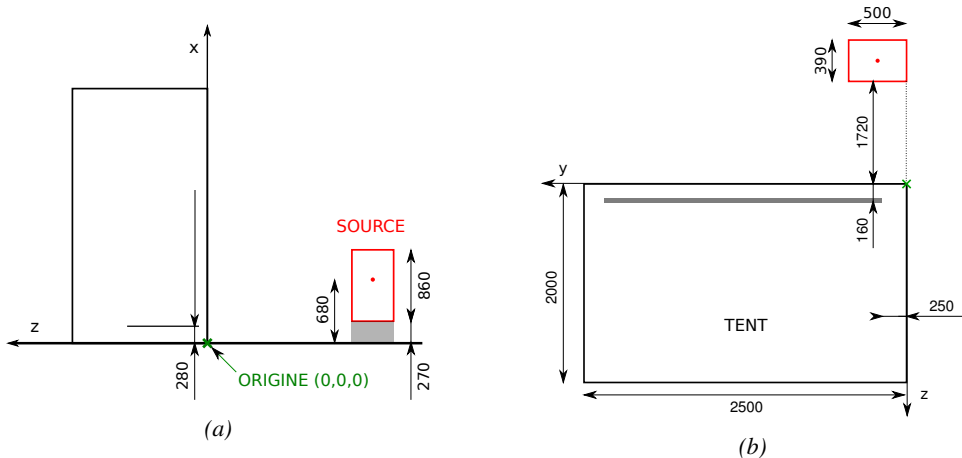
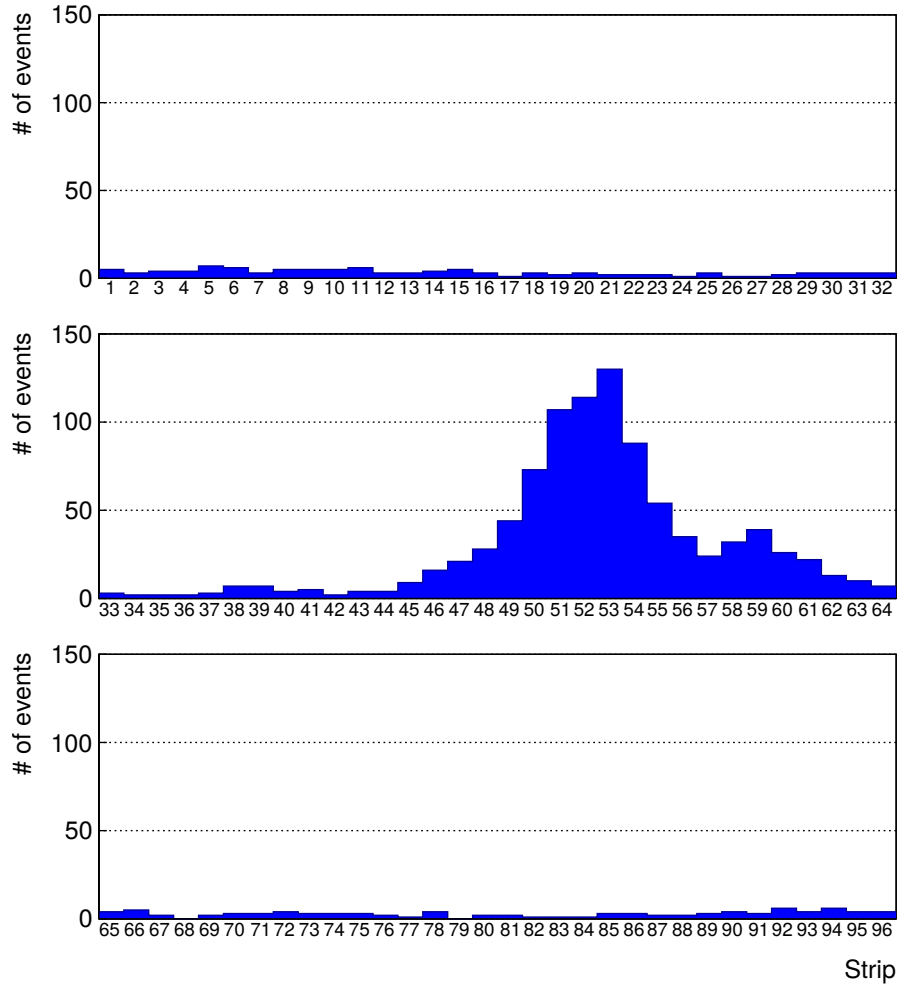


Figure 4.9: Description of the RPC setup. Dimensions are given in mm. A tent containing RPCs is placed at 1720 mm from the source container. The source is situated in the center of the container. RE-4-2-BARC-161 chamber is 160 mm inside the tent. This way, the distance between the source and the chambers plan is 2060 mm. Figure 4.9a provides a side view of the setup in the xz plane while Figure 4.9b shows a top view in the yz plane.



*Figure 4.10: RE-4-2-BARC-I61 chamber is inside the tent as described in Figure 4.9. In the top right, the two scintillators used as trigger can be seen. This trigger system has an inclination of 10° relative to horizontal and is placed above half-partition B2 of the RPCs. PMT electronics are shielded thanks to lead blocks placed in order to protect them without stopping photons from going through the scintillators and the chamber.*

861 At the time of the tests, the beam not being operational anymore, a trigger composed of 2 plastic  
 862 scintillators has been placed in front of the setup with an inclination of 10 deg with respect to the  
 863 detector plane in order to look at cosmic muons. Using this particular trigger layout, shown on Fig-  
 864 ure 4.10, leads to a cosmic muon hit distribution into the chamber similar to the one in Figure 4.11.  
 865 Measured without gamma irradiation, two peaks can be seen on the profile of partition B, centered  
 866 on strips 52 and 59. Section ?? will help us understand that these two peaks are due respectively to  
 867 forward and backward coming cosmic particles where forward coming particles are first detected by  
 868 the scintillators and then the RPC while the backward coming muons are first detected in the RPC.



*Figure 4.11: Hit distributions over all 3 partitions of RE-4-2-BARC-161 chamber is showed on these plots. Top, middle and bottom figures respectively correspond to partitions A, B, and C. These plots show that some events still occur in other half-partitions than B2, which corresponds to strips 49 to 64, in front of which the trigger is placed, contributing to the inefficiency of detection of cosmic muons. In the case of partitions A and C, the very low amount of data can be interpreted as noise. On the other hand, it is clear that a little portion of muons reach the half-partition B1, corresponding to strips 33 to 48.*

### 869 4.3.2 Data Acquisition

### 870 4.3.3 Geometrical acceptance of the setup layout to cosmic muons

871 In order to profit from a constant gamma irradiation, the detectors inside of the GIF bunker need  
 872 to be placed in a plane orthogonal to the beam line. The muon beam that used to be available was  
 873 meant to test the performance of detectors under test. This beam not being active anymore, another  
 874 solution to test detector performance had to be used. Thus, it has been decided to use cosmic muons  
 875 detected through a telescope composed of two scintillators. Lead blocks were used as shielding to

876 protect the photomultipliers from gammas as can be seen from Figure 4.10.

877 An inclination has been given to the cosmic telescope to maximize the muon flux. A good com-  
 878 promise had to be found between good enough muon flux and narrow enough hit distribution to  
 879 be sure to contain all the events into only one half partitions as required from the limited available  
 880 readout hardware. Nevertheless, a consequence of the misplaced trigger, that can be seen as a loss  
 881 of events in half-partition B1 in Figure 4.11, is an inefficiency. Nevertheless, the inefficiency of ap-  
 882 proximately 20 % highlighted in Figure 4.12 by comparing the performance of chamber BARC-161  
 883 in 904 and at GIF without irradiation seems too important to be explained only by the geometri-  
 884 cal acceptance of the setup itself. Simulations have been conducted to show how the setup brings  
 885 inefficiency.

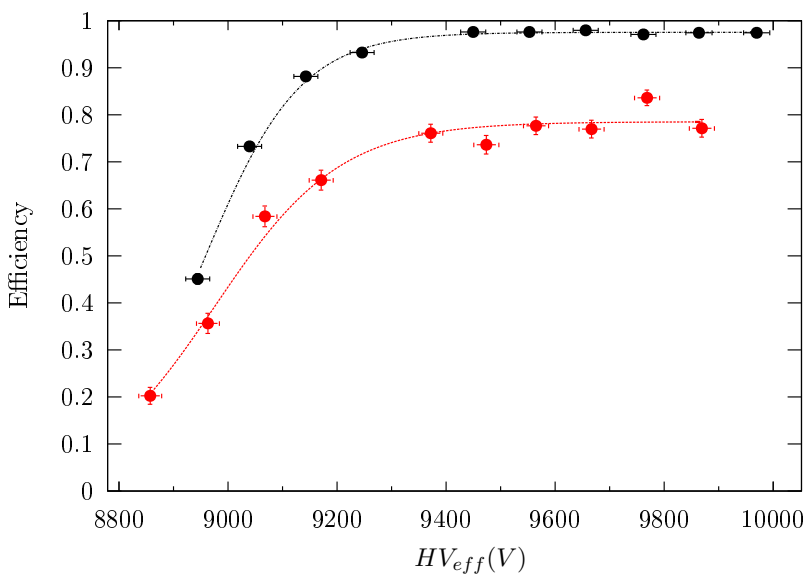
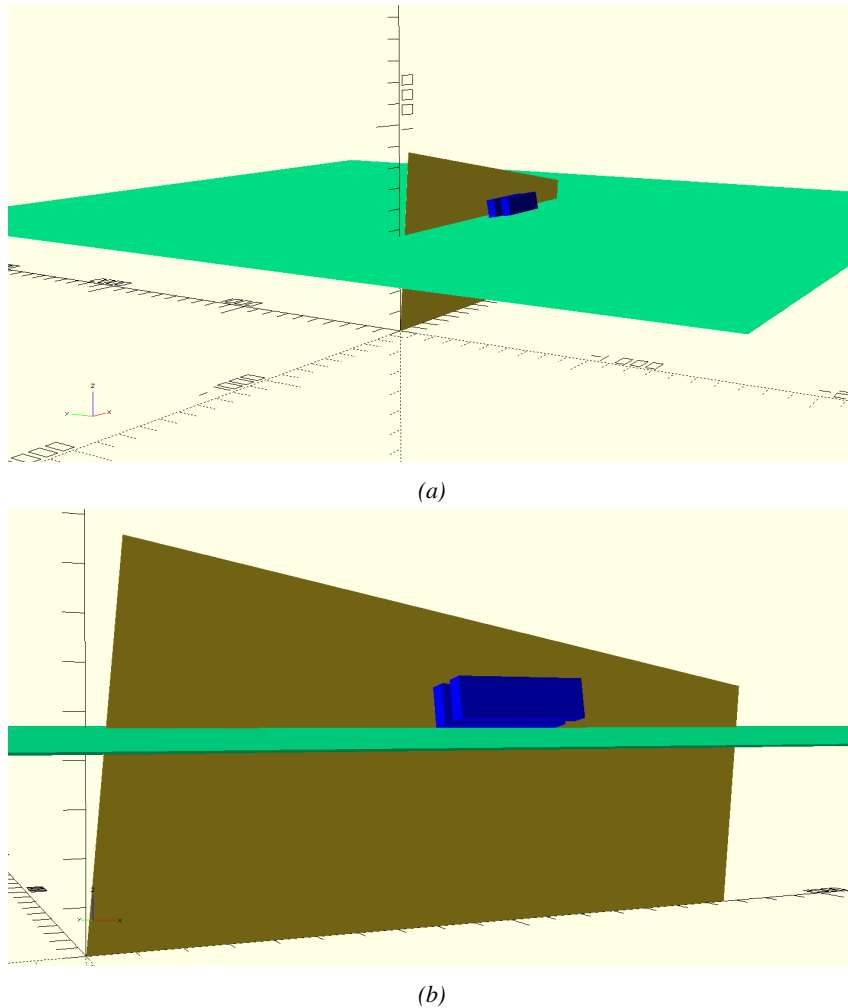


Figure 4.12: Results are derived from data taken on half-partition B2 only. On the 18<sup>th</sup> of June 2014, data has been taken on chamber RE-2-BARC-161 at building 904 (Prevessin Site) with cosmic muons providing us a reference efficiency plateau of  $(97.54 \pm 0.15)\%$  represented by a black curve. A similar measurement has been done at GIF on the 21<sup>st</sup> of July with the same chamber giving a plateau of  $(78.52 \pm 0.94)\%$  represented by a red curve.

#### 886 4.3.3.1 Description of the simulation layout

887 The layout of GIF setup has been reproduced and incorporated into a Monte Carlo (MC) simulation  
 888 to study the influence of the disposition of the telescope on the final distribution measured by the  
 889 RPC. A 3D view of the simulated layout is given into Figure 4.13. Muons are generated randomly  
 890 in a horizontal plane located at a height corresponding to the lowest point of the PMTs. This way,  
 891 the needed size of the plane in order to simulate events happening at very big azimuthal angles (i.e.  
 892  $\theta \approx \pi$ ) can be kept relatively small. The muon flux is designed to follow the usual  $\cos^2\theta$  distribution  
 893 for cosmic particle. The goal of the simulation is to look at muons that pass through the muon  
 894 telescope composed of the two scintillators and define their distribution onto the RPC plane. During  
 895 the reconstruction, the RPC plane is then divided into its strips and each muon track is assigned to a  
 896 strip.



*Figure 4.13: Representation of the layout used for the simulations of the test setup. The RPC is represented as a yellow trapezoid while the two scintillators as blue cuboids looking at the sky. A green plane corresponds to the muon generation plane within the simulation. Figure 4.9a shows a global view of the simulated setup. Figure 4.9b shows a zoomed view that allows to see the 2 scintillators as well as the full RPC plane.*

897 In order to further refine the quality of the simulation and understand deeper the results the  
 898 dependance of the distribution has been studied for a range of telescope inclinations. Moreover,  
 899 the threshold applied on the PMT signals has been included into the simulation in the form of a  
 900 cut. In the approximation of uniform scintillators, it has been considered that the threshold can be  
 901 understood as the minimum distance particles need to travel through the scintillating material to give  
 902 a strong enough signal. Particles that travel a distance smaller than the set "threshold" are thus not  
 903 detected by the telescope and cannot trigger the data taking. Finally, the FEE threshold also has  
 904 been considered in a similar way. The mean momentum of horizontal cosmic rays is higher than  
 905 those of vertical ones but the stopping power of matter for momenta ranging from 1 GeV to 1 TeV  
 906 stays comparable. It is then possible to assume that the mean number of primary  $e^-/ion$  pairs per  
 907 unit length will stay similar and thus, depending on the applied discriminator threshold, muons with

908 the shortest path through the gas volume will deposit less charge and induce a smaller signal on the  
 909 pick-up strips that could eventually not be detected. These two thresholds also restrain the overall  
 910 geometrical acceptance of the system.

911 **4.3.3.2 Simulation procedure**

912 The simulation software has been designed using C++ and the output data is saved into ROOT  
 913 histograms. Simulations start for a threshold  $T_{scint}$  varying in a range from 0 to 45 mm in steps  
 914 of 5 mm, where  $T_{scint} = 0$  mm corresponds to the case where there isn't any threshold apply on  
 915 the input signal while  $T_{scint} = 45$  mm, which is the scintillator thickness, is the case where muons  
 916 cannot arrive orthogonally onto the scintillator surface. For a given  $T_{scint}$ , a set of RPC thresholds  
 917 are considered. The RPC threshold,  $T_{RPC}$  varies from 2 mm, the thickness of the gas volume, to  
 918 3 mm in steps of 0.25 mm. For each  $(T_{scint}; T_{RPC})$  pair,  $N_\mu = 10^8$  muons are randomly generated  
 919 inside the muon plane described in the previous paragraph with an azimuthal angle  $\theta$  chosen to follow  
 920 a  $\cos^2\theta$  distribution.

921 Planes are associated to each surface of the scintillators. Knowing muon position into the muon  
 922 plane and its direction allows us, by assuming that muons travel in a straight line, to compute the  
 923 intersection of the muon track with these planes. Applying conditions to the limits of the surfaces  
 924 of the scintillator faces then gives us an answer to whether or not the muon passed through the  
 925 scintillators. In the case the muon has indeed passed through the telescope, the path through each  
 926 scintillator is computed and muons whose path was shorter than  $T_{scint}$  are rejected and are thus  
 927 considered as having not interacted with the setup.

928 On the contrary, if the muon is labeled as good, its position within the RPC plane is computed  
 929 and the corresponding strip, determined by geometrical tests in the case the distance through the  
 930 gas volume was enough not to be rejected because of  $T_{RPC}$ , gets a hit and several histograms  
 931 are filled in order to keep track of the generation point on the muon plane, the intersection points  
 932 of the reconstructed muons within the telescope, or on the RPC plane, the path traveled through  
 933 each individual scintillator or the gas volume, as well as other histograms. Moreover, muons fill  
 934 different histograms whether they are forward or backward coming muons. They are discriminated  
 935 according to their direction components. When a muon is generated, an  $(x, y, z)$  position is assigned  
 936 into the muon plane as well as a  $(\theta; \phi)$  pair that gives us the direction it's coming from. This way,  
 937 muons satisfying the condition  $0 \leq \phi < \pi$  are designated as backward coming muons while muons  
 938 satisfying  $\pi \leq \phi < 2\pi$  as forward coming muons.

939 This simulation is then repeated for different telescope inclinations ranging in between 4 and 20°  
 940 and varying in steps of 2°. Due to this inclination and to the vertical position of the detector under  
 941 test, the muon distribution reconstructed in the detector plane is asymmetrical. The choice has been  
 942 made to choose a skew distribution formula to fit the data built as the multiplication of gaussian and  
 943 sigmoidal curves together. A typical gaussian formula is given as 4.1 and has three free parameters  
 944 as  $A_g$ , its amplitude,  $\bar{x}$ , its mean value and  $\sigma$ , its root mean square. Sigmoidal curves as given by  
 945 formula 4.2 are functions converging to 0 and  $A_s$  as  $x$  diverges. The inflection point is given as  $x_i$   
 946 and  $\lambda$  is proportional to the slope at  $x = x_i$ . In the limit where  $\lambda \rightarrow \infty$ , the sigmoid becomes a  
 947 step function.

$$g(x) = A_g e^{-\frac{(x-\bar{x})^2}{2\sigma^2}} \quad (4.1)$$

$$s(x) = \frac{A_s}{1 + e^{-\lambda(x-x_i)}} \quad (4.2)$$

Finally, a possible representation of a skew distribution is given by formula 4.3 and is the product of 4.1 and 4.2. Naturally, here  $A_{sk} = A_g \times A_s$  and represents the theoretical maximum in the limit where the skew tends to a gaussian function.

$$sk(x) = g(x) \times s(x) = A_{sk} \frac{e^{\frac{-(x-\bar{x})^2}{2\sigma^2}}}{1 + e^{-\lambda(x-x_i)}} \quad (4.3)$$

### 4.3.3.3 Results

#### Influence of $T_{scint}$ on the muon distribution

#### Influence of $T_{RPC}$ on the muon distribution

#### Influence of the telescope inclination on the muon distribution

#### Comparison to data taken at GIF without irradiation

### 4.3.4 Photon flux at GIF

#### 4.3.4.1 Expectations from simulations

In order to understand and evaluate the  $\gamma$  flux in the GIF area, simulations had been conducted in 1999 and published by S. Agosteo et al [54]. Table 4.1 presented in this article gives us the  $\gamma$  flux for different distances  $D$  to the source. This simulation was done using GEANT and a Monte Carlo N-Particle (MCNP) transport code, and the flux  $F$  is given in number of  $\gamma$  per unit area and unit time along with the estimated error from these packages expressed in %.

Nominal ABS	Photon flux $F$ [ $s^{-1}cm^{-2}$ ]			
	at $D = 50$ cm	at $D = 155$ cm	at $D = 300$ cm	at $D = 400$ cm
1	$0.12 \cdot 10^8 \pm 0.2\%$	$0.14 \cdot 10^7 \pm 0.5\%$	$0.45 \cdot 10^6 \pm 0.5\%$	$0.28 \cdot 10^6 \pm 0.5\%$
2	$0.68 \cdot 10^7 \pm 0.3\%$	$0.80 \cdot 10^6 \pm 0.8\%$	$0.25 \cdot 10^6 \pm 0.8\%$	$0.16 \cdot 10^6 \pm 0.6\%$
5	$0.31 \cdot 10^7 \pm 0.4\%$	$0.36 \cdot 10^6 \pm 1.2\%$	$0.11 \cdot 10^6 \pm 1.2\%$	$0.70 \cdot 10^5 \pm 0.9\%$

Table 4.1: Total photon flux ( $E\gamma \leq 662$  keV) with statistical error predicted considering a  $^{137}Cs$  activity of 740 GBq at different values of the distance  $D$  to the source along the  $x$ -axis of irradiation field [54].

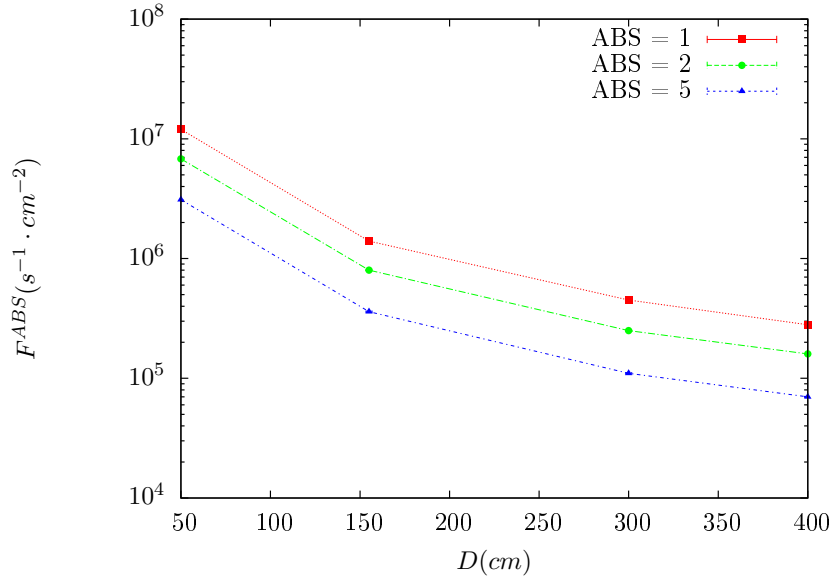


Figure 4.14:  $\gamma$  flux  $F(D)$  is plot using values from table 4.1. As expected, the plot shows similar attenuation behaviours with increasing distance for each absorption factors.

The simulation doesn't directly provides us with an estimated flux at the level of our RPC. First of all, it is needed to extract the value of the flux from the available data contained in the original paper and then to estimate the flux in 2014 at the time the experimentation took place. Figure 4.14 that contains the data from Table 4.1. In the case of a pointlike source emitting isotropic and homogeneous gamma radiations, the gamma flux  $F$  at a distance  $D$  to the source with respect to a reference point situated at  $D_0$  where a known flux  $F_0$  is measured will be expressed like in Equation 4.4, assuming that the flux decreases as  $1/D^2$ , where  $c$  is a fitting factor.

$$F^{ABS} = F_0^{ABS} \times \left( \frac{cD_0}{D} \right)^2 \quad (4.4)$$

By rewriting Equation 4.4, it comes that :

$$c = \frac{D}{D_0} \sqrt{\frac{F^{ABS}}{F_0^{ABS}}} \quad (4.5)$$

$$\Delta c = \frac{c}{2} \left( \frac{\Delta F^{ABS}}{F^{ABS}} + \frac{\Delta F_0^{ABS}}{F_0^{ABS}} \right) \quad (4.6)$$

Finally, using Equation 4.5 and the data in Table 4.1 with  $D_0 = 50$  cm as reference point, we can build Table 4.2. It is interesting to note that  $c$  for each value of  $D$  doesn't depend on the absorption factor.

Nominal ABS	Correction factor $c$		
	at $D = 155$ cm	at $D = 300$ cm	at $D = 400$ cm
1	$1.059 \pm 0.70\%$	$1.162 \pm 0.70\%$	$1.222 \pm 0.70\%$
2	$1.063 \pm 1.10\%$	$1.150 \pm 1.10\%$	$1.227 \pm 0.90\%$
5	$1.056 \pm 1.60\%$	$1.130 \pm 1.60\%$	$1.202 \pm 1.30\%$

Table 4.2: Correction factor  $c$  is computed thanks to formulae 4.5 taking as reference  $D_0 = 50$  cm and the associated flux  $F_0^{ABS}$  for each absorption factor available in table 4.1.

974 For the range of  $D/D_0$  values available, it is possible to use a simple linear fit to get the evolution  
 975 of  $c$ . The linear fit will then use only 2 free parameters,  $a$  and  $b$ , as written in Equation 4.7. This gives  
 976 us the results showed in Figure 4.15. Figure 4.15b confirms that using only a linear fit to extract  $c$  is  
 977 enough as the evolution of the rate that can be obtained superimposes well on the simulation points.

$$c \left( \frac{D}{D_0} \right) = a \frac{D}{D_0} + b \quad (4.7)$$

$$F^{ABS} = F_0^{ABS} \left( a + \frac{bD_0}{D} \right)^2 \quad (4.8)$$

$$\Delta F^{ABS} = F^{ABS} \left[ \frac{\Delta F_0^{ABS}}{F_0^{ABS}} + 2 \frac{\Delta a + \Delta b \frac{D_0}{D}}{a + \frac{bD_0}{D}} \right] \quad (4.9)$$

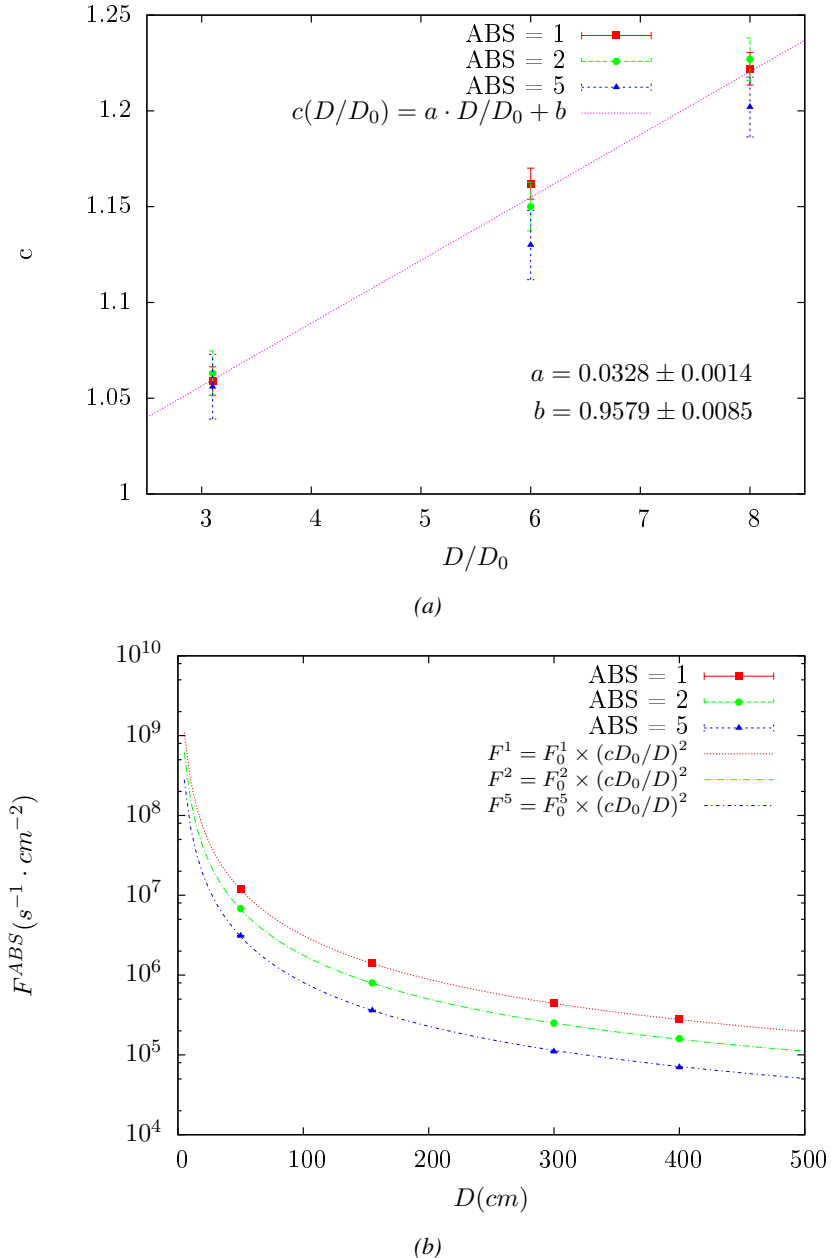


Figure 4.15: Figure 4.15a shows the linear approximation fit done via formulae 4.7 on data from table 4.2. Figure 4.15b shows a comparison of this model with the simulated flux using  $a$  and  $b$  given in figure 4.15a in formulae 4.4 and the reference value  $D_0 = 50\text{cm}$  and the associated flux for each absorption factor  $F_0^{ABS}$  from table 4.1

In the case of the 2014 GIF tests, the RPC plane is located at a distance  $D = 206\text{ cm}$  to the source. Moreover, to estimate the strength of the flux in 2014, it is necessary to consider the nuclear decay through time associated to the Cesium source whose half-life is well known ( $t_{1/2} = (30.05 \pm 0.08)\text{ y}$ ). The very first source activity measurement has been done on the 5<sup>th</sup> of March 1997 while the Gif

982 tests were done in between the 20<sup>th</sup> and the 31<sup>st</sup> of August 2014, i.e. at a time  $t = (17.47 \pm 0.02)$  y  
 983 resulting in an attenuation of the activity from 740 GBq in 1997 to 494 GBq in 2014. All the needed  
 984 information to extrapolate the flux through our detector in 2014 has now been assembled, leading  
 985 to the Table 4.3. It is interesting to note that for a common RPC sensitivity to  $\gamma$  of  $2 \cdot 10^{-3}$ , the  
 986 order of magnitude of the estimated hit rate per unit area is of the order of the kHz for the fully  
 987 opened source. Moreover, taking profit of the two working absorbers, it will be possible to scan  
 988 background rates at 0 Hz,  $\sim 300$  Hz as well as  $\sim 600$  Hz. Without source, a good estimate of the  
 989 intrinsic performance will be available. Then at 300 Hz, the goal will be to show that the detectors  
 990 fulfill the performance certification of CMS RPCs. Then a first idea of the performance of the  
 991 detectors at higher background will be provided with absorption factors 2 ( $\sim 600$  Hz) and 1 (no  
 992 absorption). *[Here I will also put a reference to the plot showing the estimated background rate at  
 993 the level of RE3/1 in the case of HL-LHC but this one being in another chapter, I will do it later.]*

Nominal ABS	Photon flux $F$ [ $s^{-1}cm^{-2}$ ]			Hit rate/unit area [ $Hz cm^{-2}$ ] at $D^{2014} = 206$ cm
	at $D_0^{1997} = 50$ cm	at $D^{1997} = 206$ cm	at $D^{2014} = 206$ cm	
1	$0.12 \cdot 10^8 \pm 0.2\%$	$0.84 \cdot 10^6 \pm 0.3\%$	$0.56 \cdot 10^6 \pm 0.3\%$	$1129 \pm 32$
2	$0.68 \cdot 10^7 \pm 0.3\%$	$0.48 \cdot 10^6 \pm 0.3\%$	$0.32 \cdot 10^6 \pm 0.3\%$	$640 \pm 19$
5	$0.31 \cdot 10^7 \pm 0.4\%$	$0.22 \cdot 10^6 \pm 0.3\%$	$0.15 \cdot 10^6 \pm 0.3\%$	$292 \pm 9$

Table 4.3: The data at  $D_0$  in 1997 is taken from [54]. In a second step, using Equations 4.8 and 4.9, the flux at  $D$  can be estimated in 1997. Then, taking into account the attenuation of the source activity, the flux at  $D$  can be estimated at the time of the tests in GIF in 2014. Finally, assuming a sensitivity of the RPC to  $\gamma$   $s = 2 \cdot 10^{-3}$ , an estimation of the hit rate per unit area is obtained.

994    **4.3.4.2 Dose measurements**

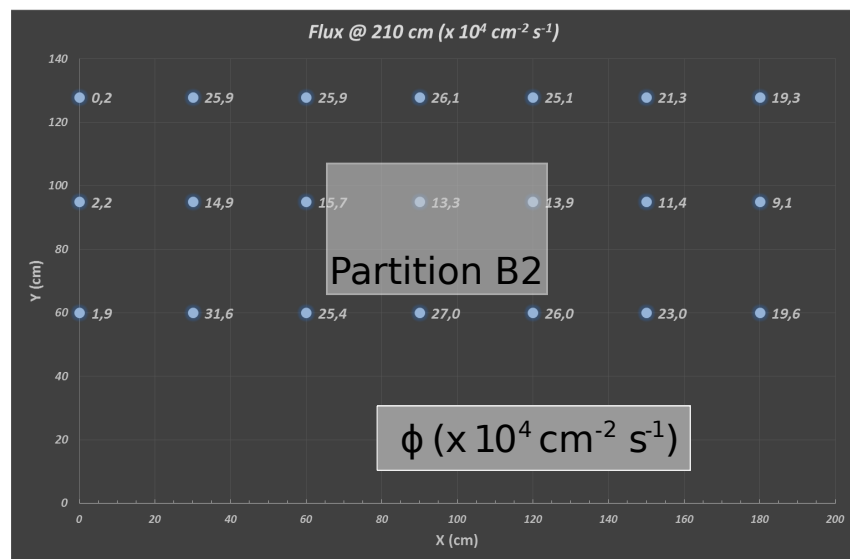


Figure 4.16: Dose measurements has been done in a plane corresponding to the tents front side. This plan is 1900 mm away from the source. As explained in the first chapter, a lens-shaped lead filter provides a uniform photon flux in the vertical plan orthogonal to the beam direction. If the second line of measured fluxes is not taken into account because of lower values due to experimental equipments in the way between the source and the tent, the uniformity of the flux is well showed by the results.

<sup>995</sup> **4.3.5 Results and discussions**

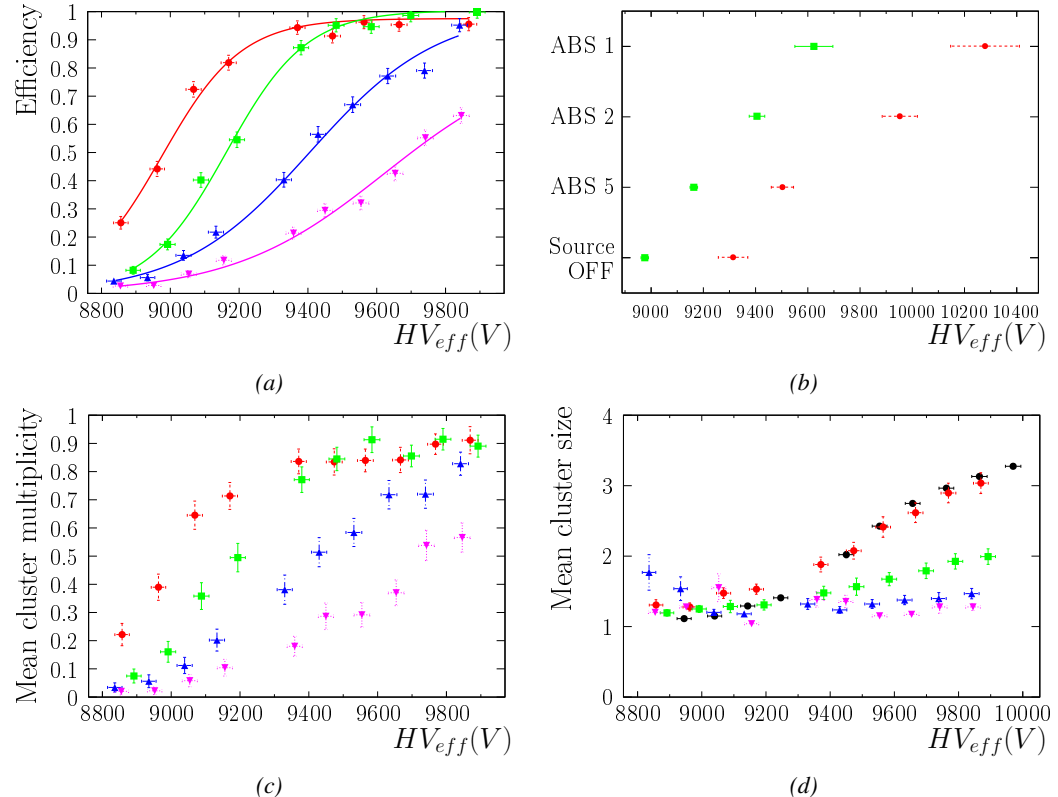


Figure 4.17

## 996 4.4 Longevity tests at GIF++

997 Longevity studies imply a monitoring of the performance of the detectors probed using a high inten-  
998 sity muon beam in a irradiated environment by periodically measuring their rate capability, the dark  
999 current running through them and the bulk resistivity of the Bakelite composing their electrodes.  
1000 GIF++, with its very intense  $^{137}\text{Cs}$  source, provides the perfect environment to perform such kind  
1001 of tests. Assuming a maximum acceleration factor of 3, it is expected to accumulate the equivalent  
1002 charge in 1.7 years.

1003 As the maximum background is found in the endcap, the choice naturally was made to focus the  
1004 GIF++ longevity studies on endcap chambers. Most of the RPC system was installed in 2007. Nev-  
1005 ertheless, the large chambers in the fourth endcap (RE4/2 and RE4/3) have been installed during  
1006 LS1 in 2014. The Bakelite of these two different productions having different properties, four spare  
1007 chambers of the present system were selected, two RE2,3/2 spares and two RE4/2 spares. Having  
1008 two chambers of each type allows to always keep one of them non irradiated as reference, the per-  
1009 formance evolution of the irradiated chamber being then compared through time to the performance  
1010 of the non irradiated one.

1011 The performance of the detectors under different level of irradiation is measured periodically dur-  
1012 ing dedicated test beam periods using the H4 muon beam. In between these test beam periods, the  
1013 two RE2,3/2 and RE4/2 chambers selected for this study are irradiated by the  $^{137}\text{Cs}$  source in order  
1014 to accumulate charge and the gamma background is monitored, as well as the currents. The two  
1015 remaining chambers are kept non-irradiated as reference detectors. Due to the limited gas flow in  
1016 GIF++, the RE4 chamber remained non-irradiated until end of November 2016 where a new mass  
1017 flow controller has been installed allowing for bigger volumes of gas to flow in the system.

1018 Figures 4.18 and 4.19 give us for different test beam periods, and thus for increasing integrated  
1019 charge through time, a comparison of the maximum efficiency, obtained using a sigmoid-like func-  
1020 tion, and of the working point of both irradiated and non irradiated chambers [**SIGMOID2005**]. No  
1021 aging is yet to see from this data, the shifts in  $\gamma$  rate per unit area in between irradiated and non  
1022 irradiated detectors and RE2 and RE4 types being easily explained by a difference of sensitivity due  
1023 to the various Bakelite resistivities of the HPL electrodes used for the electrode production.

1024 Collecting performance data at each test beam period allows us to extrapolate the maximum effi-  
1025 ciency for a background hit rate of  $300\text{ Hz}/\text{cm}^2$  corresponding to the expected HL-LHC conditions.  
1026 Aging effects could emerge from a loss of efficiency with increasing integrated charge over time,  
1027 thus Figure 4.20 helps us understand such degradation of the performance of irradiated detectors in  
1028 comparison with non irradiated ones. The final answer for an eventual loss of efficiency is given in  
1029 Figure 4.21 by comparing for both irradiated and non irradiated detectors the efficiency sigmoids  
1030 before and after the longevity study. Moreover, to complete the performance information, the Bake-  
1031 lite resistivity is regularly measured thanks to  $Ag$  scans (Figure 4.22) and the noise rate is monitored  
1032 weekly during irradiation periods (Figure 4.23). At the end of 2016, no signs of aging were observed  
1033 and further investigation is needed to get closer to the final integrated charge requirements proposed  
1034 for the longevity study of the present CMS RPC sub-system.

1035

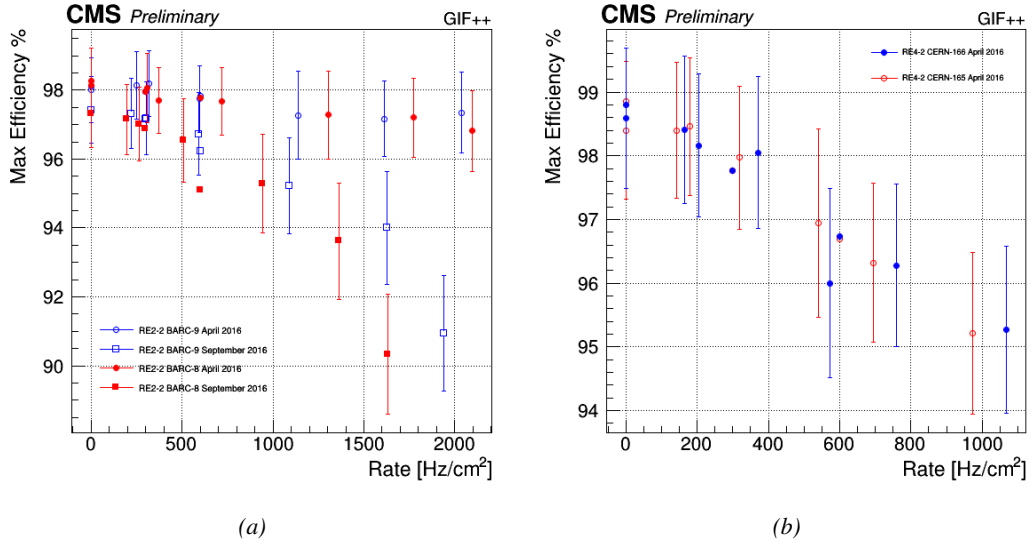


Figure 4.18: Evolution of the maximum efficiency for RE2 (4.18a) and RE4 (4.18b) chambers with increasing extrapolated  $\gamma$  rate per unit area at working point. Both irradiated (blue) and non irradiated (red) chambers are shown.

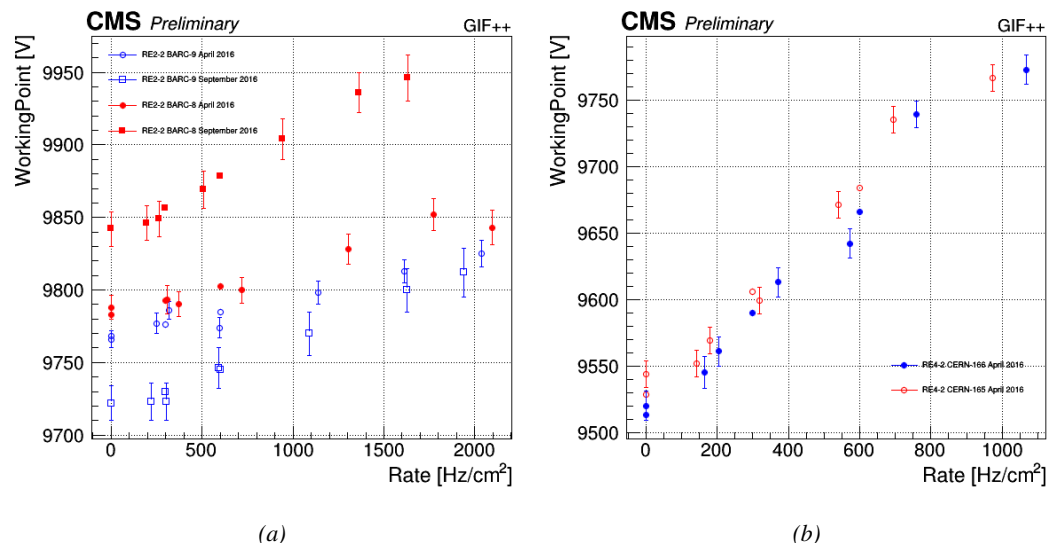
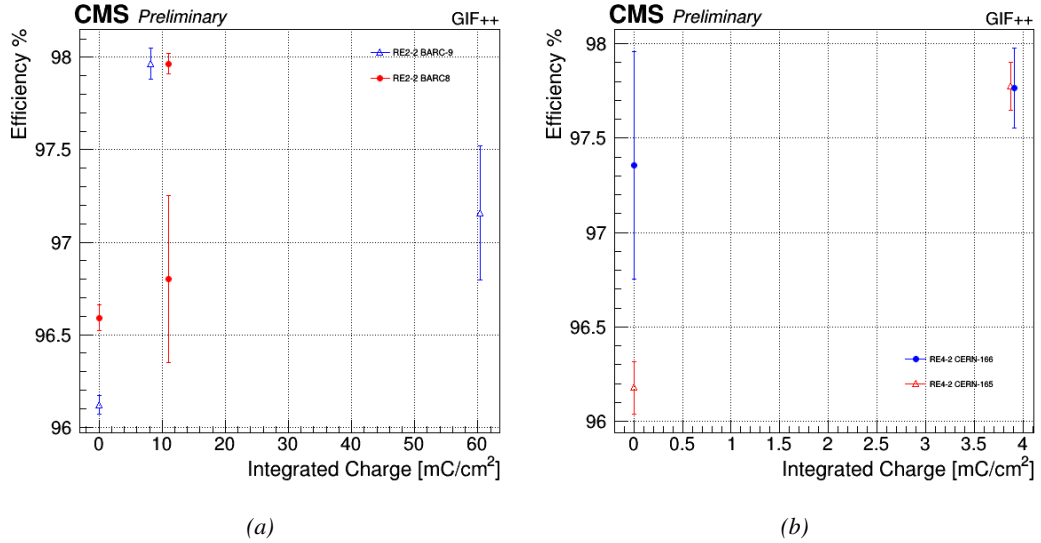
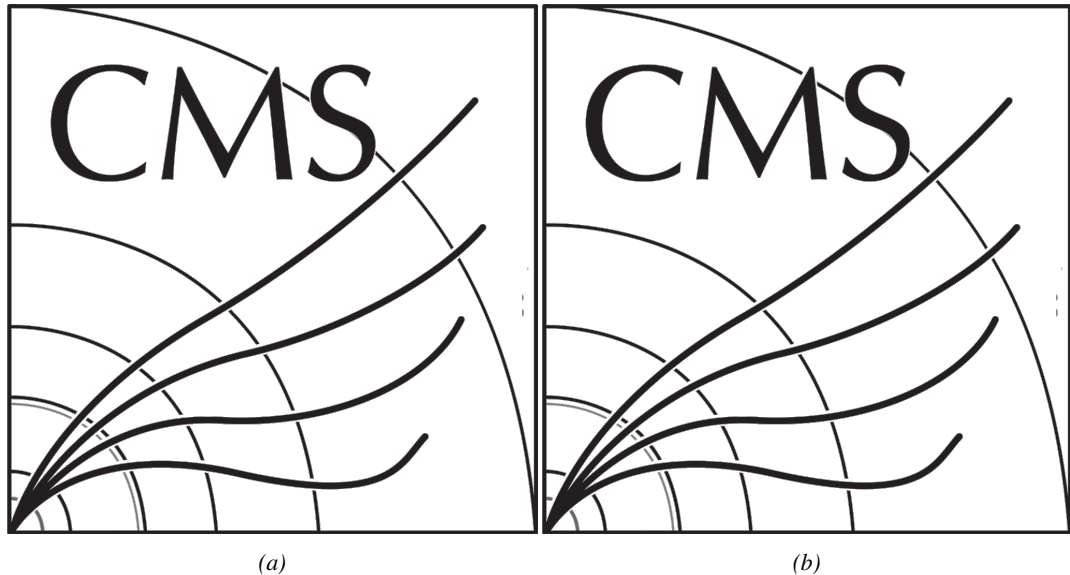


Figure 4.19: Evolution of the working point for RE2 (4.19a) and RE4 (4.19b) with increasing extrapolated  $\gamma$  rate per unit area at working point. Both irradiated (blue) and non irradiated (red) chambers are shown.



*Figure 4.20: Evolution of the maximum efficiency at HL-LHC conditions, i.e. a background hit rate per unit area of 300 Hz/cm<sup>2</sup>, with increasing integrated charge for RE2 (4.20a) and RE4 (4.20b) detectors. Both irradiated (blue) and non irradiated (red) chambers are shown. The integrated charge for non irradiated detectors is recorded during test beam periods and stays small with respect to the charge accumulated in irradiated chambers.*



*Figure 4.21: Comparison of the efficiency sigmoid before (triangles) and after (circles) irradiation for RE2 (4.21a) and RE4 (4.21b) detectors. Both irradiated (blue) and non irradiated (red) chambers are shown.*

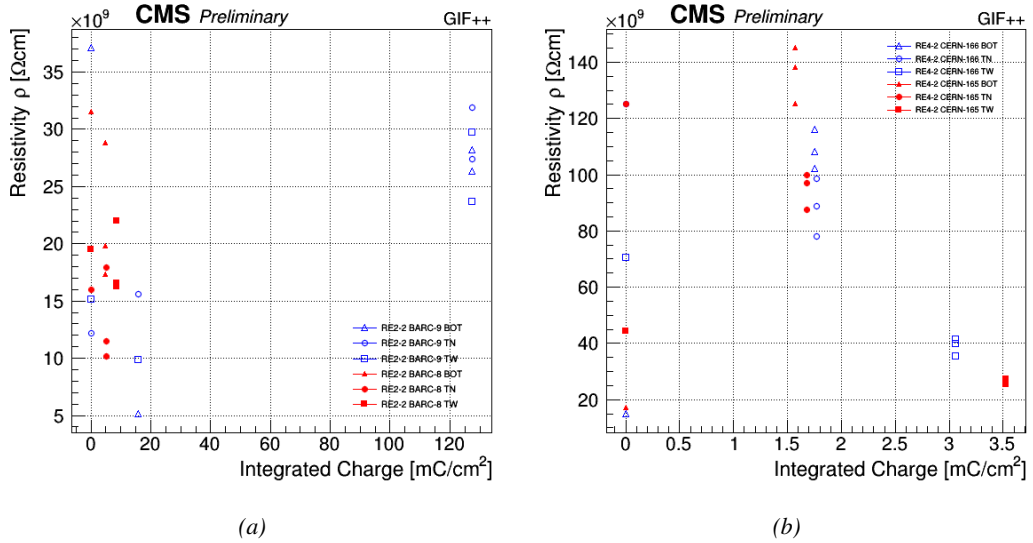


Figure 4.22: Evolution of the Bakelite resistivity for RE2 (4.22a) and RE4 (4.22b) detectors. Both irradiated (blue) and non-irradiated (red) chambers are shown.

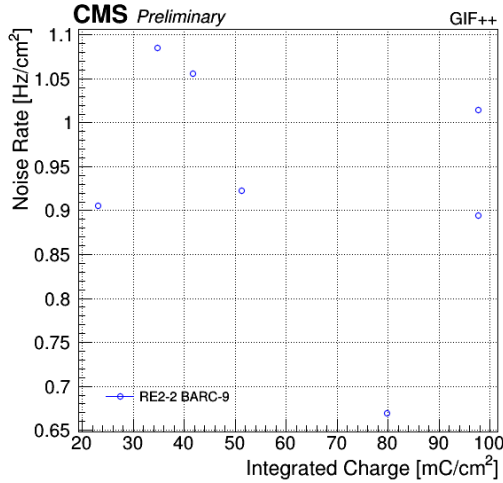


Figure 4.23: Evolution of the noise rate per unit area for the irradiated chamber RE2-2-BARC-9 only.

#### 4.4.1 Description of the Data Acquisition

For the longevity studies, four spare chambers of the present system are used. Two spare RPCs of the RE2,3 stations as well as two spare RPCs from the new RE4 stations have been mounted in a Trolley. Six RE4 gaps are also placed in the trolley. The trolley is placed inside the GIFT++ in the upstream region of the bunker, taking the cesium source as a reference. The trolley is oriented for the detection surface of the chambers to be orthogonal to the beam line. The system can be moved along the orthogonal plane in order to have the beam in all  $\eta$ -partitions. For the aging the trolley is

1043 moved outside the beam line and is placed in a distance of 5.2 m to the source, which irradiates the  
 1044 bunker using an attenuation filter of 2.2 which corresponds to a fluence of  $10^7 \text{ gamma/cm}^2$ .

1045 During GIF++ operation, the data collected can be divided into different categories as several  
 1046 parameters are monitored in addition to the usual RPC performance data. On one hand, to know  
 1047 the performance of a chamber, it is need to measure its efficiency and to know the background  
 1048 conditions in which it is operated. To do this, the hit signals from the chamber are recorded and  
 1049 stored in a ROOT file via a Data Acquisition (DAQ) software. On the other hand, it is also very  
 1050 important to monitor parameters such as environmental pressure and temperature, gas temperature  
 1051 and humidity, RPC HV, LV, and currents, or even source and beam status. This is done through the  
 1052 GIF++ web Detector Control Software (DCS) that stores this information in a database.

1053 Two different types of tests are conducted on RPCs via the DAQ. Indeed, the performance of the  
 1054 detectors is measured periodically during dedicated test beam periods using the H4 muon beam. In  
 1055 between these test beam periods, when the beam is not available, the chambers are irradiated by the  
 1056  $^{137}\text{Cs}$  in order to accumulate deposited charge and the gamma background is measured.

1057 RPCs under test are connected through LVDS cables to V1190A Time-to-Digital Converter  
 1058 (TDC) modules manufactured by CAEN. These modules, located in the rack area outside of the  
 1059 bunker, get the logic signals sent by the chambers and save them into their buffers. Due to the  
 1060 limited size of the buffers, the collected data is regularly erased and replaced. A trigger signal is  
 1061 needed for the TDC modules to send the useful data to the DAQ computer via a V1718 CAEN USB  
 1062 communication module.

1063 In the case of performance test, the trigger signal used for data acquisition is generated by the  
 1064 coincidence of three scintillators. A first one is placed upstream outside of the bunker, a second one  
 1065 is placed downstream outside of the bunker, while a third one is placed in front of the trolley, close by  
 1066 the chambers. Every time a trigger is sent to the TDCs, i.e. every time a muon is detected, knowing  
 1067 the time delay in between the trigger and the RPC signals, signals located in the right time window  
 1068 are extracted from the buffers and saved for later analysis. Signals are taken in a time window of  
 1069 400 ns centered on the muon peak (here we could show a time spectrum). On the other hand, in the  
 1070 case of background rate measurement, the trigger signal needs to be "random" not to measure muons  
 1071 but to look at gamma background. A trigger pulse is continuously generated at a rate of 300 Hz using  
 1072 a dual timer. To integrate an as great as possible time, all signals contained within a time window of  
 1073 10us prior to the random trigger signal are extracted form the buffers and saved for further analysis  
 1074 (here another time spectrum to illustrate could be useful, maybe even place both spectrum together  
 1075 as a single Figure).

1076 The signals sent to the TDCs correspond to hit collections in the RPCs. When a particle hits  
 1077 a RPC, it induce a signal in the pickup strips of the RPC readout. If this signal is higher than the  
 1078 detection threshold, a LVDS signal is sent to the TDCs. The data is then organised into 4 branches  
 1079 keeping track of the event number, the hit multiplicity for the whole setup, and the time and channel  
 1080 profile of the hits in the TDCs.

#### 1081 **4.4.2 RPC current, environmental and operation parameter monitoring**

1082 In order to take into account the variation of pressure and temperature between different data taking  
 1083 periods the applied voltage is corrected following the relationship :

$$1084 HV_{eff} = HV_{app} \times \left( 0.2 + 0.8 \cdot \frac{P_0}{P} \times \frac{T}{T_0} \right) \quad (4.10)$$

1084 where  $T_0$  (=293 K) and  $P_0$  (=990 mbar) are the reference values.

1085 **4.4.3 Measurement procedure**

1086 Insert a short description of the online tools (DAQ, DCS, DQM).

1087 Insert a short description of the offline tools : tracking and efficiency algorithm.

1088 Identify long term aging effects we are monitoring the rates per strip.

1089 **4.4.4 Longevity studies results**

# 5

1090

1091

## Investigation on high rate RPCs

1092 **5.1 Rate limitations and ageing of RPCs**

1093 **5.1.1 Low resistivity electrodes**

1094 **5.1.2 Low noise front-end electronics**

1095 **5.2 Construction of prototypes**

1096 **5.3 Results and discussions**



# 6

1097

1098

## Conclusions and outlooks

<sup>1099</sup> **6.1 Conclusions**

<sup>1100</sup> **6.2 Outlooks**



# A

1101

1102

1103

## A data acquisition software for CAEN VME TDCs

1104 Certifying detectors in the perspective of HL-LHC required to develop tools for the GIF++ experiment.  
1105 Among them was the C++ Data Acquisition (DAQ) software that allows to make the communications  
1106 in between a computer and TDC modules in order to retrieve the RPC data [56]. In this  
1107 appendix, details about this software, as of how the software was written, how it functions and how  
1108 it can be exported to another similar setup, will be given.

### 1109 A.1 GIF++ DAQ file tree

1110 GIF++ DAQ source code is fully available on github at [https://github.com/afagot/GIF\\_DAQ](https://github.com/afagot/GIF_DAQ). The software requires 3 non-optional dependencies:

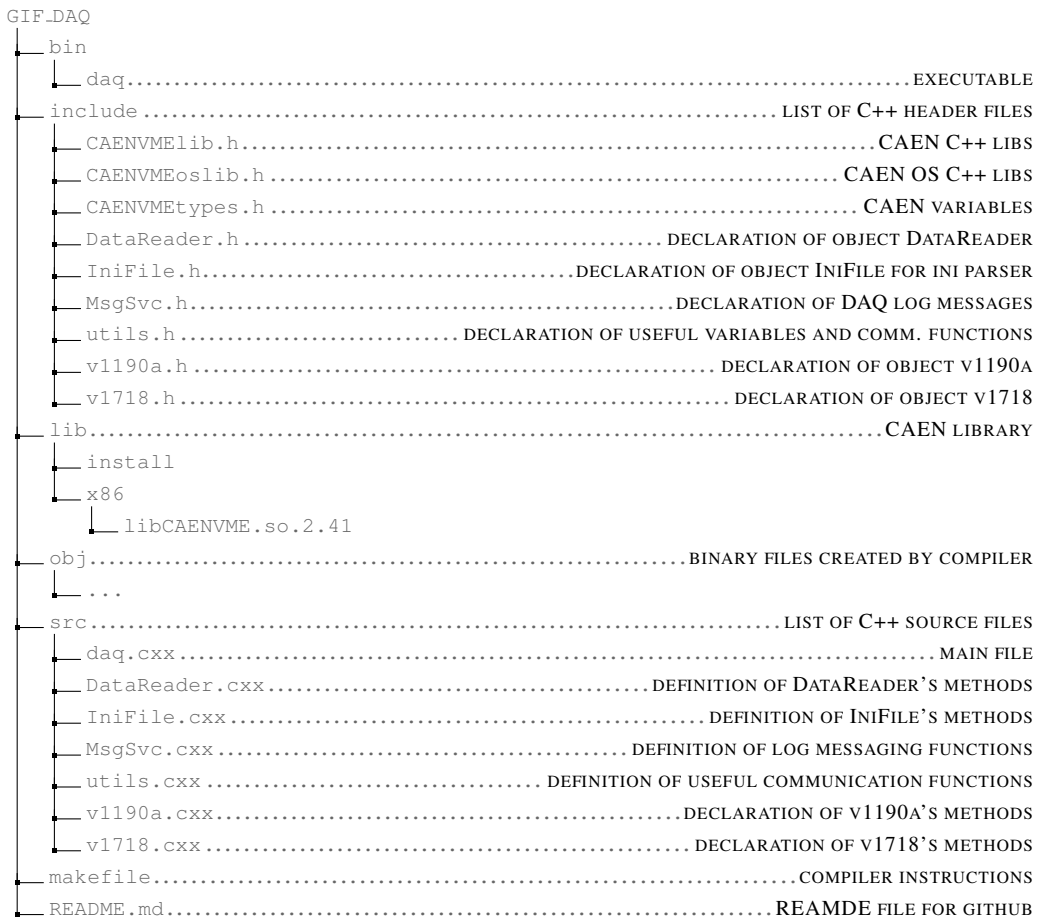
- 1112 • CAEN USB Driver, to mount the VME hardware,
- 1113 • CAEN VME Library, to communicate with the VME hardware, and
- 1114 • ROOT, to organize the collected data into a TTree.

1115 The CAEN VME library will not be packaged by distributions and will need to be installed man-  
1116 ually. To compile the GIF++ DAQ project via a terminal, from the DAQ folder use the command:

1117  
1118 `make`

1119 The source code tree is provided below along with comments to give an overview of the files' con-  
1120 tent. The different objects created for this project (`v1718`, `v1190a`, `IniFile` & `DataReader`) will be  
1121 described in details in the following sections.

1122



## 1123 A.2 Usage of the DAQ

1124 GIF++ DAQ, as used in GIF++, is not a standalone software. Indeed, the system being more complexe,  
 1125 the DAQ only is a sub-layer of the software architecture developped to control and monitor  
 1126 the RPCs that are placed into the bunker for performance study in an irradiated environment. The top  
 1127 layer of GIF++ is a Web Detector Control System (webDCS) application. The DAQ is only called  
 1128 by the webDCS when data needs to be acquired. The webDCS operates the DAQ through command  
 1129 line. To start the DAQ, the webDCS calls:

1130

1131   bin/daq /path/to/the/log/file/in/the/output/data/folder

1132 where /path/to/the/log/file/in/the/output/data/folder is the only argument required. This  
 1133 log file is important for the webDCS as this file contains all the content of the communication of the  
 1134 webDCS and the different systems monitored by the webDCS. Its content is constantly displayed  
 1135 during data taking for the users to be able to follow the operations. The communication messages  
 1136 are normally sent to the webDCS log file via the functions declared in file MsgSvc.h, typically  
 1137 MSG\_INFO(string message).

1138

### 1139 A.3 Description of the readout setup

1140 The CMS RPC setup at GIF++ counts 5 V1190A Time-to-Digital Converter (TDC) manufactured  
 1141 by CAEN [57]. V1190A are VME units accepting 128 independent Multi-Hit/Multi-Event TDC  
 1142 channels whose signals are treated by 4 100 ps high performance TDC chips developed by CERN  
 1143 / ECP-MIC Division. The communication between the computer and the TDCs to transfer data is  
 1144 done via a V1718 VME master module also manufactured by CAEN and operated from a USB  
 1145 port [58]. These VME modules are all hosted into a 6U VME 6021 powered crate manufactured by  
 1146 W-Ie-Ne-R than can accommodate up to 21 VME bus cards [59]. These 3 components of the DAQ  
 1147 setup are shown in Figure A.1.

1148

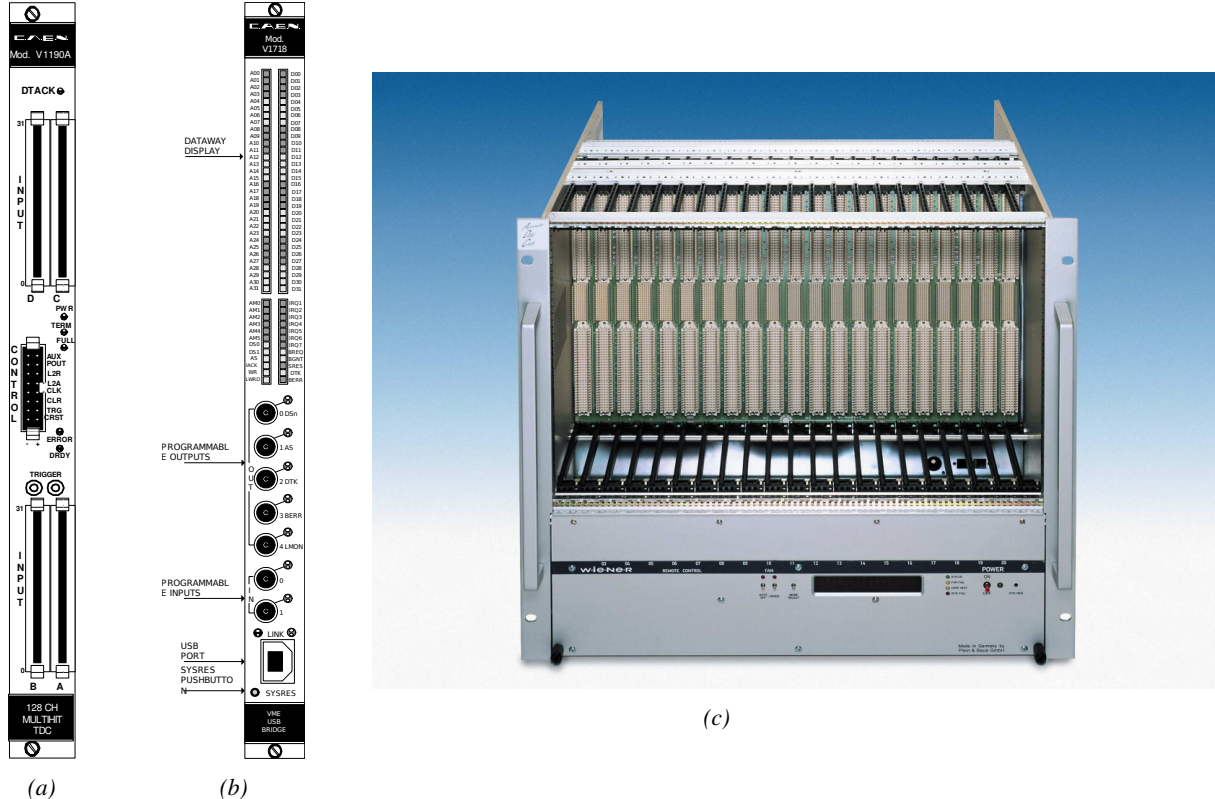


Figure A.1: (A.1a) View of the front panel of a V1190A TDC module [57]. (A.1b) View of the front panel of a V1718 Bridge module [58]. (A.1c) View of the front panel of a 6U 6021 VME crate [59].

1149

### A.4 Data read-out

1150 To efficiently perform a data readout algorithm, C++ objects to handle the VME modules (TDCs  
 1151 and VME bridge) have been created along with objects to store data and read the configuration file

1152 that comes as an input of the DAQ software.

1153

#### 1154 A.4.1 V1190A TDCs

1155 The DAQ used at GIF takes profit of the *Trigger Matching Mode* offered by V1190A modules.  
 1156 This setting is enabled through the method `v1190a::SetTrigMatching (int ntdcs)` where `ntdcs`  
 1157 is the total number of TDCs in the setup this setting needs to be enabled for (Source Code A.1). A  
 1158 trigger matching is performed in between a trigger time tag, a trigger signal sent into the TRIGGER  
 1159 input of the TDC visible on Figure A.1a, and the channel time measurements, signals recorded from  
 1160 the detectors under test in our case. Control over this data acquisition mode, explained through  
 1161 Figure A.2, is offered via 4 programmable parameters:

- 1162 • **match window:** the matching between a trigger and a hit is done within a programmable time  
 1163 window. This is set via the method

```
1164     void v1190a::SetTrigWindowWidth(UINT windowWidth, int ntdcs)
```

- 1165 • **window offset:** temporal distance between the trigger tag and the start of the trigger matching  
 1166 window. This is set via the method

```
1167     void v1190a::SetTrigWindowWidth(UINT windowWidth, int ntdcs)
```

- 1168 • **extra search margin:** an extended time window is used to ensure that all matching hits are  
 1169 found. This is set via the method

```
1170     void v1190a::SetTrigSearchMargin(UINT searchMargin, int ntdcs)
```

- 1171 • **reject margin:** older hits are automatically rejected to prevent buffer overflows and to speed  
 1172 up the search time. This is set via the method

```
1173     void v1190a::SetTrigRejectionMargin(UINT rejectMargin, int ntdcs)
```

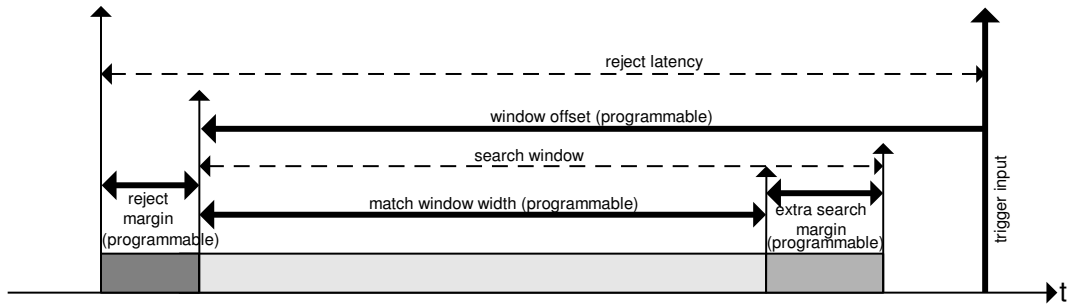


Figure A.2: Module V1190A Trigger Matching Mode timing diagram [57].

1174 Each of these 4 parameters are given in number of clocks, 1 clock being 25 ns long. It is easy to  
 1175 understand at this level that there are 3 possible functioning settings:

- 1176 • **1:** the match window is entirely contained after the trigger signal,
- 1177 • **2:** the match window overlaps the trigger signal, or
- 1178 • **3:** the match window is entirely contained before the trigger signal as displayed on Figure A.2.

1179 In both the first and second cases, the sum of the window width and of the offset can be set to  
1180 a maximum of 40 clocks, which corresponds to 1  $\mu$ s. Evidently, the offset can be negative, allowing  
1181 for a longer match window, with the constraint of having the window ending at most 1  $\mu$ s after the  
1182 trigger signal. In the third case, the maximum negative offset allowed is of 2048 clocks (12 bit) cor-  
1183 responding to 51.2  $\mu$ s, the match window being strictly smaller than the offset. In the case of GIF++,  
1184 the choice has been made to use this last setting by delaying the trigger signal. During the studies  
1185 performed in GIF++, both the efficiency of the RPCs, probed using a muon beam, and the noise or  
1186 gamma background rate are monitored. The extra search and reject margins are left unused.  
1187 To probe the efficiency of RPC detectors, the trigger time tag is provided by the coïncidence of  
1188 scintillators when a bunch of muons passes through GIF++ area is used to trigger the data acquisi-  
1189 tion. For this measurement, it is useful to reduce the match window width only to contain the muon  
1190 information. Indeed, the delay in between a trigger signal and the detection of the corresponding  
1191 muon in the RPC being very contant (typically a few tens of ns due to jitter and cable length), the  
1192 muon signals are very localised in time. Thus, due to a delay of approximalety 325 ns in between  
1193 the muons and the trigger, the settings where chosen to have a window width of 24 clocks (600 ns)  
1194 centered on the muon peak thanks to a negative offset of 29 clocks (725 ns).  
1195 On the otherhand, monitoring the rates don't require for the DAQ to look at a specific time window.  
1196 It is important to integrate enough time to have a robust measurement of the rate as the number of  
1197 hits per time unit. The triggerring signal is provided by a pulse generator at a frequency of 300 Hz  
1198 to ensure that the data taking occurs in a random way, with respect to beam physics, to probe only  
1199 the irradiation spectrum on the detectors. The match window is set to 400 clocks (10  $\mu$ s) and the  
1200 negative offset to 401 clocks as it needs to exceed the value of the match window.

```

1201
class v1190a
{
    private :
        long             Handle;
        vector<Data32>   Address;
        CVDataWidth      DataWidth;
        CVAddressModifier AddressModifier;

    public:

        v1190a(long handle, IniFile *inifile, int ntdcs);
        ~v1190a();
        Data16 write_op_reg(Data32 address, int code, string error);
        Data16 read_op_reg(Data32 address, string error);
        void Reset(int ntdcs);
        void Clear(int ntdcs);
        void TestWR(Data16 value,int ntdcs);
        void CheckTDCStatus(int ntdcs);
        void CheckCommunication(int ntdcs);
        void SetTDCTestMode(Data16 mode,int ntdcs);
        void SetTrigMatching(int ntdcs);
        void SetTrigTimeSubtraction(Data16 mode,int ntdcs);
        void SetTrigWindowWidth(Uint windowHeight,int ntdcs);
        void SetTrigWindowOffset(Uint windowOffset,int ntdcs);
        void SetTrigSearchMargin(Uint searchMargin,int ntdcs);
        void SetTrigRejectionMargin(Uint rejectMargin,int ntdcs);
        void GetTrigConfiguration(int ntdcs);
        void SetTrigConfiguration(IniFile *inifile,int ntdcs);
        void SetTDCDetectionMode(Data16 mode,int ntdcs);
        void SetTDCResolution(Data16 lsb,int ntdcs);
        void SetTDCDeadTime(Data16 time,int ntdcs);
        void SetTDCHeadTrailer(Data16 mode,int ntdcs);
        void SetTDCEventSize(Data16 size,int ntdcs);
        void SwitchChannels(IniFile *inifile,int ntdcs);
        void SetIRQ(Data32 level, Data32 count,int ntdcs);
        void SetBlockTransferMode(Data16 mode,int ntdcs);
        void Set(IniFile *inifile,int ntdcs);
        void CheckStatus(CVErrorCodes status) const;
        int ReadBlockD32(Uint tdc, const Data16 address,
                         Data32 *data, const Uint words, bool ignore_berr);
        Uint Read(RAWData *DataList,int ntdcs);
};

1202

```

1203       *Source Code A.1: Description of C++ object v1190a.*

1204       The v1190a object, defined in the DAQ software as in Source Code A.1, offers the possibility to  
 1205       concatenate all TDCs in the readout setup into a single object containing a list of hardware addresses  
 1206       (addresses to access the TDCs' buffer through the VME crate) and each constructor and method acts  
 1207       on the list of TDCs.  
 1208

#### 1209       A.4.2 DataReader

1210       Enabled thanks to v1190a::SetBlockTransferMode(Data16 mode, int ntdcs), the data transfer  
 1211       is done via Block Transfer (BLT). Using BLT allows to tranfer a fixed number of events called a  
 1212       *block*. This is used together with an Almost Full Level (AFL) of the TDCs' output buffers, defined

1213 through `v1190a::SetIRQ(Data32 level, Data32 count, int ntdcs)`. This AFL gives the maxi-  
 1214 mum amount of 32735 words (16 bits, corresponding to the depth of a TDC output buffer) that can  
 1215 written in a buffer before an Interrupt Request (IRQ) is generated and seen by the VME Bridge,  
 1216 stopping the data acquisition to transfer the content of each TDC buffers before resuming. For each  
 1217 trigger, 6 words or more are written into the TDC buffer:

- 1218     • a **global header** providing information of the event number since the beginning of the data  
       acquisition,
- 1220     • a **TDC header**,
- 1221     • the **TDC data** (*if any*), 1 for each hit recorded during the event, providing the channel and the  
       time stamp associated to the hit,
- 1223     • a **TDC error** providing error flags,
- 1224     • a **TDC trailer**,
- 1225     • a **global trigger time tag** that provides the absolute trigger time relatively to the last reset,  
       and
- 1227     • a **global trailer** providing the total word count in the event.

1228     As previously described in Section ??, CMS RPC FEEs provide us with 100 ns long LVDS out-  
 1229 put signals that are injected into the TDCs' input. Any avalanche signal that gives a signal above the  
 1230 FEEs threshold is thus recorded by the TDCs as a hit within the match window. Each hit is assigned  
 1231 to a specific TDC channel with a time stamp, with a precision of 100 ps. The reference time,  $t_0 = 0$ ,  
 1232 is provided by the beginning of the match window. Thus for each trigger, coming from a scintillator  
 1233 coïncidence or the pulse generator, a list of hits is stored into the TDCs' buffers and will then be  
 1234 transferred into a ROOT Tree.

1235     When the BLT is used, it is easy to understand that the maximum number of words that have  
 1236 been set as ALF will not be a finite number of events or, at least, the number of events that would  
 1237 be recorded into the TDC buffers will not be a multiple of the block size. In the last BLT cycle to  
 1238 tranfer data, the number of events to transfer will most probably be lower than the block size. In that  
 1239 case, the TDC can add fillers at the end of the block but this option requires to send more data to the  
 1240 computer and is thus a little slower. Another solution is to finish the transfer after the last event by  
 1241 sending a bus error that states that the BLT reached the last event in the pile. This method has been  
 1242 chosen in GIF++.

1244     Due to irradiation, an event in GIF++ can count up to 300 words per TDC. A limit of 4096 words  
 1245 (12 bits) has been set to generate IRQ which represent from 14 to almost 700 events depending on  
 1246 the average of hits collected per event. Then the block size has been set to 100 events with enabled  
 1247 bus errors. When an AFL is reached for one of the TDCs, the VME bridge stops the acquisition by  
 1248 sending a BUSY signal.

1250

The data is then transferred one TDC at a time into a structure called `RAWData` (Source Code A.2).

```
1252     struct RAWData{
1253         vector<int>                      *EventList;
1254         vector<int>                      *NHitsList;
1255         vector<int>                      *QFlagList;
1256         vector<vector<int> >            *ChannelList;
1257         vector<vector<float> >          *TimeStampList;
1258     };
1259 }
```

*Source Code A.2: Description of data holding C++ structure RAWData.*

In order to organize the data transfer and the data storage, an object called `DataReader` was created (Source Code A.3). On one hand, it has `v1718` and `v1190a` objects as private members for communication purposes, such as VME modules settings via the configuration file `*iniFile` or data read-out through `v1190a::Read()` and on the other hand, it contains the struture `RAWData` that allows to organise the data in vectors reproducing the tree structure of a ROOT file.

```
1260 class DataReader
{
    private:
        bool      StopFlag;
        IniFile  *iniFile;
        Data32   MaxTriggers;
        v1718    *VME;
        int       nTDCs;
        v1190a   *TDCs;
        RAWData  TDCData;

    public:
        DataReader();
        virtual ~DataReader();
        void     SetIniFile(string inifilename);
        void     SetMaxTriggers();
        Data32  GetMaxTriggers();
        void     SetVME();
        void     SetTDC();
        int      GetQFlag(Uint it);
        void     Init(string inifilename);
        void     FlushBuffer();
        void     Update();
        string  GetFileName();
        void     WriteRunRegistry(string filename);
        void     Run();
};

1261
```

1262 *Source Code A.3: Description of C++ object DataReader.*

1263 Each event is transferred from `TDCData` and saved into branches of a ROOT `TTree` as 3 integers  
 1264 that represent the event ID (`EventCount`), the number of hits read from the TDCs (`nHits`), and the  
 1265 quality flag that provides information for any problem in the data transfer (`qflag`), and 2 lists of  
 1266 `nHits` elements containing the fired TDC channels (`TDCch`) and their respective time stamps (`TDCTS`),  
 1267 as presented in Source Code A.4. The ROOT file file is named using information contained into  
 1268 the configuration file, presented in section A.5.2. The needed information is extracted using method  
 1269 `DataReader::GetFileName()` and allow to build the output filename format `ScanXXXXXX_HVX_DAQ.root`

1270 where ScanXXXXXX is a 6 digit number representing the scan number into GIFT++ database and HVX  
 1271 the HV step within the scan that can be more than a single digit. An example of ROOT data file is  
 1272 provided with Figure A.3.

```
1273
RAWData TDCData;
TFile *outputFile = new TFile(outputFileName.c_str(),"recreate");
TTree *RAWDataTree = new TTree("RAWData","RAWData");

int EventCount = -9;
int nHits = -8;
int qflag = -7;
vector<int> TDCCh;
vector<float> TDCTS;

RAWDataTree->Branch("EventNumber",&EventCount, "EventNumber/I");
RAWDataTree->Branch("number_of_hits",&nHits,"number_of_hits/I");
RAWDataTree->Branch("Quality_flag",&qflag,"Quality_flag/I");
RAWDataTree->Branch("TDC_channel",&TDCCh);
RAWDataTree->Branch("TDC_TimeStamp",&TDCTS);

1274
//...
//Here read the TDC data using v1190a::Read() and place it into
//TDCData for as long as you didn't collect the requested amount
//of data.
//...

for(Uint i=0; i<TDCData.EventList->size(); i++){
    EventCount = TDCData.EventList->at(i);
    nHits = TDCData.NHitsList->at(i);
    qflag = TDCData.QFlagList->at(i);
    TDCCh = TDCData.ChannelList->at(i);
    TDCTS = TDCData.TimeStampList->at(i);
    RAWDataTree->Fill();
}
```

1275 *Source Code A.4: Highlight of the data transfer and organisation within DataReader::Run() after the data has been collected into TDCData.*

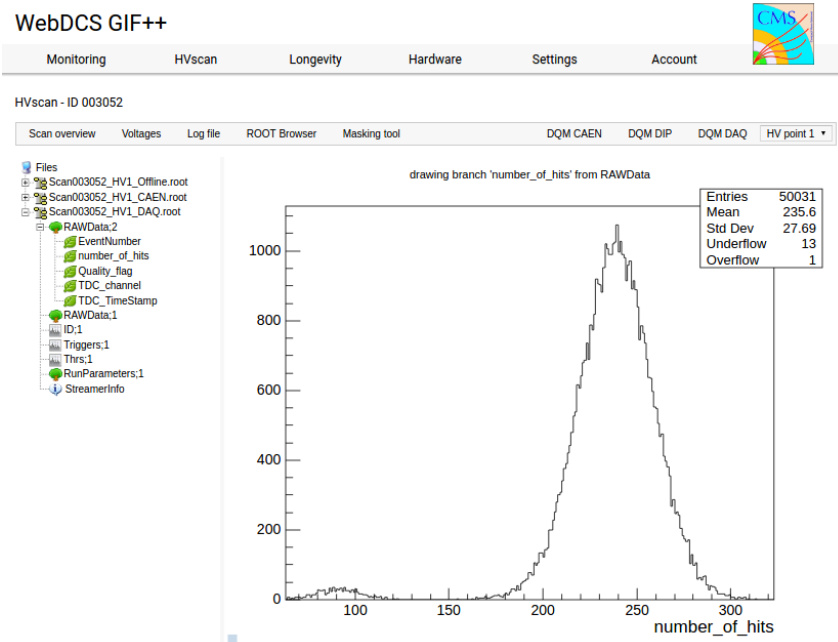


*Figure A.3: Structure of the ROOT output file generated by the DAQ. The 5 branches (EventNumber, number\_of\_hits, Quality\_flag, TDC\_channel and TDC\_TimeStamp) are visible on the left panel of the ROOT browser. On the right panel is visible the histogram corresponding to the variable nHits. In this specific example, there were approximately 50k events recorded to measure the gamma irradiation rate on the detectors. Each event is stored as a single entry in the TTree.*

#### 1276    A.4.3 Data quality flag

1277    Among the parameters that are recorded for each event, the quality flag, defined in Source Code A.5,  
 1278    is determined on the fly by checking the data recorded by every single TDC. From method `v1190a::Read()`,  
 1279    it can be understood that the content of each TDC buffer is readout one TDC at a time. Entries are  
 1280    created in the data list for the first TDC and then, when the second buffer is readout, events corre-  
 1281    sponding to entries that have already been created to store data for the previous TDC are added to  
 1282    the existing list element. On the contrary, when an event entry has not been yet created in the data  
 1283    list, a new entry is created.

```
1284
  typedef enum _QualityFlag {
    GOOD      = 1,
    CORRUPTED = 0
} QualityFlag;
```

1286    *Source Code A.5: Definition of the quality flag `enum`.*

1287    It is possible that each TDC buffer contains a different number of events. In cases where the first  
 1288    element in the buffer list is an event for corresponds to a new entry, the difference in between the  
 1289    entry from the buffer and the last entry in the data list is recorded and checked. If it is greater than 1,  
 1290    what should never be the case, the quality flag is set to CORRUPTED for this TDC and an empty entry  
 1291    is created in the place of the missing ones. Missing entries are believe to be the result of a bad hold

1292 on the TDC buffers at the moment of the readout. Indeed, the software hold is effective only on 1  
 1293 TDC at a time and no solution as been found yet to completely block the writting in the buffers when  
 1294 an IRQ is received.

1295 At the end of each BLT cycle, the ID of the last entry stored for each TDC buffer is not recorded.  
 1296 When starting the next cycle, if the first entry in the pile corresponds to an event already existing  
 1297 in the list, the readout will start from this list element and will not be able to check the difference  
 1298 in between this entry's ID and the one of the last entry that was recorded for this TDC buffer in  
 1299 the previous cycle. In the case events were missing, the flag stays at its initial value of 0, which is  
 1300 similar to CORRUPTED and it is assumed that then this TDC will not contribute to `number_of_hits`,  
 1301 `TDC_channel` or `TDC_TimeStamp`.

1302 Finally, since there will be 1 `RAWData` entry per TDC for each event (meaning `nTDCs` entries,  
 1303 referring to `DataReader` private attribute), the individual flags of each TDC will be added together.  
 1304 The final format is an integer composed `nTDCs` digits where each digit is the flag of a specific TDC.  
 1305 This is constructed using powers of 10 like follows:

```
1306 TDC 0: QFlag = 100 × _QualityFlag
1307 TDC 1: QFlag = 101 × _QualityFlag
1308 ...
1309 TDC N: QFlag = 10N × _QualityFlag
```

1310 and the final flag to be with N digits:

```
1311 QFlag = n....3210
```

1312 each digit being 1 or 0. Below is given an example with a 4 TDCs setup.

```
1313 If all TDCs were good : QFlag = 1111,
1314 but if TDC 2 was corrupted : QFlag = 1011.
```

1315 When data taking is over and the data contained in the dynamical `RAWData` structure is transferred  
 1316 to the ROOT file, all the 0s are changed into 2s by calling the method `DataReader::GetQFlag()`.  
 1317 This will help translating the flag without knowing the number of TDCs beforehand. Indeed, a flag  
 1318 111 could be due to a 3 TDC setup with 3 good individual TDC flags or to a more than 3 TDC setup  
 1319 with TDCs those ID is greater than 2 being CORRUPTED, thus giving a 0.

1320 The quality flag has been introduced quite late, in October 2017 only, to the list of GIFT++ DAQ  
 1321 parameters to be recorded into the output ROOT file. Before this addition, the missing data, corrupting  
 1322 the quality for the offline analysis, was contributing to artificially fill data with lower multiplicity.  
 1323 Looking at `TBranch number_of_hits` provides an information about the data of the full GIFT++  
 1324 setup. When a TDC is not able to transfer data for a specific event, the effect is a reduction of the  
 1325 total number of hits recorded in the full setup, this is what can be seen from Figure A.4. After offline  
 1326 reconstruction detector by detector, the effect of missing events can be seen in the artificially filled  
 1327 bin at multiplicity 0 shown in Figure A.5. Nonetheless, for data with high irradiation levels, as it is  
 1328 the case for Figure A.5a, discarding the fake multiplicity 0 data can be done easily during the offline  
 1329 analysis. At lower radiation, the missing events contribution becomes more problematic as the multi-  
 1330 tiplicity distribution overlaps the multiplicity 0 and that in the same time the proportion of missing

events decreases. Attempts to fit the distribution with a Poisson or skew distribution function were not conclusive and this very problem has been at the origin of the quality flag that allows to give a non ambiguous information about each event quality.

1334

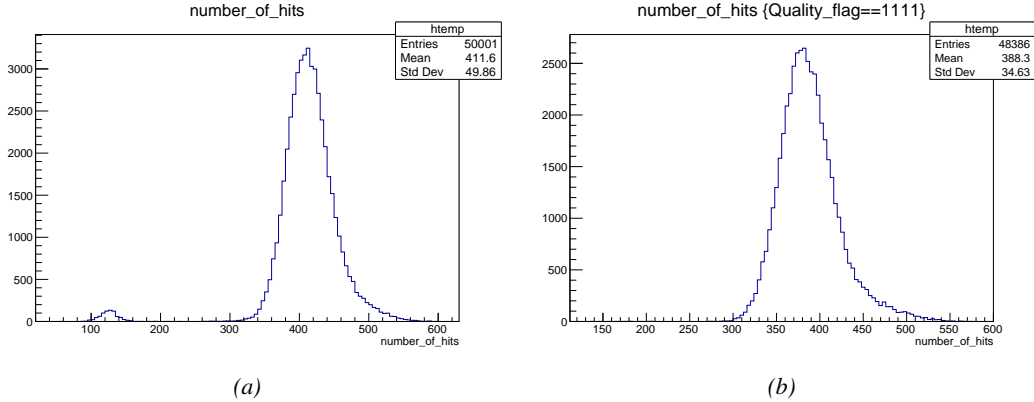


Figure A.4: The effect of the quality flag is explained by presenting the content of TBranch `number_of_hits` of a data file without `Quality_flag` in Figure A.4a and the content of the same TBranch for data corresponding to a `Quality_flag` where all TDCs were labelled as `GOOD` in Figure A.4b taken with similar conditions. It can be noted that the number of entries in Figure A.4b is slightly lower than in Figure A.4a due to the excluded events.

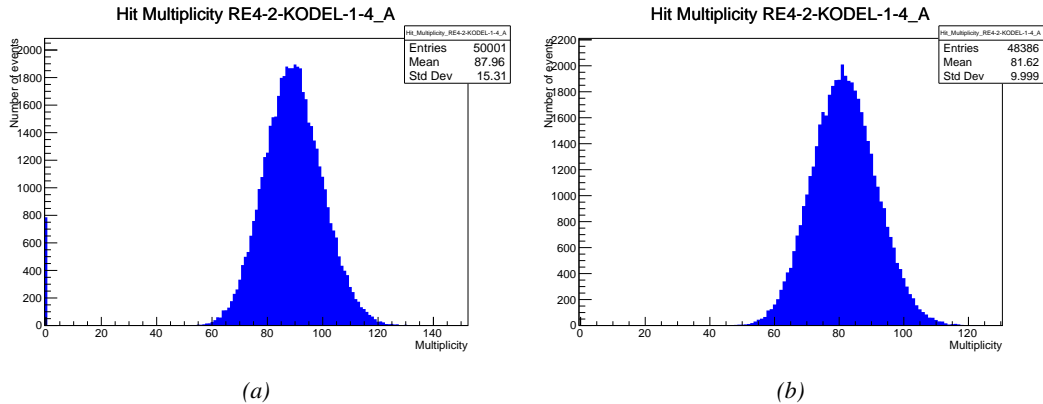


Figure A.5: Using the same data as previously showed in Figure A.4, the effect of the quality flag is explained by presenting the reconstructed hit multiplicity of a data file without `Quality_flag` in Figure A.5a and the reconstructed content of the same RPC partition for data corresponding to a `Quality_flag` where all TDCs were labelled as `GOOD` in Figure A.5b taken with similar conditions. The artificial high content of bin 0 is completely suppressed.

1335

## A.5 Communications

1336  
1337

To ensure data readout and dialog in between the machine and the TDCs or in between the webDCS and the DAQ, different communication solutions were used. First of all, it is important to have a

1338 module to allow the communication in between the TDCs and the computer from which the DAQ  
 1339 operates. When this communication is effective, shifters using the webDCS to control data taking  
 1340 can thus send instructions to the DAQ.

1341

### 1342 A.5.1 V1718 USB Bridge

1343 In the previous section, the data transfer has been discussed. The importance of the `v1718` object  
 1344 (Source Code A.6), used as private member of `DataReader`, was not explicated. VME master  
 1345 modules are used for communication purposes as they host the USB port that connects the pow-  
 1346 ered crate buffer to the computer where the DAQ is installed. From the source code point of view,  
 1347 this object is used to control the communication status, by reading the returned error codes with  
 1348 `v1718::CheckStatus()`, or to check for IRQs coming from the TDCs through `v1718::CheckIRQ()`.  
 1349 Finally, to ensure that triggers are blocked at the hardware level, a NIM pulse is sent out of one of the  
 1350 5 programmable outputs (`v1718::SendBUSY()`) to the VETO of the coincidence module where the  
 1351 trigger signals originate from. As long as this signal is ON, no trigger can reach the TDCs anymore.  
 1352

```
1353
  class v1718{
    private:
      int Handle;
      Data32 Data;           // Data
      CVIRQLevels Level;    // Interrupt level
      CVAddressModifier AM;  // Addressing Mode
      CVDataWidth dataSize; // Data Format
      Data32 BaseAddress;   // Base Address

    public:
      v1718(IniFile *inifile);
      ~v1718();
      long GetHandle(void) const;
      int SetData(Data16 data);
      Data16 GetData(void);
      int SetLevel(CVIRQLevels level);
      CVIRQLevels GetLevel(void);
      int SetAM(CVAddressModifier am);
      CVAddressModifier GetAM(void);
      int SetDatasize(CVDataWidth datasize);
      CVDataWidth GetDataSize(void);
      int SetBaseAddress(Data16 baseaddress);
      Data16 GetBaseAddress(void);
      void CheckStatus(CVErrorCodes status) const;
      void CheckIRQ();
      void SetPulsers();
      void SendBUSY(BusyLevel level);
  };

```

1354

*Source Code A.6: Description of C++ object v1718.*

### 1355 A.5.2 Configuration file

1356 The DAQ software takes as input a configuration file written using INI standard [60]. This file is  
 1357 partly filled with the information provided by the shifters when starting data acquisition using the  
 1358 webDCS, as shown by Figure A.6. This information is written in section [`General`] and will later

1359 be stored in the ROOT file that contains the DAQ data as can be seen from Figure A.3. Indeed,  
 1360 another `TTree` called `RunParameters` as well as the 2 histograms `ID`, containing the scan number,  
 1361 start and stop time stamps, and `Triggers`, containing the number of triggers requested by the shifter,  
 1362 are available in the data files. Moreover, `ScanID` and `HV` are then used to construct the file name  
 1363 thanks to the method `DataReader::GetFileName()`.

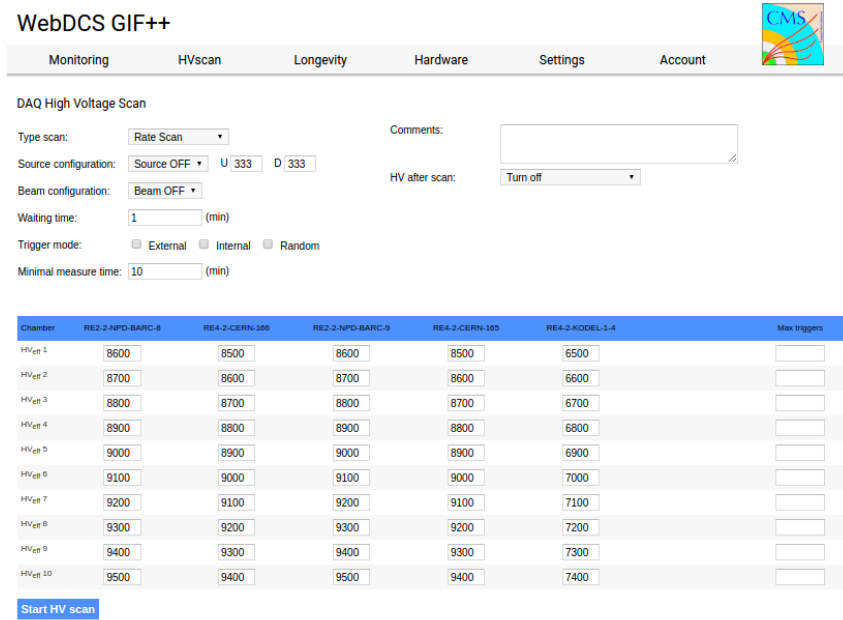


Figure A.6: WebDCS DAQ scan page. On this page, shifters need to choose the type of scan (Rate, Efficiency or Noise Reference scan), the gamma source configuration at the moment of data taking, the beam configuration, and the trigger mode. These information will be stored in the DAQ ROOT output. Are also given the minimal measurement time and waiting time after ramping up of the detectors is over before starting the data acquisition. Then, the list of HV points to scan and the number of triggers for each run of the scan are given in the table underneath.

1364 The rest of the information is written beforehand in the configuration file template, as explicated  
 1365 in Source Code A.7, and contains the hardware addresses to the different VME modules in the  
 1366 setup as well as settings for the TDCs. As the TDC settings available in the configuration file are not  
 1367 supposed to be modified, an improvement would be to remove them from the configuration file and  
 1368 to hardcode them inside of the DAQ code itself or to place them into a different INI file that would  
 1369 host only the TDC settings to lower the probability for a bad manipulation of the configuration file  
 1370 that can be modified from one of webDCS' menus.

1371

```
[General]
TdcS=4
ScanID=$scanid
HV=$HV
RunType=$runtype
MaxTriggers=$maxtriggers
Beam=$beam
[VMEInterface]
Type=V1718
BaseAddress=0xFF0000
Name=VmeInterface
[TDC0]
Type=V1190A
BaseAddress=0x00000000
Name=Tdc0
StatusA00-15=1
StatusA16-31=1
StatusB00-15=1
StatusB16-31=1
StatusC00-15=1
StatusC16-31=1
StatusD00-15=1
StatusD16-31=1
[TDC1]
Type=V1190A
BaseAddress=0x11110000
Name=Tdc1
StatusA00-15=1
StatusA16-31=1
StatusB00-15=1
StatusB16-31=1
StatusC00-15=1
StatusC16-31=1
StatusD00-15=1
StatusD16-31=1
[TDC2]
Type=V1190A
BaseAddress=0x22220000
Name=Tdc2
StatusA00-15=1
StatusA16-31=1
StatusB00-15=1
StatusB16-31=1
StatusC00-15=1
StatusC16-31=1
StatusD00-15=1
StatusD16-31=1
[TDC3]
Type=V1190A
BaseAddress=0x44440000
Name=Tdc3
StatusA00-15=1
StatusA16-31=1
StatusB00-15=1
StatusB16-31=1
StatusC00-15=1
StatusC16-31=1
StatusD00-15=1
StatusD16-31=1
[TDCSettings]
TriggerExtraSearchMargin=0
TriggerRejectMargin=0
TriggerTimeSubtraction=0b1
TdcDetectionMode=0b01
TdcResolution=0b10
TdcDeadTime=0b00
TdcHeadTrailer=0b1
TdcEventSize=0b1001
TdcTestMode=0b0
BLTMode=1
```

*Source Code A.7: INI configuration file template for 4 TDCs. In section [General], the number of TDCs is explicitated and information about the ongoing run is given. Then, there are sections for each and every VME modules. There buffer addresses are given and for the TDCs, the list of channels to enable is given. Finally, in section [TDCSettings], a part of the TDC settings are given.*

1374     In order to retrieve the information of the configuration file, the object `IniFile` has been developed  
 1375     to provide an INI parser, presented in Source Code A.8. It contains private methods returning a  
 1376     boolean to check the type of line written in the file, whether a comment, a group header or a key line  
 1377     (`IniFile::CheckIfComment()`, `IniFile::CheckIfGroup()` and `IniFile::CheckIfToken()`). The  
 1378     key may sometimes be referred to as *token* in the source code. Moreover, the private element  
 1379     `FileData` is a map of `const string` to `string` that allows to store the data contained inside the  
 1380     configuration file via the public method `IniFile::GetFileData()` following the formatting (see  
 1381     method `IniFile::Read()`):

```
1382
  1383     string group, token, value;
  // Get the field values for the 3 strings.
  // Then concatenate group and token together as a single string
  // with a dot separation.
  token = group + "." + token;
  FileData[token] = value;
```

1384     More methods have been written to translate the different keys into the right variable format  
 1385     when used by the DAQ. For example, to get a `float` value out of the configuration file data, knowing  
 1386     the group and the key needed, the method `IniFile::floatType()` can be used. It takes 3 arguments  
 1387     being the group name and key name (both `string`), and a default `float` value used as exception in  
 1388     the case the expected combination of group and key cannot be found in the configuration file. This  
 1389     default value is then used and the DAQ continues on working after sending an alert in the log file for  
 1390     further debugging.

```

1391 typedef map< const string, string > IniFileData;
1392
class IniFile{
    private:
        bool          CheckIfComment (string line);
        bool          CheckIfGroup(string line, string& group);
        bool          CheckIfToken(string line, string& key, string& value);
        string         FileName;
        IniFileData   FileData;
        int           Error;

    public:
        IniFile();
        IniFile(string filename);
        virtual      ~IniFile();

        // Basic file operations
        void          SetFileName(string filename);
        int           Read();
        int           Write();
        IniFileData GetFileData();

        // Data readout methods
        Data32         addressType (string groupname, string keyname, Data32
→     defaultvalue);
        long          intType     (string groupname, string keyname, long
→     defaultvalue);
        long long    longType    (string groupname, string keyname, long long
→     defaultvalue );
        string         stringType  (string groupname, string keyname, string
→     defaultvalue );
        float         floatType   (string groupname, string keyname, float
→     defaultvalue );

        // Error methods
        string         GetErrorMsg();
    };

```

1393       *Source Code A.8: Description of C++ object `IniFile` used as a parser for INI file format.*

### 1394       A.5.3 WebDCS/DAQ intercommunication

1395       When shifters send instructions to the DAQ via the configuration file, it is the webDCS itself that  
 1396       gives the start command to the DAQ and then the 2 softwares use inter-process communication  
 1397       through file to synchronise themselves. This communication file is represented by the variable **const**  
 1398       string \_\_runstatuspath.

1399       On one side, the webDCS sends commands or status that are readout by the DAQ:

- 1400       • INIT, status sent when launching a scan and read via function `CtrlRunStatus(...)`,
- 1401       • START, command to start data taking and read via function `CheckSTART()`,
- 1402       • STOP, command to stop data taking at the end of the scan and read via function `CheckSTOP()`,  
 1403        and
- 1404       • KILL, command to kill data taking sent by user and read via function `CheckKILL()`

1405 and on the other, the DAQ sends status that are controled by the webDCS:

- 1406     ● `DAQ_RDY`, sent with `SendDAQReady()` to signify that the DAQ is ready to receive commands  
1407       from the webDCS,
- 1408     ● `RUNNING`, sent with `SendDAQRunning()` to signify that the DAQ is taking data,
- 1409     ● `DAQ_ERR`, sent with `SendDAQError()` to signify that the DAQ didn't receive the expected com-  
1410       mand from the webDCS or that the launch command didn't have the right number of argu-  
1411       ments,
- 1412     ● `RD_ERR`, sent when the DAQ wasn't able to read the communication file, and
- 1413     ● `WR_ERR`, sent when the DAQ wasn't able to write into the communication file.

#### 1414     **A.5.4 Example of inter-process communication cycle**

1415 Under normal conditions, the webDCS and the DAQ processes exchange commands and status via  
1416 the file hosted at the address `__runstatuspath`, as explained in subsection A.5.3. An example of  
1417 cycle is given in Table A.1. In this example, the steps 3 to 5 are repeated as long as the webDCS tells  
1418 the DAQ to take data. A data taking cycle is the equivalent as what is called a *Scan* in GIFT++ jargon,  
1419 referring to a set a runs with several HV steps. Each repetition of steps 3 to 5 is then equivalent to a  
1420 single *Run*.

1421

1422 At any moment during the data taking, for any reason, the shifter can decide that the data taking  
1423 needs to be stopped before it reached the end of the scheduled cycle. Thus at any moment on the  
1424 cycle, the content of the inter-process communication file will be changed to `KILL` and the DAQ will  
1425 shut down right away. The DAQ checks for `KILL` signals every 5s after the TDCs configuration is  
1426 over. So far, the function `CheckKILL()` has been used only inside of the data taking loop of method  
1427 `DataReader::Run()` and thus, if the shifter decides to KILL the data taking during the TDC con-  
1428 figuration phase or the HV ramping in between 2 HV steps, the DAQ will not be stopped smoothly  
1429 and a *force kill* command will be sent to stop the DAQ process that is still awake on the computer.  
1430 Improvements can be brought on this part of the software to make sure that the DAQ can safely  
1431 shutdown at any moment.

1432

#### 1433     **A.6 Software export**

1434 In section A.2 was discussed the fact that the DAQ as written in its last version is not a standalone  
1435 software. It is possible to make it a standalone program that could be adapted to any VME setup  
1436 using V1190A and V1718 modules by creating a GUI for the software or by printing the log mes-  
1437 sages that are normally printed in the webDCS through the log file, directly into the terminal. This  
1438 method was used by the DAQ up to version 3.0 moment where the webDCS was completed. Also, it  
1439 is possible to check branches of DAQ v2.X to have example of communication through a terminal.

1440

1441 DAQ v2.X is nonetheless limited in it's possibilities and requires a lot of offline manual interven-  
1442 tions from the users. Indeed, there is no communication of the software with the detectors' power  
1443 supply system that would allow for a user a predefine a list of voltages to operate the detectors at

step	actions of webDCS	status of DAQ	<code>__runstatuspath</code>
1	launch DAQ ramp voltages ramping over wait for currents stabilization	readout of IniFile configuration of TDCs	INIT
2		configuration done send DAQ ready wait for START signal	DAQ_RDY
3	waiting time over send START		START
4	wait for run to end monitor DAQ run status	data taking ongoing check for KILL signal	RUNNING
5		run over send DAQ_RDY wait for next DCS signal	DAQ_RDY
6	ramp voltages ramping over wait for currents stabilization		DAQ_RDY
3	waiting time over send START		START
4	wait for run to end monitor DAQ run status	update IniFile information data taking ongoing check for KILL signal	RUNNING
5		run over send DAQ_RDY wait for next DCS signal	DAQ_RDY
7	send command STOP	DAQ shuts down	STOP

Table A.1: Inter-process communication cycles in between the webDCS and the DAQ through file string signals.

1444 and loop over to take data without any further manual intervention. In v2.X, the data is taken for a  
1445 single detector setting and at the end of each run, the softwares asks the user if he intends on taking  
1446 more runs. If so, the software invites the user to set the operating voltages accordingly to what is  
1447 necessary and to manual update the configuration file in consequence. This working mode can be a  
1448 very first approach before an evolution and has been successfully used by colleagues from different  
1449 collaborations.

1450  
1451 For a more robust operation, it is recommended to develop a GUI or a web application to inter-  
1452 face the DAQ. Moreover, to limit the amount of manual interventions, and thus the probability to  
1453 make mistakes, it is also recommended to add an extra feature into the DAQ by installing the HV  
1454 Wrapper library provided by CAEN of which an example of use in a similar DAQ software devel-  
1455 opped by a master student of UGent, and called TinyDAQ, is provided on UGent's github. Then, this  
1456 HV Wrapper will help you communicating with and give instructions to a CAEN HV powered crate  
1457 and can be added into the DAQ at the same level where the communication with the user was made  
1458 in DAQ v2.X. In case you are using another kind of power system for your detectors, it is stringly  
1459 adviced to use HV modules or crates that can be remotely controled via a using C++ libraries.  
1460

# B

1461

1462

## Details on the offline analysis package

1463 The data collected in GIF++ thanks to the DAQ described in Appendix A is difficult to interpret by  
1464 a human user that doesn't have a clear idea of the raw data architecture of the ROOT data files. In  
1465 order to render the data human readable, a C++ offline analysis tool was designed to provide users  
1466 with detector by detector histograms that give a clear overview of the parameters monitored during  
1467 the data acquisition [61]. In this appendix, details about this software in the context of GIF++, as of  
1468 how the software was written and how it functions will be given.

### 1469 B.1 GIF++ Offline Analysis file tree

1470 GIF++ Offline Analysis source code is fully available on github at [https://github.com/afagot/GIF\\_OfflineAnalysis](https://github.com/afagot/GIF_OfflineAnalysis). The software requires ROOT as non-optionnal dependency  
1471 as it takes ROOT files in input and write an output ROOT file containing histograms. To compile the  
1472 GIF++ Offline Analysis project is compiled with cmake. To compile, first a build/ directory must  
1473 be created to compile from there:

```
1475 mkdir build  
1476 cd build  
1477 cmake ..  
1478 make  
1479 make install
```

1477 To clean the directory and create a new build directory, the bash script cleandir.sh can be used:

```
1478  
1479 ./cleandir.sh
```

1480 The source code tree is provided below along with comments to give an overview of the files' con-  
1481 tent. The different objects created for this project (`Infrastructure`, `Trolley`, `RPC`, `Mapping`, `RPCHit`,  
1482 `RPCCluster` and `Inifile`) will be described in details in the following sections.

1483

```

GIF_OfflineAnalysis
├── bin
│   └── offlineanalysis ..... EXECUTABLE
├── build..... CMAKE COMPILATION DIRECTORY
└── ...
    ├── include..... LIST OF C++ HEADER FILES
    │   ├── Cluster.h..... DECLARATION OF OBJECT RPCCLUSTER
    │   ├── Current.h..... DECLARATION OF GETCURRENT ANALYSIS MACRO
    │   ├── GIFTrolley.h..... DECLARATION OF OBJECT TROLLEY
    │   ├── Infrastructure.h..... DECLARATION OF OBJECT INFRASTRUCTURE
    │   ├── IniFile.h..... DECLARATION OF OBJECT INI FILE FORINI PARSER
    │   ├── Mapping.h..... DECLARATION OF OBJECT MAPPING
    │   ├── MsgSvc.h..... DECLARATION OF OFFLINE LOG MESSAGES
    │   ├── OfflineAnalysis.h..... DECLARATION OF DATA ANALYSIS MACRO
    │   ├── RPCTracker.h..... DECLARATION OF OBJECT RPC
    │   ├── RPCHit.h..... DECLARATION OF OBJECT RPCHIT
    │   ├── types.h..... DEFINITION OF USEFUL VARIABLE TYPES
    │   └── utils.h..... DECLARATION OF USEFUL FUNCTIONS
    ├── obj..... BINARY FILES CREATED BY COMPILER
    └── ...
        ├── src..... LIST OF C++ SOURCE FILES
        │   ├── Cluster.cc..... DEFINITION OF OBJECT RPCCLUSTER
        │   ├── Current.cc .....

```

## 1484 B.2 Usage of the Offline Analysis

1485 In order to use the Offline Analysis tool, it is necessary to know the Scan number and the HV Step  
 1486 of the run that needs to be analysed. This information needs to be written in the following format:

1487

1488 Scan00XXXX\_HVY

1489 where XXXX is the scan ID and y is the high voltage step (in case of a high voltage scan, data will be  
 1490 taken for several HV steps). This format corresponds to the base name of data files in the database

1491 of the GIF++ webDCS. Usually, the offline analysis tool is automatically called by the webDCS at  
 1492 the end of data taking or by a user from the webDCS panel if an update of the tool was brought.  
 1493 Nonetheless, an expert can locally launch the analysis for tests on the GIF++ computer, or a user can  
 1494 get the code on its local machine from github and download data from the webDCS for its own anal-  
 1495 ysis. To launch the code, the following command can be used from the `GIF_OfflineAnalysis` folder:

1496  
 1497     `bin/offlineanalysis /path/to/Scan00XXXX_HVY`

1498 where, `/path/to/Scan00XXXX_HVY` refers to the local data files. Then, the offline tool will by itself  
 1499 take care of finding all available ROOT data files present in the folder, as listed below:

- 1500
  - `Scan00XXXX_HVY_DAQ.root` containing the TDC data as described in Appendix ?? (events, hit  
     1501       and timestamp lists), and
  - `Scan00XXXX_HVY_CAEN.root` containing the CAEN mainframe data recorded by the monitor-  
     1503       ing tool webDCS during data taking (HVs and currents of every HV channels). This file is  
     1504       created independently of the DAQ.

## 1505     **B.2.1 Output of the offline tool**

### 1506     **B.2.1.1 ROOT file**

1507 The analysis gives in output ROOT datafiles that are saved into the data folder and called using the  
 1508 naming convention `Scan00XXXX_HVY_Offline.root`. Inside those, a list of `TH1` histograms can be  
 1509 found. Its size will vary as a function of the number of detectors in the setup as each set of histograms  
 1510 is produced detector by detector. For each partition of each chamber, can be found:

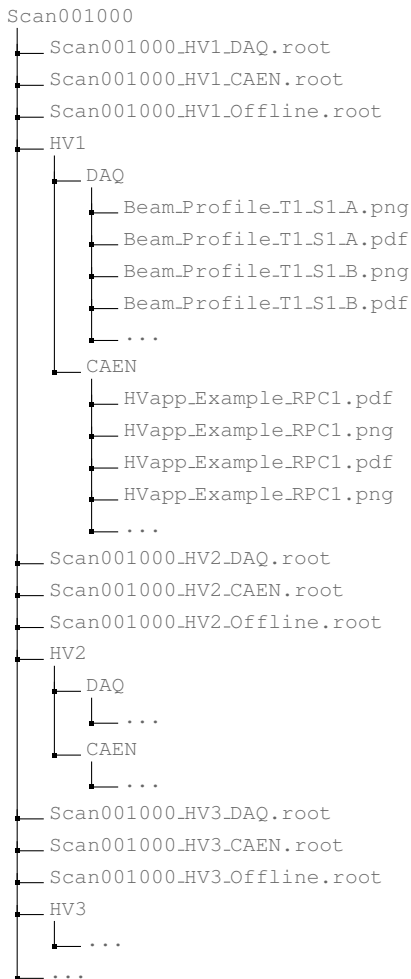
- 1511
  - `Time_Profile_Tt_Sc_p` shows the time profile of all recorded events (number of events per  
     1512       time bin),
  - `Hit_Profile_Tt_Sc_p` shows the hit profile of all recorded events (number of events per chan-  
     1514       nel),
  - `Hit_Multiplicity_Tt_Sc_p` shows the hit multiplicity (number of hits per event) of all recorded  
     1516       events (number of occurrences per multiplicity bin),
  - `Strip_Mean_Noise_Tt_Sc_p` shows noise/gamma rate per unit area for each strip in a se-  
     1518       lected time range. After filters are applied on `Time_Profile_Tt_Sc_p`, the filtered version  
     1519       of `Hit_Profile_Tt_Sc_p` is normalised to the total integrated time and active detection area  
     1520       of a single channel,
  - `Strip_Activity_Tt_Sc_p` shows noise/gamma activity for each strip (normalised version of  
     1522       previous histogram - strip activity = strip rate / average partition rate),
  - `Strip_Homogeneity_Tt_Sc_p` shows the *homogeneity* of a given partition ( $\text{homogeneity} = \exp(-\text{strip rates standard deviation}(\text{strip rates in partition}/\text{average partition rate}))$ ),
  - `mask_Strip_Mean_Noise_Tt_Sc_p` shows noise/gamma rate per unit area for each masked  
     1526       strip in a selected time range. Offline, the user can control the noise/gamma rate and decide to  
     1527       mask the strips that are judged to be noisy or dead. This is done via the *Masking Tool* provided  
     1528       by the webDCS,

- 1529     ● `mask_Strip_Activity_Tt_Sc_p` shows noise/gamma activity per unit area for each masked  
1530       strip with respect to the average rate of active strips,
- 1531     ● `NoiseCSize_H_Tt_Sc_p` shows noise/gamma cluster size, a cluster being constructed out of  
1532       adjacent strips giving a signal at the *same time* (hits within a time window of 25 ns),
- 1533     ● `NoiseCMult_H_Tt_Sc_p` shows noise/gamma cluster multiplicity (number of reconstructed  
1534       clusters per event),
- 1535     ● `Chip_Mean_Noise_Tt_Sc_p` shows the same information than `Strip_Mean_Noise_Tt_Scp` us-  
1536       ing a different binning (1 chip corresponds to 8 strips),
- 1537     ● `Chip_Activity_Tt_Sc_p` shows the same information than `Strip_Activity_Tt_Scp` using  
1538       chip binning,
- 1539     ● `Chip_Homogeneity_Tt_Sc_p` shows the homogeneity of a given partition using chip binning,
- 1540     ● `Beam_Profile_Tt_Sc_p` shows the estimated beam profile when taking efficiency scan. This  
1541       is obtained by filtering `Time_Profile_Tt_Sc_p` to only consider the muon peak where the  
1542       noise/gamma background has been subtracted. The resulting hit profile corresponds to the  
1543       beam profile on the detector channels,
- 1544     ● `L0_Efficiency_Tt_Sc_p` shows the level 0 efficiency that was estimated **without** muon track-  
1545       ing,
- 1546     ● `MuonCSize_H_Tt_Sc_p` shows the level 0 muon cluster size that was estimated **without** muon  
1547       tracking, and
- 1548     ● `MuonCMult_H_Tt_Sc_p` shows the level 0 muon cluster multiplicity that was estimated **without**  
1549       muon tracking.

1550     In the histogram labels,  $t$  stands for the trolley number (1 or 3),  $c$  for the chamber slot label in  
1551       trolley  $t$  and  $p$  for the partition label (A, B, C or D depending on the chamber layout) as explained  
1552       in Chapter ??.

1553  
1554     In the context of GIF++, an extra script called by the webDCS is called to extract the histograms  
1555       from the ROOT files. The histograms are then stored in PNG and PDF formats into the correspond-  
1556       ing folder (a single folder per HV step, so per ROOT file). the goal is to then display the histograms  
1557       on the Data Quality Monitoring (DQM) page of the webDCS in order for the users to control the  
1558       quality of the data taking at the end of data taking. An example of histogram organisation is given  
1559       below:

1560



**1561      Here can put some screens from the webDCS to show the DQM and the plots available to users.**

**1562**

### **1563      B.2.1.2 CSV files**

**1564** Moreover, up to 3 CSV files can be created depending on which ones of the 3 input files were in the  
**1565** data folder:

- 1566**      • `Offline-Corrupted.csv`, is used to keep track of the amount of data that was corrupted and  
**1567** removed from old data format files that don't contain any data quality flag.
- 1568**      • `Offline-Current.csv`, contains the summary of the currents and voltages applied on each  
**1569** RPC HV channel.
- 1570**      • `Offline-L0-EffC1.csv`, is used to write the efficiencies, cluster size and cluster multiplicity  
**1571** of efficiency runs. Note that `L0` refers here to *Level 0* and means that the results of efficiency and  
**1572** clusterization are a first approximation calculated without performing any muon tracking in

1573 between the different detectors. This offline tool provides the user with a preliminar calculation  
 1574 of the efficiency and of the muon event parameters. Another analysis software especially  
 1575 dedicated to muon tracking is called on selected data to retrieve the results of efficiency and  
 1576 muon clusterization using a tracking algorithm to discriminate noise or gamma from muons  
 1577 as muons are the only particles that pass through the full setup, leaving hits than can be used  
 1578 to reconstruct their tracks.

- 1579     ● `Offline-Rate.csv`, is used to write the noise or gamma rates measured in the detector readout  
 1580 partitions.

1581 Note that these 4 CSV files are created along with their *headers* (`Offline-[...]-Header.csv`  
 1582 containing the names of each data columns) and are automatically merged together when the offline  
 1583 analysis tool is called from the webDCS, contrary to the case where the tool is runned locally from  
 1584 the terminal as the merging bash script is then not called. Thus, the resulting files, used to make  
 1585 official plots, are:

- 1586     ● `Corrupted.csv`,  
 1587     ● `Current.csv`,  
 1588     ● `L0-EffCl.csv`.  
 1589     ● `Rate.csv`.

## 1590     **B.3 Analysis inputs and information handling**

1591 The usage of the Offline Analysis tool as well as its output have been presented in the previous section.  
 1592 It is now important to dig further and start looking at the source code and the inputs necessary  
 1593 for the tool to work. Indeed, other than the raw ROOT data files that are analysed, more information  
 1594 needs to be imported inside of the program to perform the analysis such as the description of the  
 1595 setup inside of GIFT++ at the time of data taking (number of trolleys, of RPCs, dimensions of the  
 1596 detectors, etc...) or the mapping that links the TDC channels to the coresponding RPC channels in  
 1597 order to translate the TDC information into human readable data. 2 files are used to transmit all this  
 1598 information:  
 1599

- 1600     ● `Dimensions.ini`, that provides the necessary setup and RPC information, and  
 1601     ● `ChannelsMapping.csv`, that gives the link between the TDC and RPC channels as well as the  
 1602 *mask* for each channel (masked or not?).

### 1603     **B.3.1 Dimensions file and InFile parser**

1604 This input file, present in every data folder, allows the analysis tool to know of the number of active  
 1605 trolleys, the number of active RPCs in those trolleys, and the details about each RPCs such as  
 1606 the number of RPC gaps, the number of pseudo-rapidity partitions (for CMS-like prototypes), the  
 1607 number of strips per partion or the dimensions. To do so, there are 3 types of groups in the INI file  
 1608 architecture. A first general group, appearing only once at the head of the document, gives information  
 1609 about the number of active trolleys as well as their IDs, as presented in Source Code B.1. For

1610 each active trolley, a group similar to Source Code B.2 can be found containing information about  
 1611 the number of active detectors in the trolley and their IDs. Each trolley group as a `Tt` name format,  
 1612 where `t` is the trolley ID. Finally, for each detector stored in slots of an active trolley, there is a group  
 1613 providing information about their names and dimensions, as shown in Source Code B.3. Each slot  
 1614 group as a `TtSs` name format, where `s` is the slot ID of trolley `t` where the active RPC is hosted.

```
1615 [General]
1616 nTrolleys=2
  TrolleysID=13
```

1617 *Source Code B.1: Example of `[General]` group as might be found in `Dimensions.ini`. In Gif++, only 2  
 trolleys are available to hold RPCs and place them inside of the bunker for irradiation. The IDs of the trolleys  
 are written in a single string as "13" and then read character by character by the program.*

```
1618 [T1]
  nSlots=4
  SlotsID=1234
```

1619 *Source Code B.2: Example of trolley group as might be found in `Dimensions.ini`. In this example, the file  
 tells that there are 4 detectors placed in the holding slots of the trolley `T1` and that their IDs, written as a single  
 string variable, are 1, 2, 3 and 4.*

```
1620 [T1S1]
  Name=RE2-2-NPD-BARC-8
  Partitions=3
  Gaps=3
  Gap1=BOT
  Gap2=TN
  Gap3=TW
  AreaGap1=11694.25
  AreaGap2=6432
  AreaGap3=4582.82
  Strips=32
  ActiveArea-A=157.8
  ActiveArea-B=121.69
  ActiveArea-C=93.03
```

1621 *Source Code B.3: Example of slot group as might be found in `Dimensions.ini`. In this example, the file  
 provides information about a detector named `RE2-2-NPD-BARC-8`, having 3 pseudo-rapidity readout partitions  
 and stored in slot `S1` of trolley `T1`. This is a CMS RE2-2 type of detector. This information will then be used for  
 example to compute the rate per unit area calculation.*

1622 This information is readout and stored in a C++ object called `IniFile`, that parses the information  
 1623 in the INI input file and stores it into a local buffer for later use. This INI parser is the exact same  
 1624 one that was previously developed for the Gif++ DAQ and described in Appendix A.5.2.

### 1625 **B.3.2 TDC to RPC link file and Mapping**

1626 The same way the INI dimension file information is stored using `map`, the channel mapping and mask  
 1627 information is stored and accessed through `map`. First of all, the mapping CSV file is organised into  
 1628 3 columns separated by tabulations (and not by commas, as expected for CSV files as it is easier using  
 1629 streams to read tab or space separated data using C++):

1630

1631	RPC_channel	TDC_channel	mask
------	-------------	-------------	------

1632 using as formatting for each field:

1633	TSCCC	TCCC	M
------	-------	------	---

1635 TSCCC is a 5-digit integer where  $\tau$  is the trolley ID,  $s$  the slot ID in which the RPC is held insite  
 1636 the trolley  $\tau$  and ccc is the RPC channel number, or *strip* number, that can take values up to  
 1637 3-digits depending on the detector,

1638 TCCC is a 4 digit integer where  $\tau$  is the TDC ID, ccc is the TDC channel number that can take values  
 1639 in between 0 and 127, and

1640 M is a 1-digit integer indicating if the channel should be considered ( $M = 1$ ) or discarded ( $M = 0$ )  
 1641 during analysis.

1642 This mapping and masking information is readout and stored thanks to the object `Mapping`, pre-  
 1643 sented in Source Code B.4. Similarly to `IniFile` objects, this class has private methods. The first  
 1644 one, `Mapping::CheckIfNewLine()` is used to find the newline character '`\n`' or return character  
 1645 '`\r`' (depending on which kind of operating system interacted with the file). This is used for the  
 1646 simple reason that the masking information has been introduced only during the year 2017 but the  
 1647 channel mapping files exist since 2015 and the very beginning of data taking at GIF++. This means  
 1648 that in the older data folders, before the upgrade, the channel mapping file only had 2 columns, the  
 1649 RPC channel and the TDC channel. For compatibility reasons, this method helps controling the  
 1650 character following the readout of the 2 first fields of a line. In case any end of line character is  
 1651 found, no mask information is present in the file and the default  $M = 1$  is used. On the contrary, if  
 1652 the next character was a tabulation or a space, the mask information is present.

1653 Once the 3 fields have been readout, the second private method `Mapping::CheckIfTDCCh()` is  
 1654 used to control that the TDC channel is an existing TDC channel. Finally, the information is stored  
 1655 into 3 different maps (`Link`, `ReverseLink` and `Mask`) thanks to the public method `Mapping::Read()`.  
 1656 `Link` allows to get the RPC channel by knowing the TDC channel while `ReverseLink` does the op-  
 1657 posite by returning the TDC channel by knowing the RPC channel. Finally, `Mask` returns the mask  
 1658 associated to a given RPC channel.

```

1659 typedef map<Uint,Uint> MappingData;
1660
1661 class Mapping {
1662     private:
1663         bool          CheckIfNewLine(char next);
1664         bool          CheckIfTDCCh(Uint channel);
1665         string        FileName;
1666         MappingData Link;
1667         MappingData ReverseLink;
1668         MappingData Mask;
1669         int           Error;
1670
1671     public:
1672         Mapping();
1673         Mapping(string baseName);
1674         ~Mapping();
1675
1676         void SetFileName(const string filename);
1677         int Read();
1678         Uint GetLink(Uint tdcchannel);
1679         Uint GetReverse(Uint rpcchannel);
1680         Uint GetMask(Uint rpcchannel);
1681     };

```

1661 *Source Code B.4: Description of C++ object Mapping used as a parser for the channel mapping and mask file.*

## 1662 B.4 Description of GIF++ setup within the Offline Analysis tool

1663 In the previous section, the tool input files have been discussed. The dimension file information is  
 1664 stored in a map hosted by the `IniFile` object. But this information is then used to create a series of  
 1665 new objects that helps defining the GIF++ infrastructure directly into the Offline Analysis. Indeed,  
 1666 from the `RPC`, to the more general `Infrastructure`, every element of the GIF++ infrastrucutre is  
 1667 recreated for each data analysis based on the information provided in input. All this information  
 1668 about the infrastructure will be used to assign each hit signal to a specific strip channel of a specific  
 1669 detector, and having a specific active area. This way, rate per unit area calculation is possible.  
 1670

### 1671 B.4.1 RPC objects

1672 `RPC` objects have been developped to represent physical active detectors in GIF++ at the moment  
 1673 of data taking. Thus, there are as many `RPC` objects created during the analysis than there were  
 1674 active `RPC`s tested during a run. Each `RPC` hosts the information present in the corresponding INI  
 1675 slot group, as shown in B.3, and organises it using a similar architecture. This can be seen from  
 1676 Source B.5.

1677 To make the object more compact, the lists of gap labels, of gap active areas and strip active  
 1678 areas are stored into `vector` dynamical containers. `RPC` objects are always contructed thanks to the  
 1679 dimension file information stored into the `IniFILE` and their ID, using the format `TtSs`. Using the  
 1680 `RPC` ID, the constructor calls the methods of `IniFILE` to initialise the `RPC`. The other constructors  
 1681 are not used but exist in case of need. Finally, some getters have been written to access the different  
 1682 private parameters storing the detector information.

```

1683
class RPC{
    private:
        string      name;           //RPC name as in webDCS database
        Uint        nGaps;          //Number of gaps in the RPC
        Uint        nPartitions;    //Number of partitions in the RPC
        Uint        nStrips;         //Number of strips per partition
        vector<string> gaps;       //List of gap labels (BOT, TOP, etc...)
        vector<float>  gapGeo;        //List of gap active areas
        vector<float>  stripGeo;      //List of strip active areas

    public:
        RPC();
        RPC(string ID, IniFile* geofile);
        RPC(const RPC& other);
        ~RPC();
        RPC& operator=(const RPC& other);

        string GetName();
        Uint GetNGaps();
        Uint GetNPartitions();
        Uint GetNStrips();
        string GetGap(Uint g);
        float GetGapGeo(Uint g);
        float GetStripGeo(Uint p);
};

1684
1685  Source Code B.5: Description of C++ objects RPC that describe each active detectors used during data taking.

```

## 1686 B.4.2 Trolley objects

1687 Trolley objects have been developped to represent physical active trolleys in GIFT++ at the moment  
 1688 of data taking. Thus, there are as many trolley objects created during the analysis than there were  
 1689 active trolleys hosting tested RPCs during a run. Each Trolley hosts the information present in the  
 1690 corresponding INI trolley group, as shown in B.2, and organises it using a similar architecture. In  
 1691 addition to the information hosted in the INI file, these object have a dynamical container of RPC  
 1692 objects, representing the active detectors the active trolley was hosting at the time of data taking.  
 1693 This can been seen from Source Code B.6.

1694 Trolley objects are always contructed thanks to the dimension file information stored into the  
 1695 IniFILE and their ID, using the format Tt. Using the Trolley ID, the constructor calls the methods  
 1696 of IniFILE to initialise the Trolley. Retrieving the information of the RPC IDs via SlotsID, a new  
 1697 RPC is constructed and added to the container RPCs for each character in the ID string. The other  
 1698 constructors are not used but exist in case of need. Finally, some getters have been written to access  
 1699 the different private parameters storing the trolley and detectors information.

```

1700
class Trolley{
    private:
        Uint          nSlots; //Number of active RPCs in the considered trolley
        string        SlotsID; //Active RPC IDs written into a string
        vector<RPC*> RPCs;   //List of active RPCs

    public:
        //Constructors, destructor and operator =
        Trolley();
        Trolley(string ID, IniFile* geofile);
        Trolley(const Trolley& other);
        ~Trolley();
        Trolley& operator=(const Trolley& other);

        //Get GIFTrolley members
        Uint  GetNSlots();
        string GetSlotsID();
        Uint   GetSlotID(Uint s);

        //Manage RPC list
        RPC*  GetRPC(Uint r);
        void  DeleteRPC(Uint r);

        //Methods to get members of RPC objects stored in RPCs
        string GetName(Uint r);
        Uint   GetNGaps(Uint r);
        Uint   GetNPartitions(Uint r);
        Uint   GetNStrips(Uint r);
        string GetGap(Uint r, Uint g);
        float  GetGapGeo(Uint r, Uint g);
        float  GetStripGeo(Uint r, Uint p);
    };

```

*Source Code B.6: Description of C++ objects `Trolley` that describe each active trolley used during data taking.*

### 1703    B.4.3 Infrastructure object

1704 The `Infrastructure` object has been developped to represent the GIFT++ bunker area dedicated to  
 1705 CMS RPC experiments. With this very specific object, all the information about the CMS RPC  
 1706 setup within GIFT++ at the moment of data taking is stored. It hosts the information present in the  
 1707 corresponding INI general group, as shown in B.1, and organises it using a similar architecture. In  
 1708 addition to the information hosted in the INI file, this object have a dynamical container of `Trolley`  
 1709 objects, representing the active tolleys in GIFT++ area. This can be seen from Source Code B.7.

1710 The `Infrastructure` object is always contructed thanks to the dimension file information stored  
 1711 into the `IniFILE`. Retrieving the information of the trolley IDs via `TrolleysID`, a new `Trolley` is  
 1712 constructed and added to the container `Trolleys` for each character in the ID `string`. By extension,  
 1713 it is easy to understand that the process described in Section B.4.2 for the construction of RPCs  
 1714 takes place when a trolley is constructed. The other constructors are not used but exist in case of  
 1715 need. Finally, some getters have been written to access the different private parameters storing the  
 1716 infrastructure, tolleys and detectors information.

```

1717
class Infrastructure {
    private:
        Uint             nTrolleys;   //Number of active Trolleys in the run
        string          TrolleysID;  //Active trolley IDs written into a string
        vector<Trolley*> Trolleys;  //List of active Trolleys (struct)

    public:
        //Constructors and destructor
        Infrastructure();
        Infrastructure(IniFile* geofile);
        Infrastructure(const Infrastructure& other);
        ~Infrastructure();
        Infrastructure& operator=(const Infrastructure& other);

        //Get Infrastructure members
        Uint  GetNTrolleys();
        string GetTrolleysID();
        Uint   GetTrolleyID(Uint t);

1718
        //Manage Trolleys
        Trolley* GetTrolley(Uint t);
        void     DeleteTrolley(Uint t);

        //Methods to get members of GIFTrolley objects stored in Trolleys
        Uint  GetNSlots(Uint t);
        string GetSlotsID(Uint t);
        Uint   GetSlotID(Uint t, Uint s);
        RPC*  GetRPC(Uint t, Uint r);

        //Methods to get members of RPC objects stored in RPCs
        string GetName(Uint t, Uint r);
        Uint   GetNGaps(Uint t, Uint r);
        Uint   GetNPartitions(Uint t, Uint r);
        Uint   GetNStrips(Uint t, Uint r);
        string GetGap(Uint t, Uint r, Uint g);
        float  GetGapGeo(Uint t, Uint r, Uint g);
        float  GetStripGeo(Uint t, Uint r, Uint p);
};


```

Source Code B.7: Description of C++ object *Infrastructure* that contains the full information about CMS RPC experiment in GIF++.

## 1720 B.5 Handeling of data

1721 As discussed in Appendix A.4.2, the raw data as a `TTree` architecture where every entry is related to  
 1722 a trigger signal provided by a muon or a random pulse, whether the goal of the data taking was to  
 1723 measure the performance of the detector or the noise/gamma background respectively. Each of these  
 1724 entries, referred also as events, contain a more or less full list of hits in the TDC channels to which  
 1725 the detectors are connected. To this list of hits corresponds a list of time stamps, marking the arrival  
 1726 of the hits within the TDC channel.

1727 The infrastructure of the CMS RPC experiment within GIF++ being defined, combining the  
 1728 information about the raw data with the information provided by both the mapping/mask file and the  
 1729 dimension file allows to build new physical objects that will help in computing efficiency or rates.

### B.5.1 RPC hits

1731 The raw data stored in the ROOT file as output of the GIFT++ DAQ, is readout by the analysis tool  
1732 using the structure `RAWData` presented in Source Code B.9 that differs from the structure presented  
1733 in Appendix A.4.2 as it is not meant to hold all of the data contained in the ROOT file. In this sense,  
1734 this structure is in the case of the offline analysis tool not a dynamical object and will only be storing  
1735 a single event contained in a single entry of the `TTree`.

```

1736
class RPCHit {
    private:
        Uint Channel;           //RPC channel according to mapping (5 digits)
        Uint Trolley;          //0, 1 or 3 (1st digit of the RPC channel)
        Uint Station;           //Slot where is held the RPC in Trolley (2nd digit)
        Uint Strip;             //Physical RPC strip where the hit occurred (last 3
    ↵  digits)
        Uint Partition;         //Readout partition along eta segmentation
        float TimeStamp;        //Time stamp of the arrival in TDC

    public:
        //Constructors, destructor & operator =
        RPCHit();
        RPCHit(Uint channel, float time, Infrastructure* Infra);
        RPCHit(const RPCHit& other);
        ~RPCHit();
        RPCHit& operator=(const RPCHit& other);

        //Get RPCHit members
        Uint GetChannel();
        Uint GetTrolley();
        Uint GetStation();
        Uint GetStrip();
        Uint GetPartition();
        float GetTime();
};

typedef vector<RPCHit> HitList;
typedef struct GIFHitList { HitList rpc[NTROLLEYS][NSLOTS][NPARTITIONS]; }
    ↵  GIFHitList;

bool SortHitbyStrip(RPCHit h1, RPCHit h2);
bool SortHitbyTime(RPCHit h1, RPCHit h2);

```

Source Code B.8: Description of C++ object `RPCHit`.

```
1739 struct RAWData{  
    int iEvent; //Event i  
    int TDCNHits; //Number of hits in event i  
    int QFlag; //Quality flag list (1 flag digit per TDC)  
    vector<UInt> *TDCCh; //List of channels giving hits per event  
    vector<float> *TDCTS; //List of the corresponding time stamps  
};
```

*Source Code B.9: Description of C++ structure RAWData.*

1741 Each member of the structure is then linked to the corresponding branch of the ROOT data tree,  
1742 as shown in the example of Source Code B.10, and using the method `GetEntry(int i)` of the ROOT  
1743 class `TTree` will update the state of the members of `RAWData`.

```

1744 TTree* dataTree = (TTree*)dataFile.Get("RAWData");
1745 RAWData data;
1746
1747 dataTree->SetBranchAddress("EventNumber", &data.iEvent);
1748 dataTree->SetBranchAddress("number_of_hits", &data.TDCNHits);
1749 dataTree->SetBranchAddress("Quality_flag", &data.QFlag);
1750 dataTree->SetBranchAddress("TDC_channel", &data.TDCCh);
1751 dataTree->SetBranchAddress("TDC_TimeStamp", &data.TDCTS);

```

1746       *Source Code B.10: Example of link in between RAWData and TTree.*

1747       The data is then analysed entry by entry and to each element of the TDC channel list, a `RPCHit` is  
1748       constructed by linking each TDC channel to the corresponding RPC channel thanks to the `Mapping`  
1749       object. The information carried by the RPC channel format allows to easily retrieve the trolley and  
1750       slot from which the hit was recorded (see section B.3.2). Using these 2 values, the readout partition  
1751       can be found by knowing the strip channel and comparing it with the number of partitions and strips  
1752       per partition stored into the `Infrastructure` object.

1753       Thus `RPCHit` objects are then stored into 3D dynamical list called `GIFHitList` (Source Code B.9)  
1754       where the 3 dimensions refer to the 3 layers of the readout in `GIF++` : in the bunker there are *trolleys*  
1755       ( $\tau$ ) holding detectors in *slots* ( $s$ ) and each detector readout is divided into 1 or more pseudo-rapidity  
1756       *partitions* ( $p$ ). Using these 3 information allows to assign an address to each readout partition and  
1757       this address will point to a specific hit list.

1758

## 1759       **B.5.2 Clusters of hits**

1760       All the hits contained in the ROOT file have been sorted into the different hit lists through the  
1761       `GIFHitList`. At this point, it is possible to start looking for clusters. A cluster is a group of adjacent  
1762       strips getting hits within a time window of 25 ns. These strips are then assumed to be part of the same  
1763       physical avalanche signal generated by a muon passing through the chamber or by the interaction of  
1764       a gamma stopping into the electrodes of the RPCs.

1765       To keep the cluster information, `RPCCluster` objects have been defined as shown in Source  
1766       Code B.11. Using the information of each individual `RPCHit` taken out of the hit list, it stores  
1767       the cluster size (number of adjacent strips composing the cluster), the first and last hit, the center for  
1768       spatial reconstruction and finally the start and stop time stamps as well as the time spread in between  
1769       the first and last hit.

```

1770 class RPCCluster{
    private:
        Uint ClusterSize; //Size of cluster #ID
        Uint FirstStrip; //First strip of cluster #ID
        Uint LastStrip; //Last strip of cluster #ID
        float Center; //Center of cluster #ID ((first+last)/2)
        float StartStamp; //Time stamp of the earliest hit of cluster #ID
        float StopStamp; //Time stamp of the latest hit of cluster #ID
        float TimeSpread; //Time difference between earliest and latest hits
                           //of cluster #ID

    public:
        //Constructors, destructor & operator =
        RPCCluster();
        RPCCluster(HitList List, Uint cID, Uint cSize, Uint first, Uint firstID);
        RPCCluster(const RPCCluster& other);
        ~RPCCluster();
        RPCCluster& operator=(const RPCCluster& other);

        //Get Cluster members
        Uint GetID();
        Uint GetSize();
        Uint GetFirstStrip();
        Uint GetLastStrip();
        float GetCenter();
        float GetStart();
        float GetStop();
        float GetSpread();
    };

typedef vector<RPCCluster> ClusterList;

//Other functions to build cluster lists out of hit lists
void BuildClusters(HitList &cluster, ClusterList &clusterList);
void Clusterization(HitList &hits, TH1 *hcSize, TH1 *hcMult);

```

1772 Source Code B.11: Description of C++ object cluster.

To investigate the hit list of a given detector partition, the function `Clusterization()` defined in `include/Cluster.h` needs the hits in the list to be time sorted. This is achieved by calling function `sort()` of library `<algorithm>` using the comparator `SortHitbyTime(RPCHit h1, RPCHit h2)` defined in `include/RPCHit.h` that returns `true` if the time stamp of hit `h1` is lower than that of `h2`. A first isolation of strips is made only based on time information. All the hits within the 25 ns window are taken separately from the rest. Then, this sub-list of hits is sorted this time by ascending strip number, using this time the comparator `SortHitbyStrip(RPCHit h1, RPCHit h2)`. Finally, the groups of adjacent strips are used to construct `RPCCluster` objects that are then stored in a temporary list of clusters that is at the end of the process used to know how many clusters were reconstructed and to fill their sizes into an histogram that will allows to know the mean size of muon or gamma clusters.

1785 B.6 DAQ data Analysis

1786 All the ingredients to analyse GIF++ data have been defined. This section will focus on the different  
1787 part of the analysis performed on the data, from determining the type of data the tool is dealing with

1788 to calculating the rate in each detector or reconstructing muon or gamma clusters.

### 1789 B.6.1 Determination of the run type

1790 In GIF++, both the performance of the detectors in detecting muons in an irradiated environment and  
1791 the gamma background can be independantly measured. These corresponds to different run types  
1792 and thus, to different TDC settings giving different data to look at.

1793

1794 In the case of performance measurements, the trigger for data taking is provided by the coïncidence  
1795 of several scintillators when muons from the beam passing through the area are detected. Data  
1796 is collected in a 600 ns wide window around the arrival of muons in the RPCs. The expected time  
1797 distribution of hits is shown in Figure B.1a. The muon peak is clearly visible in the center of the  
1798 distribution and is to be extracted from the gamma background that composes the flat part of the  
1799 distribution.

1800 On the other hand, gamma background or noise measurements are focussed on the non muon  
1801 related physics and the trigger needs to be independant from the muons to give a good measurement  
1802 of the gamma/noise distribution as seen by the detectors. The trigger is then provided by a pulse  
1803 generator at a frequency of 300 Hz whose pulse is not likely to be on time with a muon. In order  
1804 to increase the integrated time without increasing the acquisition time too much, the width of the  
1805 acquisition windows are increased to 10  $\mu$ s. The time distribution of the hits is expected to be flat, as  
1806 shown by Figure B.1b.

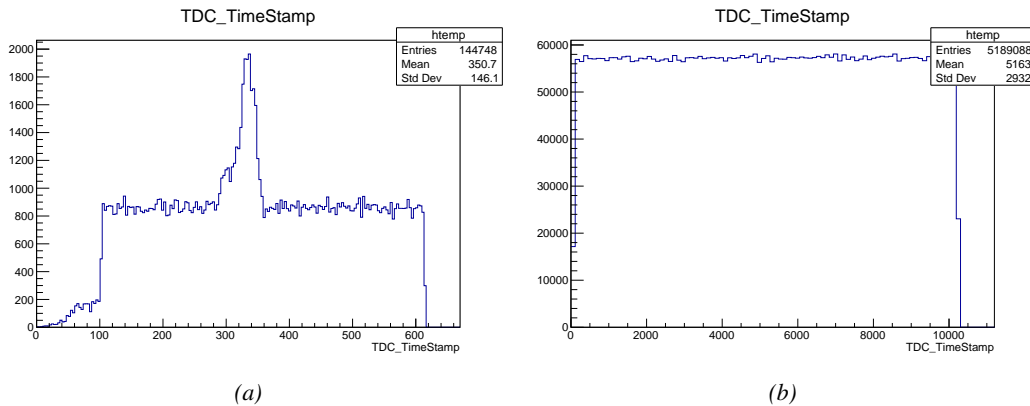


*Figure B.1: Example of expected hit time distributions in the cases of efficiency (Figure B.1a) and noise/gamma rate per unit area (Figure B.1b) measurements as extracted from the raw ROOT files. The unit along the x-axis corresponds to ns. The fact that "the" muon peak is not well defined in Figure B.1a is due to the contribution of all the RPCs being tested at the same time that don't necessarily have the same signal arrival time. Each individual peak can have an offset with the ones of other detectors. The inconsistency in the first 100 ns of both time distributions is an artefact of the TDCs and are systematically rejected during the analysis.*

1807 The ROOT files include a TTree called RunParameters containing, among other things, the in-  
1808 formation related to the type of run. The run type can then be accessed as described by Source  
1809 Code B.12 and the function IsEfficiencyRun() is then used to determine if the run file is an effi-  
1810 ciency run or, on the contrary, another type of run (noise or gamma measurement).

```

1811     TTree* RunParameters = (TTree*)dataFile.Get("RunParameters");
1812     TString* RunType = new TString();
1813     RunParameters->SetBranchAddress("RunType", &RunType);
1814     RunParameters->GetEntry(0);

```

1813       *Source Code B.12: Access to the run type contained in TTree\* RunParameters.*

1814       Finally, the data files will have a slightly different content whether it was collected before or after  
 1815       October 2017 and the upgrade of the DAQ software that brought a new information into the ROOT  
 1816       output. This is discussed in Appendix A.4.3 and implies that the analysis will differ a little depending  
 1817       on the data format. Indeed, as no information on the data quality is stored, in older data files, the cor-  
 1818       rections for missing events has to be done at the end of the analysis. The information about the type  
 1819       of data format is stored in the variable **bool** `isNewFormat` by checking the list of branches contained  
 1820       in the data tree via the methods `TTree::GetListOfBranches()` and `TCollection::Contains()`.

## 1821       **B.6.2 Beam time window calculation for efficiency runs**

1822       Knowing the run type is important first of all to know the width of the acquisition window to be used  
 1823       for the rate calculation and finally to be able to seek for muons. Indeed, the peak that appears in the  
 1824       time distribution for each detectors is then fitted to extract the most probable time window in which  
 1825       the tool should look for muon hits. The data outside of this time window is then used to evaluate the  
 1826       noise or gamma background the detector was subjected to during the data taking. Computing the  
 1827       position of the peak is done calling the function `SetBeamWindow()` defined in file `src/RPCHit.cc` that  
 1828       loops a first time on the data. The data is first sorted in a 3D array of 1D histograms (`GIFH1Array`, see  
 1829       `include/types.h`). Then the location of the highest bin is determined using `TH1::GetMaximumBin()`  
 1830       and is used to define a window in which a gaussian fit will be applied to compute the peak width.  
 1831       This window is a 80 ns defined by Formula B.1 around the central bin.

$$t_{center}(ns) = bin \times width_{bin}(ns) \quad (\text{B.1a})$$

$$[t_{low}; t_{high}] = [t_{center} - 40; t_{center} + 40] \quad (\text{B.1b})$$

1832       Before the fit is performed, the average number of noise/gamma hits per bin is evaluated using  
 1833       the data outside of the fit window. Excluding the first 100 ns, the average number of hits per bin  
 1834       due to the noise or gamma is defined by Formula B.2 after extracting the amount of hits in the time  
 1835       windows  $[100; t_{low}]$  and  $[t_{high}; 600]$  thanks to the method `TH1::Integral()`. This average number  
 1836       of hits is then subtracted to every bin of the 1D histogram, in order to *clean* it from the noise or  
 1837       gamma contribution as much as possible to improve the fit quality. Bins where  $\langle n_{hits} \rangle$  is greater  
 1838       than the actual bin content are set to 0.

$$\Delta t_{noise}(ns) = 600 \overbrace{-t_{high} + t_{low}}^{-80ns} - 100 = 420ns \quad (\text{B.2a})$$

$$\langle n_{hits} \rangle = width_{bin}(ns) \times \frac{\sum_{t=100}^{t_{low}} + \sum_{t=t_{high}}^{600}}{\Delta t_{noise}(ns)} \quad (\text{B.2b})$$

1839       Finally, the fit parameters are extracted and saved for each detector in 3D arrays of **float**  
 1840       (`muonPeak`, see `include/types.h`), a first one for the mean arrival time of the muons, `PeakTime`,

1841 and a second one for the width of the peak, `PeakWidth`. The width is defined as  $6\sigma$  of the gaussian  
 1842 fit. The same settings are applied to every partitions of the same detector. To determine which one  
 1843 of the detector's partitions is directly illuminated by the beam, the peak height of each partition is  
 1844 compared and the highest one is then used to define the peak settings.

### 1845 **B.6.3 Data loop and histogram filling**

1846 3D arrays of histogram are created to store the data and display it on the DQM of G4F++ webDCS  
 1847 for the use of shifters. These histograms, presented in section B.2.1.1, are filled while looping on  
 1848 the data. Before starting the analysis loop, it is necessary to control the entry quality for the new  
 1849 file formats featuring `QFlag`. If the `QFlag` value for this entry shows that 1 TDC or more have a  
 1850 CORRUPTED flag, then this event is discarded. The loss of statistics is low enough to be neglected.  
 1851 `QFlag` is controlled using the function `IsCorruptedEvent()` defined in `src/utils.cc`. As explained  
 1852 in Appendix A.4.3, each digit of this integer represent a TDC flag that can be 1 or 2. Each 2 is  
 1853 the sign of a CORRUPTED state. Then, the data is accessed entry by entry in the ROOT `TTree` using  
 1854 `RAWData` and each hit in the hit list is assigned to a detector channel and saved in the corresponding  
 1855 histograms. In the first part of the analysis, in which the loop over the ROOT file's content is  
 1856 performed, the different steps are:

1857 **1- RPC channel assignment and control:** a check is done on the RPC channel extracted thanks  
 1858 to the mapping via the method `Mapping::GetLink()`. If the channel is not initialised and is 0, or if  
 1859 the TDC channel was greater than 5127, the hit is discarded. This means there was a problem in the  
 1860 mapping. Often a mapping problem leads to the crash of the offline tool.

1861 **2- Creation of a `RPCHit` object:** to easily get the trolley, slot and partition in which the hit has  
 1862 been assigned, this object is particularly helpful.

1863 **3- General histograms are filled:** the hit is filled into the time distribution and the general hit  
 1864 distribution histograms, and if the arrival time is within the first 100 ns, it is discarded and nothing  
 1865 else happens and the loop proceeds with the next hit in the list.

1866 **4- Multiplicity counter:** the hit multiplicity counter of the corresponding detectors incremented.

1867 **5-a- Efficiency runs - Is the hit within the peak window? :** if the peak is contained in the peak  
 1868 window previously defined in section B.6.2, the hit is filled into the beam hit profile histogram of  
 1869 the corresponding chamber, added into the list of muon hits and increments the counter of *in time*  
 1870 hits. The term *in time* here refers to the hits that are likely to be muons by arriving in the expected  
 1871 time window. If the hit is outside of the peak window, it is filled into the noise profile histogram  
 1872 of the corresponding detector, added into the list of noise/gamma hits and increments the counter of  
 1873 noise/gamma hits.

1874 **5-b- Noise/gamma rate runs - Noise histograms are filled:** the hit is filled into the noise profile  
 1875 histogram of the corresponding detector, added into the list of noise/gamma hits and increments the  
 1876 counter of noise/gamma hits.

1877

1878 After the loop on the hit list of the entry is over, the next step is to clusterize the 3D lists filled  
 1879 in the previous steps. A 3D loop is then started over the active trolley, slot and RPC partitions to  
 1880 access these objects. Each `NoiseHitList` and `MuonHitList`, in case of efficiency run, are clusterized  
 1881 as described in section B.5.2. There corresponding cluster size and multiplicity histograms are filled  
 1882 at the end of the clustering process. Then, the efficiency histogram is filled in case of efficiency run.  
 1883 The selection is simply made by checking whether the RPC detected signals in the peak window  
 1884 during this event. Nevertheless, it is useful to highlight that at this level, it is not possible yet to  
 1885 discriminate in between a muon hit and noise or gamma hit. Thus, `MuonCSize_H`, `MuonCMult_H`  
 1886 and `Efficiency0_H` are subjected to noise and gamma contamination. This contamination will be  
 1887 estimated and corrected at the moment the results will be written into output CSV files. Finally, the  
 1888 loop ends on the filling of the general hit multiplicity histogram.

#### 1889 **B.6.4 Results calculation**

1890 As mentioned in section B.2.1, the analysis of DAQ data provides the user with 3 CSV files and  
 1891 a ROOT file associated to each and every ROOT data file. The fourth CSV file is provided by the  
 1892 extraction of the CEAN main frame data monitored during data taking and will be discussed later.  
 1893 After looping on the data in the previous part of the analysis macro, the output files are created and a  
 1894 3D loop on each RPC readout partitions is started to extract the histograms parameters and compute  
 1895 the final results.

1896

##### 1897 **B.6.4.1 Rate normalisation**

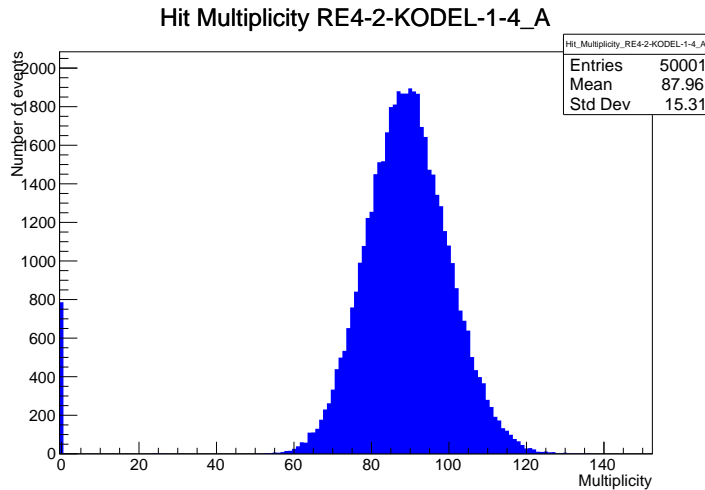


Figure B.2: The effect of the quality flag is explained by presenting the reconstructed hit multiplicity of a data file without `Quality_flag`. The artificial high content of bin 0 is the effect of corrupted data.

1898 To analyse old data format files, not containing any quality flag, it is needed to estimate the amount  
 1899 of corrupted data via a fit as the corrupted data will always fill events with a fake "0 multiplicity".  
 1900 Indeed, as no hits were stored in the DAQ ROOT files, these events artificially contribute to fill  
 1901 the bin corresponding to a null multiplicity, as shown in Figure B.2. In the case the mean of the

hit multiplicity distribution is high, the contribution of the corrupted data can easily be evaluated for later correction by comparing the level of the bin at multiplicity 0 and of a skew fit curve that should indicate a value consistent with 0. A skew fit has been chosen over a Poisson fit as it was giving better results for lower mean multiplicity values. Nevertheless, for low irradiation cases, as explained in Appendix A.4.3, the hit multiplicity distribution mean is, on the contrary, rather small and the probability to record events without hits can't be considered small anymore, leading to a difficult and non-reliable estimation of the corruption. As can be seen in Source Code B.13, conditions have been applied to prevent bad fits and wrong corruption estimation in cases where :

- The difference in between the data for multiplicity 1 and the corresponding fit value should be lower than 1% of the total amount of data :  $\frac{|n_{m=1} - sk(1)|}{N_{tot}} < 0.01$  where  $n_{m=1}$  is the number of entries with multiplicity 1,  $sk(1)$  the value of the skew fit, as defined by Formula 4.3, for multiplicity 1 and  $N_{tot}$  the total number of entries.

- The amount of data contained in the multiplicity 0 bin should not exceed 40% :  $\frac{n_{m=0}}{N_{tot}} \leq 0.4$  where  $n_{m=0}$  is the number of entries with multiplicity 0. This number has been determined to be the maximum to be able to separate the excess of data due to corruption from the hit multiplicity distribution.

Those 2 conditions need to be fulfilled to estimate the corruption of old data format files. If the fit was successful, the level of corruption is written in `Offline-Corrupted.csv` and the number of corrupted entries, refered as the integer `nEmptyEvent`, is subtracted from the total number of entries when the rate normalisation factor is computed as explicit in Source Code B.13. Note that for new data format files, the number of corrupted entries being set to 0, the definition of `rate_norm` stays valid.

```

1924 if(!isNewFormat) {
    TF1* GaussFit = new TF1("gaussfit","[0]*exp(-0.5*((x-[1])/[2])**2)",0,Xmax);
    GaussFit->SetParameter(0,100);
    GaussFit->SetParameter(1,10);
    GaussFit->SetParameter(2,1);
    HitMultiplicity_H.rpc[T][S][p]->Fit(GaussFit,"LIQR","",0.5,Xmax);

    TF1* SkewFit = new TF1("skewfit","[0]*exp(-0.5*((x-[1])/[2])**2) / (1 +
→   exp(-[3]*(x-[4])))",0,Xmax);
    SkewFit->SetParameter(0,GaussFit->GetParameter(0));
    SkewFit->SetParameter(1,GaussFit->GetParameter(1));
    SkewFit->SetParameter(2,GaussFit->GetParameter(2));
    SkewFit->SetParameter(3,1);
    SkewFit->SetParameter(4,1);
    HitMultiplicity_H.rpc[T][S][p]->Fit(SkewFit,"LIQR","",0.5,Xmax);

    double fitValue = SkewFit->Eval(1,0,0,0);
    double dataValue = (double)HitMultiplicity_H.rpc[T][S][p]->GetBinContent(2);
    double difference = TMath::Abs(dataValue - fitValue);
    double fitTOdataVSentries_ratio = difference / (double)nEntries;
    bool isFitGOOD = fitTOdataVSentries_ratio < 0.01;

    double nSinglehit = (double)HitMultiplicity_H.rpc[T][S][p]->GetBinContent(1);
    double lowMultRatio = nSinglehit / (double)nEntries;
    bool isMultLOW = lowMultRatio > 0.4;

    if(isFitGOOD && !isMultLOW){
        nEmptyEvent = HitMultiplicity_H.rpc[T][S][p]->GetBinContent(1);
        nPhysics = (int)SkewFit->Eval(0,0,0,0);
        if(nPhysics < nEmptyEvent)
            nEmptyEvent = nEmptyEvent-nPhysics;
    }
}

double corrupt_ratio = 100.* (double)nEmptyEvent / (double)nEntries;
outputCorrCSV << corrupt_ratio << '\t';

float rate_norm = 0.;
float stripArea = GIFIstra->GetStripGeo(tr,sl,p);

if(IsEfficiencyRun(RunType)) {
    float noiseWindow = BMTDCWINDOW - TIMEREJECT - 2*PeakWidth.rpc[T][S][p];
    rate_norm = (nEntries-nEmptyEvent)*noiseWindow*1e-9*stripArea;
} else
    rate_norm = (nEntries-nEmptyEvent)*RDMNOISEWDW*1e-9*stripArea;

```

*Source Code B.13: Definition of the rate normalisation variable. It takes into account the number of non corrupted entries and the time window used for noise calculation, to estimate the total integrated time, and the strip active area to express the result as rate per unit area.*

#### B.6.4.2 Rate and activity

1928 At this point, the strip rate histograms, `StripNoiseProfile_H.rpc[T][S][p]`, only contain an in-  
1929 formation about the total number of noise or rate hits each channel received during the data taking.  
1930 As described in Source Code B.14, a loop on the strip channels will be used to normalise the content  
1931 of the rate distribution histogram for each detector partitions. The initial number of hits recorded for  
1932 a given bin will be extracted and 2 values will be computed:

- 1933     ● the strip rate, defined as the number of hits recorded in the bin normalised like described in  
 1934               the previous section, using the variable `rate_norm`, and

- 1935     ● the strip activity, defined as the number of hits recorded in the bin normalised to the average  
 1936               number of hits per bin contained in the partition histogram, using the variable `averageNhit`.  
 1937               This value provides an information on the homogeneity of the detector response to the gamma  
 1938               background or of the detector noise. An activity of 1 corresponds to an average response.  
 1939               Above 1, the channel is more active than the average and bellow 1, the channel is less active.

```

int nNoise = StripNoiseProfile_H.rpc[T][S][p]->GetEntries();
float averageNhit = (nNoise>0) ? (float)(nNoise/nStripsPart) : 1.;

for(Uint st = 1; st <= nStripsPart; st++) {
    float stripRate =
        StripNoiseProfile_H.rpc[T][S][p]->GetBinContent(st)/rate_norm;
    float stripAct =
        StripNoiseProfile_H.rpc[T][S][p]->GetBinContent(st)/averageNhit;

    StripNoiseProfile_H.rpc[T][S][p]->SetBinContent(st,stripRate);
    StripActivity_H.rpc[T][S][p]->SetBinContent(st,stripAct);
}
  
```

1941     *Source Code B.14: Description of the loop that allows to set the content of each strip rate and strip activity  
 channel for each detector partition.*

1942     On each detector partitions, which are readout by a single FEE, all the channels are not processed  
 1943       by the same chip. Each chip can give a different noise response and thus, histograms using a chip  
 1944       binning are used to investigate chip related noise behaviours. The average values of the strip rate  
 1945       or activity grouped into a given chip are extracted using the using the function `GetChipBin()` and  
 1946       stored in dedicated histograms as described in Source Codes B.15 and B.16 respectively.

```

float GetChipBin(TH1* H, Uint chip){
    Uint start = 1 + chip*NSTRIPSCHIP;
    int nActive = NSTRIPSCHIP;
    float mean = 0.;

    for(Uint b = start; b <= (chip+1)*NSTRIPSCHIP; b++) {
        float value = H->GetBinContent(b);
        mean += value;
        if(value == 0.) nActive--;
    }

    if(nActive != 0) mean /= (float)nActive;
    else mean = 0.;

    return mean;
}
  
```

1949     *Source Code B.15: Function used to compute the content of a bin for an histogram using chip binning.*

```

1950   for(UInt ch = 0; ch < (nStripsPart/NSTRIPSCHIP); ch++) {
1951       ChipMeanNoiseProf_H.rpc[T][S][p]->
1952           SetBinContent(ch+1,GetChipBin(StripNoiseProfile_H.rpc[T][S][p],ch));
1953       ChipActivity_H.rpc[T][S][p]->
1954           SetBinContent(ch+1,GetChipBin(StripActivity_H.rpc[T][S][p],ch));
1955   }

```

*Source Code B.16: Description of the loop that allows to set the content of each chip rate and chip activity bins for each detector partition knowing the information contained in the corresponding strip distribution histograms.*

The activity variable is used to evaluate the homogeneity of the detector response to background or of the detector noise. The homogeneity  $h_p$  of each detector partition can be evaluated using the formula  $h_p = \exp(-\sigma_p^R / \langle R \rangle_p)$ , where  $\langle R \rangle_p$  is the partition mean rate and  $\sigma_p^R$  is the rate standard deviation calculated over the partition channels. The more homogeneously the rates are distributed and the smaller will  $\sigma_p^R$  be, and the closer to 1 will  $h_p$  get. On the contrary, if the standard deviation of the channel's rates is large,  $h_p$  will rapidly get to 0. This value is saved into histograms as shown in Source Code B.17 and could in the future be used to monitor through time, once extracted, the evolution of every partition homogeneity. This could be of great help to understand the apparition of eventual hot spots due to ageing of the chambers subjected to high radiation levels. The monitored homogeneity information could then be combined with a monitoring of the activity of each individual channel in order to have a finer information. Monitoring tools have been suggested and need to be developed for this purpose.

```

1964   float MeanPartSDev = GetTH1StdDev(StripNoiseProfile_H.rpc[T][S][p]);
1965   float strip_homog = (MeanPartRate==0)
1966       ? 0.
1967       : exp(-MeanPartSDev/MeanPartRate);
1968   StripHomogeneity_H.rpc[T][S][p]->Fill("exp -#left(#frac{\#sigma_{Strip}
1969       \rightarrow Rate}{\#mu_{Strip Rate}}\#right)",strip_homog);
1970   StripHomogeneity_H.rpc[T][S][p]->GetYaxis()->SetRangeUser(0.,1.);
1971
1972   float ChipStDevMean = GetTH1StdDev(ChipMeanNoiseProf_H.rpc[T][S][p]);
1973   float chip_homog = (MeanPartRate==0)
1974       ? 0.
1975       : exp(-ChipStDevMean/MeanPartRate);
1976   ChipHomogeneity_H.rpc[T][S][p]->Fill("exp -#left(#frac{\#sigma_{Chip}
1977       \rightarrow Rate}{\#mu_{Chip Rate}}\#right)",chip_homog);
1978   ChipHomogeneity_H.rpc[T][S][p]->GetYaxis()->SetRangeUser(0.,1.);

```

*Source Code B.17: Storage of the homogeneity into dedicated histograms.*

### B.6.4.3 Strip masking tool

The offline tool is automatically called at the end of each data taking to analyse the data and offer the shifter DQM histograms to control the data quality. After the histograms have been published online in the DQM page, the shifter can decide to mask noisy or dead channels that will contribute to bias the final rate calculation by editing the mask column of `ChannelsMapping.csv` as can be seen in Figure B.3.

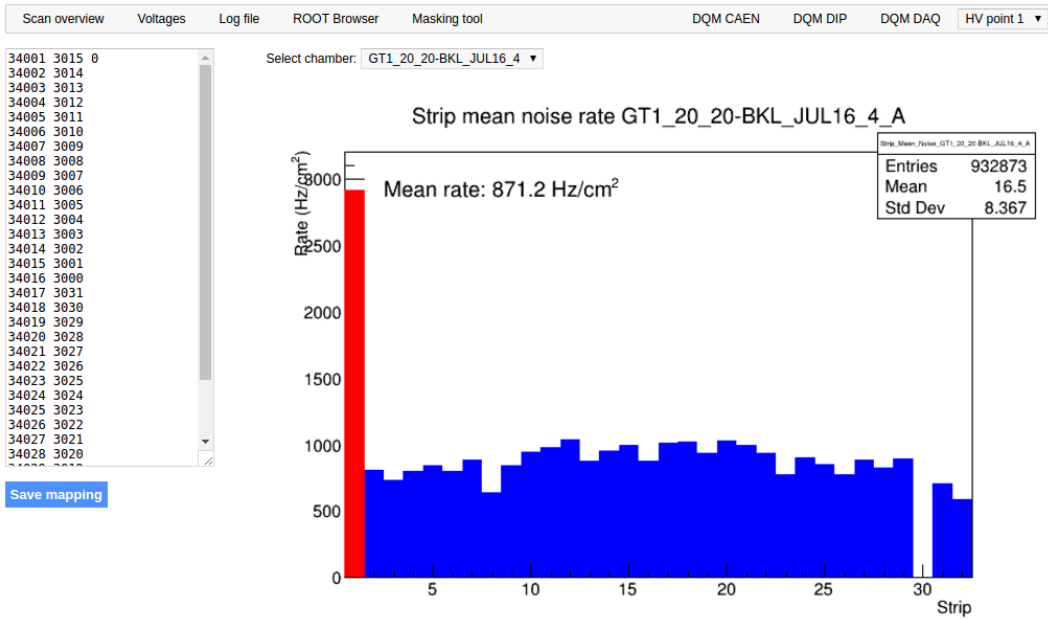


*Figure B.3: Display of the masking tool page on the webDCS. The window on the left allows the shifter to edit ChannelsMapping.csv. To mask a channel, it only is needed to set the 3rd field corresponding to the strip to mask to 0. It is not necessary for older mapping file formats to add a 1 for each strip that is not masked as the code is versatile and the default behaviour is to consider missing mask fields as active strips. The effect of the mask is directly visible for noisy channels as the corresponding bin turns red. The global effect of masking strips will be an update of the rate value showed on the histogram that will take into consideration the rejected channels.*

1973        From the code point of view, the function `GetTH1Mean()` is used to retrieve the mean rate par-  
 1974        tition by partition after the rates have been calculated strip by strip and filled into the histograms  
 1975        `StripNoiseProfile_H.rpc[T][S][p]`, as described through Source Code B.18.

1976        Once the mask for each rejected channel has been updated, the shifter can manually run the of-  
 1977        fline tool again to update the DQM plots, now including the masked strips, as well the rate results  
 1978        written in the output CSV file `Offline-Rate.csv`. If not done during the shifts, the strip masking  
 1979        procedure needs to be carefully done by the person in charge of data analysis on the scans that were  
 1980        selected to produce the final results.

```

1981   float GetTH1Mean(TH1* H) {
1982     int nBins = H->GetNbinsX();
1983     int nActive = nBins;
1984     float mean = 0.;
1985
1986     for(int b = 1; b <= nBins; b++) {
1987       float value = H->GetBinContent(b);
1988       mean += value;
1989       if(value == 0.) nActive--;
1990     }
1991
1992     if(nActive != 0) mean /= (float)nActive;
1993     else mean = 0.;
1994
1995     return mean;
1996   }

```

*Source Code B.18: The function `GetTH1Mean()` is used to return the mean along the y-axis of `TH1` histograms containing rate information. In order to take into account masked strips whose rate is set to 0, the function looks for masked channels and decrement the number of active channels for each null value found.*

#### 1984 B.6.4.4 Output CSV files filling

1985 All the histograms have been filled. Parameters will then be extracted from them to compute the  
 1986 final results that will later be used to produce plots. Once the results have been computed, the very  
 1987 last step of the offline macro is to write these values into the corresponding CSV outputs. Aside of  
 1988 the file `Offline-Corrupted.csv`, 2 CSV files are being written by the macro `offlineAnalysis()`,  
 1989 `Offline-Rates.csv` and `Offline-L0-EffCl.csv` that respectively contain information about noise  
 1990 or gamma rates, cluster size and multiplicity, and about level 0 reconstruction of the detector effi-  
 1991 ciency, muon cluster size and multiplicity. Details on the computation and file writing are respec-  
 1992 tively given in Sources Codes B.19 and B.20.

1993 **Noise/gamma background variables** are computed and written in the output file for each detector  
 1994 partitions. A detector average of the hit and cluster rate is also provided, as shown through Sources  
 1995 Code B.19. The variables that are written for each partition are:

- 1996 • The mean partition hit rate per unit area, `MeanPartRate`, that is extracted from the histogram  
   1997 `StripNoiseProfile_H` as the mean value along the y-axis, as described in section B.6.4.3. No  
   1998 error is recorded for the hit rate as this is considered a single measurement. No statistical error  
   1999 can be associated to it and the systematics are unknown.
- 2000 • The mean cluster size, `cSizePart`, is extracted from the histogram `NoiseCSize_H` and it's  
   2001 statistical error, `cSizePartErr`, is taken to be  $2\sigma$  of the total distribution.
- 2002 • The mean cluster multiplicity per trigger, `cMultPart`, is extracted from the histogram `NoiseCMult_H`  
   2003 and it's statistical error, `cMultPartErr`, is taken to be  $2\sigma$  of the total distribution. It is impor-  
   2004 tant to point to the fact that this variable gives an information that is dependent on the buffer  
   2005 window width used for each trigger for the calculation.
- 2006 • The mean cluster rate per unit area, `ClustPartRate`, is defined as the mean hit rate normalised

2007 to the mean cluster size and it's statistical error, `ClustPartRateErr`, is then obtained using the  
2008 relative statistical error on the mean cluster size.

```

for (UInt tr = 0; tr < GIFInfra->GetNTrolleys(); tr++){
    UInt T = GIFInfra->GetTrolleyID(tr);

    for (UInt sl = 0; sl < GIFInfra->GetNSlots(tr); sl++){
        UInt S = GIFInfra->GetSlotID(tr,sl) - 1;

        float MeanNoiseRate = 0.;
        float ClusterRate = 0.;
        float ClusterSDev = 0.;

        for (UInt p = 0; p < GIFInfra->GetNPartitions(tr,sl); p++){
            float MeanPartRate = GetTH1Mean(StripNoiseProfile_H.rpc[T][S][p]);
            float cSizePart = NoiseCSIZE_H.rpc[T][S][p]->GetMean();
            float cSizePartErr = (NoiseCSIZE_H.rpc[T][S][p]->GetEntries()==0)
                ? 0.
                : 2*NoiseCSIZE_H.rpc[T][S][p]->GetStdDev() /
                    sqrt(NoiseCSIZE_H.rpc[T][S][p]->GetEntries());
            float cMultPart = NoiseCMult_H.rpc[T][S][p]->GetMean();
            float cMultPartErr = (NoiseCMult_H.rpc[T][S][p]->GetEntries()==0)
                ? 0.
                : 2*NoiseCMult_H.rpc[T][S][p]->GetStdDev() /
                    sqrt(NoiseCMult_H.rpc[T][S][p]->GetEntries());
            float ClustPartRate = (cSizePart==0) ? 0.
                : MeanPartRate/cSizePart;
            float ClustPartRateErr = (cSizePart==0) ? 0.
                : ClustPartRate * cSizePartErr/cSizePart;

            outputRateCSV << MeanPartRate << '\t'
                << cSizePart << '\t' << cSizePartErr << '\t'
                << cMultPart << '\t' << cMultPartErr << '\t'
                << ClustPartRate << '\t' << ClustPartRateErr << '\t';

            RPCarea += stripArea * nStripsPart;
            MeanNoiseRate += MeanPartRate * stripArea * nStripsPart;
            ClusterRate += ClustPartRate * stripArea * nStripsPart;
            ClusterSDev += (cSizePart==0)
                ? 0.
                : ClusterRate*cSizePartErr/cSizePart;
        }

        MeanNoiseRate /= RPCarea;
        ClusterRate /= RPCarea;
        ClusterSDev /= RPCarea;

        outputRateCSV << MeanNoiseRate << '\t'
            << ClusterRate << '\t' << ClusterSDev << '\t';
    }
}

```

2010 *Source Code B.19: Description of rate result calculation and writing into the CSV output Offline-Rate.csv.  
2011 Are saved into the file for each detector, the mean partition rate, cluster size and cluster multiplicity, along with  
2012 their errors, for each partition and as well as a detector average.*

2011 **Muon performance variables** are computed and written in the output file for each detector parti-  
2012 tions as shown through Sources Code B.20. The variables that are written for each partition are:

- 2013     • The muon efficiency, `eff`, extracted from the histogram `Efficiency0_H`. It is reminded that  
2014        this offline tool doesn't include any tracking algorithm to identify muons from the beam and  
2015        only relies on the hits arriving in the time window corresponding to the beam time. The con-  
2016        tent of the efficiency histogram is thus biased by the noise/gamma background contribution  
2017        into this window and is thus corrected by estimating the muon data content in the peak re-  
2018        gion knowing the noise/gamma content in the rate calculation region. Both time windows  
2019        being different, the choice was made to normalise the noise/gamma background calculation  
2020        window to it's equivalent beam window in order to have comparable values using the variable  
2021        `windowRatio`. Finally, to estimate the data ratio in the peak region, the variable `DataRatio`  
2022        is defined as the ratio in between the estimated mean cluster multiplicity of the muons in the  
2023        peak region, `MuonCM`, and of the total mean cluster multiplicity in the peak region, `PeakCM`.  
2024        `MuonCM` is itself defined as the difference in between the total mean cluster multiplicity in the  
2025        peak region and the normalised mean noise/gamma cluster multiplicity calculated outside of  
2026        the peak region. The statistical error related to the efficiency, `eff_err`, is computed using a  
2027        binomial distribution, as the efficiency measure the probability of "success" and "failure" to  
2028        detect muons.
- 2029     • The mean muon cluster size, `MuonCS`, is calculated using the total mean cluster size and multi-  
2030        plicity in the peak region, respectively extracted from histograms `MuonCSize_H` and `MuonCMult_H`,  
2031        the noise/gamma background mean cluster size and normalised multiplicity, extracted from  
2032        `NoiseCSize_H` and `NoiseCMult_H`, and of the estimated muon cluster multiplicity `MuonCM` pre-  
2033        viously explicated. The associated statistical error, `MuonCM_err`, is calculated using the propa-  
2034        gation of errors of the mentioned variables.
- 2035     • The mean muon cluster multiplicity in the peak region, `MuonCM`, explicated above whose sta-  
2036        tistical error, `MuonCM_err`, is the sum of statistical error associated to the total mean clus-  
2037        ter multiplicity in the peak reagion, `PeakCM_err`, and of the mean noise/gamma cluster size,  
2038        `NoiseCM_err`.

2039        In addition to these 2 CSV files, the histograms are saved in ROOT file `Scan00XXXX_HVY_Offline.root`  
2040        as explained in section B.2.1.1.

2041

```

for (UInt tr = 0; tr < GIFInfra->GetNTrolleys(); tr++) {
    UInt T = GIFInfra->GetTrolleyID(tr);
    for (UInt sl = 0; sl < GIFInfra->GetNSlots(tr); sl++) {
        UInt S = GIFInfra->GetSlotID(tr,sl) - 1;
        for (UInt p = 0; p < GIFInfra->GetNPartitions(tr,sl); p++) {
            float noiseWindow =
                BMTDCWINDOW - TIMEREJECT - 2*PeakWidth.rpc[T][S][p];
            float peakWindow = 2*PeakWidth.rpc[T][S][p];
            float windowRatio = peakWindow/noiseWindow;

            float PeakCM = MuonCMult_H.rpc[T][S][p]->GetMean();
            float PeakCS = MuonCSize_H.rpc[T][S][p]->GetMean();
            float NoiseCM = NoiseCMult_H.rpc[T][S][p]->GetMean() *windowRatio;
            float NoiseCS = NoiseCSize_H.rpc[T][S][p]->GetMean();
            float MuonCM = (PeakCM<NoiseCM) ? 0. : PeakCM-NoiseCM;
            float MuonCS = (MuonCM==0 || PeakCM*PeakCS<NoiseCM*NoiseCS)
                ? 0.
                : (PeakCM*PeakCS-NoiseCM*NoiseCS) / MuonCM;
            float PeakCM_err = (MuonCMult_H.rpc[T][S][p]->GetEntries()==0.)
                ? 0.
                : 2*MuonCMult_H.rpc[T][S][p]->GetStdDev() /
                    sqrt(MuonCMult_H.rpc[T][S][p]->GetEntries());
            float PeakCS_err = (MuonCSize_H.rpc[T][S][p]->GetEntries()==0.)
                ? 0.
                : 2*MuonCSize_H.rpc[T][S][p]->GetStdDev() /
                    sqrt(MuonCSize_H.rpc[T][S][p]->GetEntries());
            float NoiseCM_err = (NoiseCMult_H.rpc[T][S][p]->GetEntries()==0.)
                ? 0.
                : windowRatio*2*NoiseCMult_H.rpc[T][S][p]->GetStdDev() /
                    sqrt(NoiseCMult_H.rpc[T][S][p]->GetEntries());
            float NoiseCS_err = (NoiseCSize_H.rpc[T][S][p]->GetEntries()==0.)
                ? 0.
                : 2*NoiseCSize_H.rpc[T][S][p]->GetStdDev() /
                    sqrt(NoiseCSize_H.rpc[T][S][p]->GetEntries());
            float MuonCM_err = (MuonCM==0) ? 0. : PeakCM_err+NoiseCM_err;
            float MuonCS_err = (MuonCS==0 || MuonCM==0) ? 0.
                : (PeakCS*PeakCM_err + PeakCM*PeakCS_err +
                    NoiseCS*NoiseCM_err + NoiseCM*NoiseCS_err +
                    MuonCS*MuonCM_err) / MuonCM;

            float DataRatio = MuonCM/PeakCM;
            float DataRatio_err = (MuonCM==0) ? 0.
                : DataRatio*(MuonCM_err/MuonCM + PeakCM_err/PeakCM);
            float eff = DataRatio*Efficiency0_H.rpc[T][S][p]->GetMean();
            float eff_err = DataRatio*2*Efficiency0_H.rpc[T][S][p]->GetStdDev() /
                sqrt(Efficiency0_H.rpc[T][S][p]->GetEntries()) +
                Efficiency0_H.rpc[T][S][p]->GetMean()*DataRatio_err;

            outputEffCSV << eff << '\t' << eff_err << '\t'
                << MuonCS << '\t' << MuonCS_err << '\t'
                << MuonCM << '\t' << MuonCM_err << '\t';
        }
    }
}

```

2042

2043

*Source Code B.20: Description of efficiency result calculation and writing into the CSV output Offline-L0-EffCl.csv. Are saved into the file for each detector, the efficiency, corrected taking into account the background in the peak window of the time profile, muon cluster size and muon cluster multiplicity, along with their errors, for each partition and as well as a detector average.*

## 2044 B.7 Current data Analysis

2045 Detectors under test at GIF++ are connected both to a CAEN HV power supply and to a CAEN  
2046 ADC that reads the currents inside of the RPC gaps bypassing the supply cable. During data tak-  
2047 ing, the webDCS records into a ROOT file called `Scan00XXXX_HVY_CAEN.root` histograms with the  
2048 monitored parameters of both CAEN devices. Are recorded for each RPC channels (in most cases,  
2049 a channel corresponds to an RPC gap):

- 2050 • the effective voltage,  $HV_{eff}$ , set by the webDCS using the PT correction on the CAEN power  
2051 supply,
- 2052 • the applied voltage,  $HV_{app}$ , monitored by the CAEN power supply, and the statistical error  
2053 related to the variations of this value through time to follow the variation of the environmental  
2054 parameters defined as the RMS of the histogram divided by the square root of the number of  
2055 recorded points,
- 2056 • the monitored current,  $I_{mon}$ , monitored by the CAEN power supply, and the statistical error  
2057 related to the variations of this value through time to follow the variation of the environmental  
2058 parameters defined as the RMS of the histogram divided by the square root of the number of  
2059 recorded points,
- 2060 • the corresponding current density,  $J_{mon}$ , defined as the monitored current per unit area,  
2061  $J_{mon} = I_{mon}/A$ , where  $A$  is the active area of the corresponding gap,
- 2062 • the ADC current,  $I_{ADC}$ , recorded through the CAEN ADC module that monitors the dark  
2063 current in the gap itself. First of all, the resolution of such a module is better than that of  
2064 CAEN power supplies and moreover, the current is not read-out through the HV supply line  
2065 but directly at the chamber level giving the real current inside of the detector. The statistical  
2066 error is defined as the RMS of the histogram distribution divided by the square root of the  
2067 number of recorded points.

2068 Once extracted through a loop over the element of GIF++ infrastructure via the C++ macro  
2069 `GetCurrent()`, these parameters, organised in 9 columns per detector HV supply line, are written in  
2070 the output CSV file `Offline-Current.csv`. The macro can be found in the file `Current.cc`.

## References

- 2072 [1] T. Massam et al. “Experimental observation of antideuteron production”. In: *Il Nuovo Cimento A* 63 (1965), pp. 10–14.
- 2073
- 2074 [2] UA1 Collaboration. “Experimental observation of isolated large transverse energy electrons with associated missing energy at  $s = 540 \text{ GeV}$ ”. In: *Physics Letters B* 122 (1983), pp. 103–116.
- 2075
- 2076
- 2077 [3] UA2 Collaboration. “Observation of single isolated electrons of high transverse momentum in events with missing transverse energy at the CERN pp collider”. In: *Physics Letters B* 122 (1983), pp. 476–485.
- 2078
- 2079
- 2080 [4] UA1 Collaboration. “Experimental observation of lepton pairs of invariant mass around  $95 \text{ GeV}/c^2$  at the CERN SPS collider”. In: *Physics Letters B* 126 (1983), pp. 398–410.
- 2081
- 2082 [5] UA2 Collaboration. “Evidence for  $Z_0 \rightarrow e^+e^-$  at the CERN pp collider”. In: *Physics Letters B* 129 (1983), pp. 130–140.
- 2083
- 2084 [6] ALEPH Collaboration. “Determination of the number of light neutrino species”. In: *Physics Letters B* 231 (1989), pp. 519–529.
- 2085
- 2086 [7] CERN, ed. (1985).
- 2087 [8] CERN, ed. (1986).
- 2088 [9] CERN, ed. (1994).
- 2089 [10] CERN, ed. (1998).
- 2090 [11] CERN, ed. (1999).
- 2091 [12] CERN. Geneva. LHC Experiments Committee. *Letter of Intent for A Large Ion Collider Experiment [ALICE]*, note = CERN-LHCC-93-016. Tech. rep. ALICE Collaboration, 1993.
- 2092
- 2093 [13] CERN. Geneva. LHC Experiments Committee. *ATLAS : technical proposal for a general-purpose pp experiment at the Large Hadron Collider at CERN*, note = CERN-LHCC-94-43. Tech. rep. ATLAS Collaboration, 1994.
- 2094
- 2095
- 2096 [14] CERN. Geneva. LHC Experiments Committee. *CMS : letter of intent by the CMS Collaboration for a general purpose detector at LHC*, note = CERN-LHCC-92-003. Tech. rep. CMS Collaboration, 1992.
- 2097
- 2098
- 2099 [15] CERN. Geneva. LHC Experiments Committee. *LHCb : letter of intent*. Tech. rep. CERN-LHCC-95-5. LHCb Collaboration, 1995.
- 2100
- 2101 [16] L. Evans and P. Bryant. “LHC Machine”. In: *JINST* 3 (2008). S08001.
- 2102
- 2103 [17] CMS Collaboration ATLAS Collaboration. “Combined Measurement of the Higgs Boson Mass in  $pp$  Collisions at  $\sqrt{s} = 7$  and  $8 \text{ TeV}$  with the ATLAS and CMS Experiments”. In: *Physical Review Letters* 114 (2015). 191803.
- 2104
- 2105 [18] LHCb Collaboration. “Observation of  $J/\psi p$  Resonances Consistent with Pentaquark States in  $\Lambda_b^0 \rightarrow J/\psi K^- p$  Decays”. In: *Physical Review Letters* 115 (2015). 072001.
- 2106

- [19] CERN. Geneva. *High-Luminosity Large Hadron Collider (HL-LHC) Technical Design Report V. 0.1*. Tech. rep. CERN-2017-007-M. 2017.
- [20] CERN. Geneva. LHC Experiments Committee. *The CMS muon project : Technical Design Report*. Tech. rep. CERN-LHCC-97-032. CMS Collaboration, 1997.
- [21] CERN. Geneva. LHC Experiments Committee. *Technical Proposal for the Phase-II Upgrade of the CMS Detector*. Tech. rep. CERN-LHCC-2015-010. CMS Collaboration, 2015.
- [22] CERN. Geneva. LHC Experiments Committee. *CMS, the Compact Muon Solenoid : technical proposal*. Tech. rep. CERN-LHCC-94-38. CMS Collaboration, 1994.
- [23] R. Santonico and R. Cardarelli. “Development of resistive plate counters”. In: *Nucl. Instr. Meth. Phys. Res.* 187 (1981), pp. 377–380.
- [24] Yu.N. Pestov and G.V. Fedotovich. *A picosecond time-of-flight spectrometer for the VEPP-2M based on local-discharge spark counter*. Tech. rep. SLAC-TRANS-0184. SLAC, 1978.
- [25] W.W. Ash, ed. *Spark Counter With A Localized Discharge*. Vol. SLAC-R-250. 1982, pp. 127–131.
- [26] I. Crotty et al. “The non-spark mode and high rate operation of resistive parallel plate chambers”. In: *NIMA* 337 (1993), pp. 370–381.
- [27] I. Crotty et al. “Further studies of avalanche mode operation of resistive parallel plate chambers”. In: *NIMA* 346 (1994), pp. 107–113.
- [28] R. Cardarelli et al. “Avalanche and streamer mode operation of resistive plate chambers”. In: *NIMA* 382 (1996), pp. 470–474.
- [29] E. Cerron Zeballos et al. “A new type of resistive plate chamber: The multigap RPC”. In: *NIMA* 374 (1996), pp. 132–135.
- [30] M.C.S. Williams. “The development of the multigap resistive plate chamber”. In: *Nucl. Phys. B* 61 (1998), pp. 250–257.
- [31] H. Czyrkowski et al. “New developments on resistive plate chambers for high rate operation”. In: *NIMA* 419 (1998), pp. 490–496.
- [32] P. Camarri et al. “Streamer suppression with SF<sub>6</sub> in RPCs operated in avalanche mode”. In: *NIMA* 414 (1998), pp. 317–324.
- [33] E. Cerron Zeballos et al. “Effect of adding SF<sub>6</sub> to the gas mixture in a multigap resistive plate chamber”. In: *NIMA* 419 (1998), pp. 475–478.
- [34] CERN. Geneva. LHC Experiments Committee. *ATLAS muon spectrometer: Technical design report*. Tech. rep. CERN-LHCC-97-22. ATLAS Collaboration, 1997.
- [35] CERN. Geneva. LHC Experiments Committee. *ALICE Time-Of-Flight system (TOF) : Technical Design Report*. Tech. rep. CERN-LHCC-2000-012. ALICE Collaboration, 2000.
- [36] The CALICE collaboration. “First results of the CALICE SDHCAL technological prototype”. In: *JINST* 11 (2016).
- [37] PoS, ed. *Density Imaging of Volcanoes with Atmospheric Muons using GRPCs*. International Europhysics Conference on High Energy Physics - HEP 2011. 2011.
- [38] C. Lippmann. “Detector Physics of Resistive Plate Chambers”. PhD thesis. Johann Wolfgang Goethe-Universität, 2003.
- [39] M. Abbrescia et al. “Properties of C<sub>2</sub>H<sub>2</sub>F<sub>4</sub>-based gas mixture for avalanche mode operation of resistive plate chambers”. In: *NIMA* 398 (1997), pp. 173–179.

## BIBLIOGRAPHY

---

- 2149 [40] G.Battistoni et al. “Sensitivity of streamer mode to single ionization electrons”. In: *NIMA*  
2150 235 (1985), pp. 91–97.
- 2151 [41] W. Riegler. “Induced signals in resistive plate chambers”. In: *NIMA* 491 (2002), pp. 258–271.
- 2152 [42] E. Cerron Zeballos et al. “A comparison of the wide gap and narrow gap resistive plate  
2153 chamber”. In: *NIMA* 373 (1996), pp. 35–42.
- 2154 [43] M.Abbrescia et al. “Cosmic ray tests of double-gap resistive plate chambers for the CMS  
2155 experiment”. In: *NIMA* 550 (2005), pp. 116–126.
- 2156 [44] ALICE Collaboration. “A study of the multigap RPC at the gamma irradiation facility at  
2157 CERN”. In: *NIMA* 490 (2002), pp. 58–70.
- 2158 [45] B. Bonner et al. “A multigap resistive plate chamber prototype for time-of-flight for the STAR  
2159 experiment at RHIC”. In: *NIMA* 478 (2002), pp. 176–179.
- 2160 [46] S. Yang et al. “Test of high time resolution MRPC with different readout modes for the  
2161 BESIII upgrade”. In: *NIMA* 763 (2014), pp. 190–196.
- 2162 [47] A. Akindinovg et al. “RPC with low-resistive phosphate glass electrodes as a candidate for  
2163 the CBM TOF”. In: *NIMA* 572 (2007), pp. 676–681.
- 2164 [48] JINST, ed. *Development of the MRPC for the TOF system of the MultiPurpose Detector.*  
2165 RPC2016: XII Workshop on Resistive Plate Chambers and Related Detectors. 2016.
- 2166 [49] M.C.S. Williams. “Particle identification using time of flight”. In: *Journal of Physics G* 39  
2167 (2012).
- 2168 [50] A. Alici et al. “Aging and rate effects of the Multigap RPC studied at the Gamma Irradiation  
2169 Facility at CERN”. In: *NIMA* 579 (2007), pp. 979–988.
- 2170 [51] M. Abbrescia et al. “The simulation of resistive plate chambers in avalanche mode: charge  
2171 spectra and efficiency”. In: *NIMA* 431 (1999), pp. 413–427.
- 2172 [52] M. Abbrescia et al. “Study of long-term performance of CMS RPC under irradiation at the  
2173 CERN GIF”. In: *NIMA* 533 (2004), pp. 102–106.
- 2174 [53] H.C. Kim et al. “Quantitative aging study with intense irradiation tests for the CMS forward  
2175 RPCs”. In: *NIMA* 602 (2009), pp. 771–774.
- 2176 [54] S. Agosteo et al. “A facility for the test of large-area muon chambers at high rates”. In: *NIMA*  
2177 452 (2000), pp. 94–104.
- 2178 [55] PoS, ed. *CERN GIF ++ : A new irradiation facility to test large-area particle detectors for*  
2179 *the high-luminosity LHC program*. Vol. TIPP2014. 2014, pp. 102–109.
- 2180 [56] A. Fagot. *GIF++ DAQ v4.0*. 2017. URL: [https://github.com/afagot/GIF\\_DAQ](https://github.com/afagot/GIF_DAQ).
- 2181 [57] CAEN. *Mod. V1190-VX1190 A/B, 128/64 Ch Multihit TDC*. 14th ed. 2016.
- 2182 [58] CAEN. *Mod. V1718 VME USB Bridge*. 9th ed. 2009.
- 2183 [59] W-Ie-Ne-R. *VME 6021-23 VXI*. 5th ed. 2016.
- 2184 [60] Wikipedia. *INI file*. 2017. URL: [https://en.wikipedia.org/wiki/INI\\_file](https://en.wikipedia.org/wiki/INI_file).
- 2185 [61] S. Carrillo A. Fagot. *GIF++ Offline Analysis v6*. 2017. URL: <https://github.com/>  
2186 [afagot/GIF\\_OfflineAnalysis](https://github.com/afagot/GIF_OfflineAnalysis).